

**STRUCTURAL, COMPOSITIONAL AND  
MECHANICAL CHARACTERIZATION OF  
PLASMA NITRIDED CoCrMo ALLOY**

**A Thesis Submitted to  
the Graduate School of Engineering and Sciences of  
İzmir Institute of Technology  
in Partial Fulfillment of the Requirements for the Degree of**

**MASTER OF SCIENCE**

**in Physics**

**by  
Serdal OKUR**

**December 2009  
İZMİR**

We approve the thesis of **Serdal OKUR**

---

**Prof. Dr. Orhan ÖZTÜRK**  
Supervisor

---

**Dr. Luc PICHON**  
Committee Member

---

**Asst. Prof. Dr. Sami SÖZÜER**  
Committee Member

16 December 2009

---

**Prof. Dr. Durmuş Ali DEMİR**  
Head of the Department of Physics

---

**Prof. Dr. Talat YALÇIN**  
Dean of the Graduate School of  
Engineering and Sciences

## ACKNOWLEDGMENTS

It has been a privilege to have been educated by my advisor, Prof. Dr. Orhan Öztürk. I would like to extend my outmost appreciation to him for his invaluable help, guidance, encouragement and his endless patience as well as his self-sacrifice without which this thesis would not have been possible. I appreciate the efforts that he has made in my personal development as a researcher and numerous technical discussions required by this study.

I would like to thank Prof. Jean Paul Riviere, Dr. Luc Pichon and Prof. Dr. Michel Drouet from Laboratoire de Physique des Matériaux, Université de Poitiers for carrying out the RF plasma nitriding of CoCrMo samples, providing profilometry measurements, Vicker's mikrohardness and wear test measurements as well as their contribution and help.

This study presented here satisfies one of the aims of a joint research project directed by Prof. Dr. Orhan Öztürk and Prof. Dr. Jean Paul Riviere partially supported by Tubitak through the grant 107M218 (Turkey) and Programme of Integrated Actions (PIA) Bosphorus (France).

Also, I would also like to acknowledge my institution, İzmir Institute of Technology, for providing me research facilities during my graduate study.

I am very thankful to TIPSAN (İzmir) for providing the medical grade CoCrMo alloy materials.

My other big "Thank you!" is for the staff of Material Research Center of İzmir Institute of Technology for their contribution.

I would like to thank Assoc. Prof. Dr. Salih Okur for providing the atomic force microscope and some of the sample preparation equipments.

Special thanks go to Prof. Dr. Mustafa Güden for providing polishing system and Research Assistant Uğur Türkan for helping preparation of the electrochemical etching system.

Also, I would like to thank Assoc. Prof. Dr. Lütfi Özyüzer and Research Assistants Hasan Köseoğlu and Fulya Türkoğlu for performing Ar<sup>+</sup> ion beam etching of the cross-sectional samples.

I would like to thank Fahri Hasyamanlar and Gökhan Özdemir of NEKA Kalıp (Manisa, Turkey) for cross-sectional sample preparations by providing wire electrical discharge machining.

I am also grateful to my friends; Emre Gözütok, Öcal Tuna, Hüseyin İlgü, Ali Kemal Havare and Arda Müftüoğlu for their encouragement, and my colleagues at Physics Department for their support and sympathy.

I am very grateful to thank Assoc. Prof. Dr. Salih Okur, his wife Nurcan Okur and his lovely children Furkan Okur, Esra Okur and İhsan Emre Okur for their invaluable encouragement and sincere during my studies.

Last but not least, thanks to my family and my fiancée Nigar Kale, for their support, understanding and love. How little is my gratitude in comparison to their contributions.

## ABSTRACT

### STRUCTURAL, COMPOSITIONAL AND MECHANICAL CHARACTERIZATION OF PLASMA NITRIDED CoCrMo ALLOY

Plasma nitriding techniques can be used to create wear and corrosion protective layers on the surface of CoCrMo alloys by modifying the near surface layers of these materials. In the present study, a medical grade CoCrMo alloy was nitrided in a low-pressure ( $\sim 60$  mTorr) R. F. plasma at  $400$  °C for 1, 2, 4, 6, and 20 hours under a gas mixture of 60%  $N_2$  – 40%  $H_2$ . The structural as well as compositional characterization of the plasma nitrided layers were investigated by X-ray diffraction (XRD), scanning electron microscopy (SEM), atomic force microscopy (AFM), and glow discharge optical emission spectroscopy (GDOES). The hardness and wear behaviour of the nitrided layers were performed by a microhardness tester and a pin-on-disk wear apparatus. The experimental analyses indicate that the expanded austenite phase,  $\gamma_N$ , with high N contents ( $\sim 30$  at.%) is formed by the plasma nitriding process at  $400$  °C. However, at longer nitriding times (6 and 20 h) there is decomposition into CrN in the  $\gamma_N$  matrix and a preferential (200) orientation of  $\gamma_N$  grains parallel to the surface develops. Based on the microscopy analyses of the electrochemically and Ar ion beam etched nitrided sample cross-sections and on the GDOES data, the  $\gamma_N$  layer thicknesses are found to be ranging from  $\sim 2$  to 10 microns. Based on the thickness data, an average N diffusion coefficient for the CoCrMo samples plasma nitrided at  $400$  °C is estimated to be near  $2 \times 10^{-11}$   $cm^2/s$ . While significant improvements in hardness and wear volume reductions are observed for all the plasma nitrided alloys compared to the untreated alloy, the CoCrMo alloys with the  $\gamma_N$  structure only had the best combined wear-corrosion protection.

## ÖZET

### PLAZMA NİTRÜLENMİŞ CoCrMo ALAŞIMININ YAPISAL, KOMPOZİSYONEL VE MEKANİK KARAKTERİZASYONU

Plazma nitrüleme teknikleri, CoCrMo alaşımlarının yakın yüzey tabakalarını modifiye ederek bu malzemelerin yüzeylerinde aşınma ve korozyona dayanıklı tabakalar oluşturmada kullanılmaktadır. Bu çalışmada, medikal sınıfı CoCrMo alaşımı, düşük basınç altında ( $\sim 60$  mTorr),  $60\% \text{N}_2 - 40\% \text{H}_2$  gaz karışımında ve  $400^\circ\text{C}$  de 1, 2, 4, 6 ve 20 saat sürelerince RF plazma nitrülenmiştir. Plazma nitrülenmiş tabakaların yapısal ve kompozisyonel karakterizasyonu X-ışınları kırınımı (XRD), taramalı electron mikroskobu (SEM), atomik kuvvet mikroskobu (AFM) ve glow discharge optik emisyon spektroskopisi (GDOES) teknikleri kullanılarak incelenmiştir. Nitrülenmiş tabakaların sertlik ve aşınma davranışları mikrosertlik ve pin-on-disc testleri kullanılarak incelenmiştir. Deneysel analiz sonuçları,  $400^\circ\text{C}$ ' deki plazma nitrüleme işlemi sonucunda, yüksek azot içeriğine sahip ( $\sim 30$  at.%) genişlemiş östenit fazının ( $\gamma_{\text{N}}$ ) oluştuğunu göstermektedir. Bununla birlikte, uzun nitrüleme sürelerinde (6 ve 20 saat)  $\gamma_{\text{N}}$  fazında CrN dekompozisyonu ve yüzeye paralel olan  $\gamma_{\text{N}}$  taneciklerde (200) tercihli yönelmeler oluşmaktadır. Elektrokimyasal ve  $\text{Ar}^+$  ışınları yöntemiyle dağlanmış nitrülenmiş malzemelerinin kesit-yüzey mikroskopi analizlerine ve GDOES verilerine göre, nitrülenmiş tabakaların kalınlıkları yaklaşık olarak 2 ile 10 mikrometre arasında değişmektedir. Kalınlık analizlerine göre, CoCrMo malzemelerinin  $400^\circ\text{C}$ ' de plazma nitrülenmesi sonucu, ortalama azot difüzyon katsayısı yaklaşık olarak  $1.5 \times 10^{-11} \text{ cm}^2/\text{s}$  bulunmuştur. Tüm plazma nitrülenmiş CoCrMo alaşımlarında önemli sertlik ve aşınma iyileşmeleri gözlenmesine rağmen, en iyi aşınma-korozyon dayanıklılığı yalnızca  $\gamma_{\text{N}}$  yapısına sahip CoCrMo alaşımlarında gözlenmiştir.

*To my Family*

# TABLE OF CONTENTS

LIST OF FIGURES .....	xii
LIST OF TABLES .....	xivv
CHAPTER 1. INTRODUCTION .....	1
1.1. Metallic Biomaterials and Cobalt-Chrome-Molybdenum (CoCrMo) Alloy .....	1
1.2. Plasma Nitriding .....	5
1.3. Expanded Austenite Phase ( $\gamma_N$ ).....	6
1.4. Purpose of This Work .....	10
CHAPTER 2. EXPERIMENTAL METHODS .....	11
2.1. Sample and Sample Preparation .....	11
2.2. Plasma Nitriding .....	13
2.2.1. Plasma Characteristics .....	16
2.3. Cross-Sectional Sample Preparation.....	19
2.3.1. Electrochemical Etching .....	20
2.3.2. Ar <sup>+</sup> Beam Etching .....	20
2.4. Microstructural Characterization .....	21
2.4.1. XRD Analysis .....	21
2.4.1.1. Bragg-Brentano Method.....	23
2.4.1.2. Grazing Incidence X-Ray Method .....	24
2.4.2. Optical Spectroscopy .....	26
2.4.3. SEM Analysis.....	26
2.4.4. Atomic Force Microscopy.....	26
2.4.4.1. Roughness Measurements.....	27
2.5. PeakFit Program.....	28
2.6. Compositional Characterization.....	28
2.7. Mechanical Characterization .....	28
2.7.1. Microhardness Measurements.....	29



2.7.2. Wear Test (Pin on disc and Oscillating TRIBOtester).....	30
CHAPTER 3. DATA ANALYSIS AND MODELING .....	31
3.1. XRD Data Curve Fitting .....	31
3.2. Epsilon Phase Analysis .....	32
3.3. Lattice Parameter and Nitrogen Concentration Analyses .....	33
3.4. Layer Thickness Analysis .....	35
CHAPTER 4. PLASMA NITRIDED CRYSTAL STRUCTURES .....	38
4.1. XRD Results .....	38
4.2. GIXRD Results .....	47
CHAPTER 5. TOPOGRAPHICAL CHARACTERIZATION .....	50
5.1. CoCrMo Substrate Surfaces.....	50
5.2. Plasma Nitrided Surfaces .....	52
CHAPTER 6. CROSS-SECTIONAL MICROSCOPY CHARACTERIZATION.....	63
6.1. Cross-sections of Polishing Plasma Nitrided Samples .....	63
6.2. Cross-sections of Electrochemically Etched Plasma Nitrided Samples.....	65
6.3. Cross-sections of Ar Beam Etched Plasma Nitrided Samples.....	68
CHAPTER 7. COMPOSITION-DEPTH ANALYSES OF PLASMA NITRIDED LAYERS .....	74
7.1. Compositional Characterization.....	74
7.2. GDOES Nitrogen Concentration Depth Profiles .....	78
7.3. Nitrogen Diffusion Constant Analysis.....	84
CHAPTER 8. MECHANICAL CHARACTERIZATION OF PLASMA NITRIDED LAYERS .....	88
8.1. Microhardness Results .....	88
8.2. Wear Results .....	92

CHAPTER 9. CONCLUSIONS .....	98
9.1. Summary and Discussion.....	98
9.2. Conclusions.....	101
9.3. Future Work.....	102
REFERENCES .....	103

# LIST OF FIGURES

<b><u>Figure</u></b>	<b><u>Page</u></b>
Figure 1. 1. Various components of total hip joint prosthesis. The picture on the right represents an actual hip implant fabricated from CoCrMo alloy .....	1
Figure 1. 2. Different femoral head-cup combinations according to cumulative wear after 10 years in vivo environment .....	3
Figure 2. 1. Schematic diagram of fcc CoCrMo lattice.....	11
Figure 2. 2. The schematic diagram of RF Plasma Reactor .....	13
Figure 2. 3. RF Plasma Reactor .....	14
Figure 2. 4. Nitriding temperature versus nitriding treatment time for the 1 h nitrided specimen. ....	19
Figure 2. 5. The schematic diagram of electrochemical etching system .....	20
Figure 2. 6. The graph shows Thin Film Philips X'Pert Pro MRD System which is used for XRD experiments in this study .....	22
Figure 2. 7. Schematic diagram of an x-ray diffractometer illustrating its main components and the angular shift.....	24
Figure 2. 8. Schematic diagram of GIXRD measurements .....	25
Figure 2. 9. A schematic picture of AFM cantilever .....	27
Figure 2. 10. Schematic diagram of wear test.....	30
Figure 3. 1. Curve-fit of XRD data of 1 h plasma nitrided CoCrMo sample (D15).....	31
Figure 3. 2. Curve-fit of the CoCrMo substrate XRD data (D10).....	32
Figure 3. 3. Nelson-Riley plot of the CoCrMo substrate sample (D10).....	33
Figure 3. 4. The model for calculation of the linear mass absorption coefficient. ... ..	35
Figure 4. 1. X-ray diffraction spectrum of CoCrMo substrate (D15).....	38
Figure 4. 2. XRD spectrums of substrate and plasma nitrided CoCrMo samples. ....	39
Figure 4. 3. $\gamma_N$ -(Co,Cr,Mo) crystal structure in plasma nitrided CoCrMo alloy. ....	40
Figure 4. 4. Distribution of (111) and (200) lattice constants of plasma nitrided and substrate CoCrMo samples .....	43
Figure 4. 5. GIXRD spectrums ( $\omega = 1^\circ$ ) of 1, 2, 4, 6 and 20 h plasma nitrided samples.....	48

Figure 4. 6. GIXRD spectrum of 20 h plasma nitrided CoCrMo at various grazing angles; $\omega = 0.5^\circ, 1^\circ, 2^\circ, 2.5^\circ, 3^\circ, 4^\circ, 5^\circ, 10^\circ$ . .....	49
Figure 5. 1. SEM images of CoCrMo substrate surface (D10) after Ar beam etching (above) and electrochemical etching (below). .....	51
Figure 5. 2. The optical interferometry images of the plasma nitrided as well as the substrate CoCrMo surfaces .....	53
Figure 5. 3. 2-D AFM images of the plasma nitrided surfaces. AFM image of the substrate (0h) is also included. ....	55
Figure 5. 4. 3-D AFM images of the plasma nitrided surfaces. AFM image of the substrate (0h) is also included. ....	59
Figure 5. 5. SEM pictures of 2 h (above) and 20 hours (below) plasma nitrided CoCrMo surfaces. ....	61
Figure 6. 1. SEM (top) and optical microscopy (bottom) images of the cross-sections of 6 and 20 h plasma nitrided samples, respectively, after polishing. ....	64
Figure 6. 2. Cross-sectional SEM images of 2, 6 and 20 h plasma nitrided samples after electrochemical etching. ....	66
Figure 6. 3. Cross-sectional SEM images of the 1, 2, 4, 6 and 20 h plasma nitrided CoCrMo samples after Ar beam etching. The bottom right figure shows a cross-sectional optical microscopy image of the 20 h plasma nitrided sample. ....	69
Figure 6. 4. 2-D and 3-D cross-sectional AFM graphs of 20 h plasma nitrided sample. ....	72
Figure 7. 1. The GDOES results of CoCrMo substrate sample (D15). Concentrations of Mo, Si, Mn and N elements are multiplied by 10 for clarity. ....	74
Figure 7. 2: The GDOES results of 6 h plasma nitrided CoCrMo sample. The concentration of Mo, Si and Mn are multiplied by 10 for clarity. ....	76
Figure 7. 3. The EDX results of the 2 h nitrided sample from surface (above) and cross-sectional EDX result of 4 h nitrided layer (below). ....	77
Figure 7. 4. GDOES nitrogen concentration-depth results of plasma nitrided CoCrMo samples. ....	79
Figure 7. 5. Calculation of the nitrogen diffusion coefficients from the experimental nitrided layer thickness of the cross-sectional Ar <sup>+</sup> beam and electrochemical etching as well as the GDOES data. ....	85

Figure 8. 1. Microhardness data for the plasma nitrided and CoCrMo substrate samples. The microhardness is in $\text{kg/mm}^2$ ( $2000 \text{ kg/mm}^2 = 19.6 \text{ GPa} = \sim 20 \text{ GPa}$ ) and load in N ( $\text{kg.m/s}^2$ ).....	91
Figure 8. 2. Average microhardness of the plasma nitrided samples and the microhardness of substrate sample as well as the fit of the substrate. The microhardness is in $\text{kg/mm}^2$ ( $2000 \text{ kg/mm}^2 = 19.6 \text{ GPa} = \sim 20 \text{ GPa}$ ) and load in N ( $\text{kg.m/s}^2$ ). .....	91
Figure 8. 3. Optical profilometer wear track results of the 2 h nitrided specimen for 1 N load and 200 m sliding wear distance used in wear results calculations. ....	95
Figure 8. 4. Wear widths and volumes for the plasma nitrided specimens for all the wear conditions (loads = 1, 4 N; sliding wear distance = 200, 600 m). For the substrate sample (0 h), all the estimated wear volume values are divided by 10 for comparison purposes. ....	96

## LIST OF TABLES

<b><u>Table</u></b>	<b><u>Page</u></b>
Table 1.1. Metallic biomaterials and some of their properties. Bone is also presented for comparison.....	2
Table 2. 1. Chemical composition of the CoCrMo alloy samples a) 30 mm (D30), b) 15 mm (D15), c) 10 mm (D10).....	12
Table 2. 2. RF plasma nitriding conditions.....	18
Table 3. 1. The values used in estimation of linear mass absorption coefficients for both substrate and plasma nitrided samples. GDOES data of substrate (D15) and 2 h nitrided sample are presented. ....	36
Table 3. 2. The linear mass absorption coefficients ( $\text{cm}^{-1}$ ).....	37
Table 4. 1. $2\theta$ peak centers of $\gamma(111)$ , $\gamma(200)$ , $\gamma_N(111)$ and $\gamma_N(200)$ of plasma nitrided samples as well as substrate sample obtained after curve-fit analyses. ....	41
Table 4. 2. Lattice parameters, $a$ , in Å for the CoCrMo alloy $\gamma$ -(CoCrMo) phase and the fcc $\gamma_N$ -(CoCrMo) phase. $\langle a \rangle$ represents average lattice parameters, while $\Delta a/a$ refers to the relative difference in lattice parameters. Also, nitrogen concentrations, $C_N$ in at.% for $\gamma_N$ -(CoCrMo) and $\langle C_N \rangle$ represents average nitrogen concentration along the plasma nitrided layers.....	44
Table 4. 3. The estimated $\gamma_N$ layer thicknesses based on (111) and (200) oriented grains and their average values. ....	46
Table 5.1. Average and RMS roughness values of as-polished and plasma nitrided CoCrMo surfaces based on the AFM measurements.....	54
Table 6. 1. Plasma nitrided layer thicknesses calculated after cross-sectional microscopy experiments. ....	73
Table 7. 1. The GDOES elemental composition result of CoCrMo substrate.....	75
Table 7. 2. The EDX average elemental composition values of plasma nitrided CoCrMo samples as well as substrate sample (D15) (obtained on the surfaces). ....	78

Table 7. 3. Thickness of the plasma nitrided layers obtained from the GDOES results. ....	80
Table 7. 4. Nitrogen diffusion coefficients obtained from Figure 7.5. ....	86
Table 8. 1. Average diagonal lengths ( $\mu\text{m}$ ) and probe depths ( $\mu\text{m}$ ) of the substrate according to the applied microindenter loads (grams). Average values were obtained from several indents for each load. ....	88
Table 8. 2. Vicker's microhardness ( $\text{HV}$ in $\text{kg}/\text{mm}^2$ ) data for the nitrided specimens. The loads (first row) are in grams. The average Vicker's microhardness values in the table are estimated from the microhardness values of the 1, 2, 4, 6 and 20 h nitrided samples (without taking into account the substrate hardness). ....	90
Table 8. 3. Wear volume, wear width and wear depth data of the wear tracks of 2, 6 and 20 h nitrided as well as substrate (0 h) samples for different wear conditions. The wear volume is estimated by multiplying cross-sectional wear areas and wear widths of the wear tracks. ....	93
Table 8. 4. Optical images of wear tracks (1 N-600 m and 4 N-200 m) of 0, 2, 6 and 20 h plasma nitrided samples. ....	94

# CHAPTER 1

## INTRODUCTION

### 1.1. Metallic Biomaterials and Cobalt-Chrome-Molybdenum (CoCrMo) Alloy

Although CoCrMo alloy is also used in aero- and land-based gas turbines technologies, its widely used applications are in biomedical practices such as hip and knee joint replacements due to its excellent mechanical properties. Figure 1.1 shows the various components of a total hip replacement. The femoral stem fits down into femur. The ball on top of the femoral stem is called the femoral head and fits into the hip joint in the pelvis. An ultra high molecular weight polyethylene (UHMWPE) liner fits inside the acetabular cup and provides the articulating surface for the femoral head (Duisabeau 2004, Katti 2004, Long 1998). The two elements of the hip implant have been made using a variety of materials such as metals, ceramics, polymers and composites. The biocompatibility of CoCrMo alloy is closely related to its excellent corrosion resistance, mainly due to the high chromium content ( $\sim 30$  at.%), higher than 316L austenitic stainless steel ( $\sim 18-20$  at.%), which has also clinical uses. Thin passive oxide film predominantly forms  $\text{Cr}_2\text{O}_3$  while there are some minor contributions from cobalt oxides without molybdenum oxides on the alloy (Simith 1991).

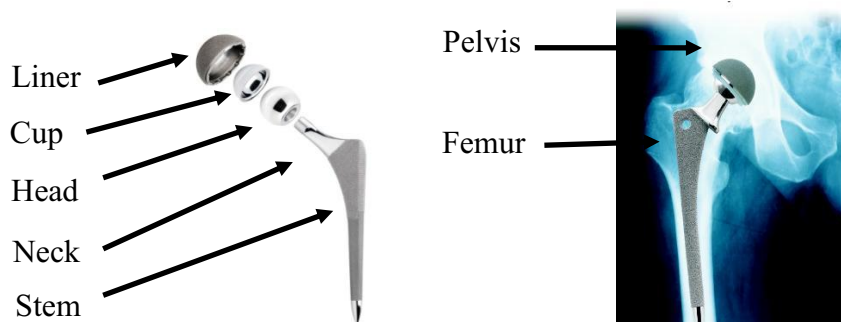


Figure 1. 1. Various components of total hip joint prosthesis. The picture on the right represents an actual hip implant fabricated from CoCrMo alloy (Source: Total Hip Replacement: Implant Choices 2009).



Biomaterial is defined as “any substance (other than a drug) or combination of substances, synthetic or natural in origin, which can be used for any period of time, as a whole or as a part of a system which treats, augments or replaces any tissue, organ, or function of the body” (Eden 1984). Biomaterials must have special properties to be used in particular biomedical applications. Biocompatibility, non-carcinogenicity, corrosion resistance, wear resistance and low toxicity are such requirements that biomedical materials must have (Ratner 1996, Lakes 1992). Metallic biomaterials have widespread use in replacing the structural components of the human body because of their excellent mechanical properties such as tensile and fatigue strengths and toughness. Some of their uses in medical devices are artificial joints, dental implants, bone plates, wires, and stents. Table 1.1 list some metallic biomaterials and some of their mechanical properties. In Table 1.1, also, the mechanical properties of bone is presented for comparison.

Table 1. 1. Metallic biomaterials and some of their properties. Bone is also presented for comparison (Source: Alvarado 2003).

	Microstructure	Density (g/cm <sup>3</sup> )	Young's Modulus, E (GPa)	Yield Strength, $\sigma_y$ (MPa)	Tensile Strength, $\sigma_{UTS}$ (MPa)	Fatigue Limit, $\sigma_{end}$ (MPa)
SS (316L)	fcc	~ 8.00	190	221-1213	586-1351	241-820
CoCrMo	fcc, hcp	~ 8.50	210-253	448-1606	655-1896	207-950
Ti	hcp	~ 4.51	110	485	760	300
Ti6Al4V	hcp, bcc	~ 4.40	116	896-1034	965-1103	620
Bone	OHAp + coll.	~ 2.00	15-30	30-70	70-150	-

Most artificial joints form of a metallic component articulating against a polymer. Metallic elements such as Co, Cr or Mo are released as ions and wear debris due to corrosion and wear created from the polymeric material in such metal-on-polymer systems are fully disadvantageous for human body. In metal-on-polyethylene types of artificial joint replacements wear particles migrate to bone and cause osteolysis surrounding the tissue and loosening the fixation site. Recently, metal-on-metal (MoM)

joints have been taking great attention due to the polyethylene wear debris problems accompanying with the metal-on-polyethylene type of artificial joint replacements. Less wear and tissue inflammation for metal-on-metal articulations have significantly been observed in both vitro and vivo studies (Chiba 2007, Yan 2006) compared to the metal-on-polymer articulations. There are still concerns about released metal ions and wear debris in spite of that longer service duration and less inflammatory osteolysis are noticed for MoM replacements. Chemical or electrochemical reactions and wear induced corrosion processes cause the releases of metallic ions from orthopaedic implants into the body environments. Figure 1.2 shows different femoral head-cup combinations with respect to cumulative wear after 10 years in vivo environment. As seen from Figure 1.2, CoCrMo head-cup combination shows superior property compared to UHMWPE-ceramic and UHMWPE-CoCrMo options.

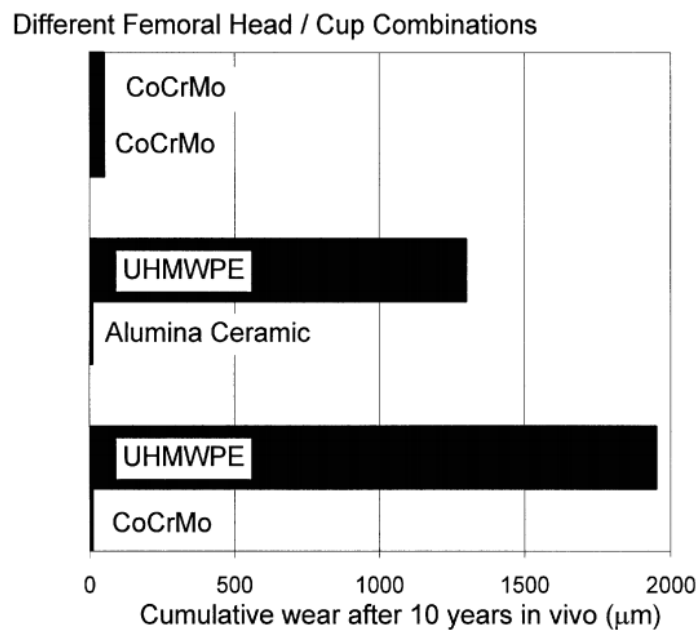


Figure 1. 2. Different femoral head-cup combinations according to cumulative wear after 10 years in vivo environment (Source: Long 1998).

The history of metallic biomaterials begins with steel which was introduced in the 19<sup>th</sup> century as screws to fix bone fractures in surgical applications. Because of the inclination of the steel to corrode in the human body, promising materials have been developed with sufficient corrosion resistance over time. Consequently, stainless steel, cobalt-chromium-molybdenum and titanium alloys becoming the main metallic

biomedical materials took their places in clinical practice. However, they have several service problems in use of orthopaedic applications:

- i. Toxicity from wear debris
- ii. Lack of biocompatibility with surrounding tissue
- iii. High rigidity compared to bone causing bone loss due to stress
- iv. Fracture due to fretting corrosion fatigue

The failure of the metallic implant devices such as hip-joint due to the corrosion is on occasion because they are already corrosion resistive materials. Corrosion resistivity in these materials relies on thin passive oxide films, such as chromium oxide in stainless steels and cobalt-chromium-molybdenum and titanium dioxide in titanium alloys spontaneously occur on the alloy surfaces protecting the underlying matrix material. Nevertheless, they may fail due to corrosion fatigue and fretting corrosion fatigue (Teoh 2000, Waterhouse 1981, Sumita 2000)). These kinds of corrosion processes begin and gain acceleration if the partial pressure of oxygen decreases inside the body. That is why; the regeneration time of the passive oxide film slows down once it is broken in the condition of lower partial pressure of oxygen. In addition to this it is unpreventable situation that some of metal ions and debris, which are generated by the fatigue and wear processes in joint prosthesis, are released from implanted metallic materials during long-term use (Bianco 1996, Mu 2000). These ions and debris adversely react with the host tissue. However, this can be assumed to be natural defence of the body. The wear debris typically triggers an inflammatory and immunological responses leading to initiation of cancer and allergic responses (Zairyu-Kagaku 1982).

Because of toxicity of nickel and its susceptibility to stress, stainless steels have limited use in clinical practices. They are generally used in temporary devices for load bearing applications (Banoczy 1979). In spite of that stainless steels are inferior in terms of quality compared to cobalt-chromium-molybdenum and titanium alloys, the reason why stainless steels are still used as metallic biomaterials in large quantities is due to their low cost which is about ten times lower than others (Pourbaix 1974). Though, titanium alloys are superior in specific strength, corrosion resistance, and biocompatibility compared to stainless steel and cobalt-chromium-molybdenum alloys, the restrictions of its prevalent use as biomaterial are that of its inferior tribological properties and high costs. Comparing these three alloys as metallic biomaterial in terms

of biomedical properties and availability, cobalt-chrome-molybdenum (CoCrMo) alloys are advantageous to stainless steel and titanium alloys.

As mentioned before, essential parameters in determining the suitability of a metallic biomaterial in surgical implants are corrosion resistance and wear behavior. Although CoCrMo has very good corrosion resistance, corrosion fatigue and wear induced corrosion processes can still cause failures. In order to improve surface properties of the metallic biomaterials, some surface modification techniques have been developed up to now. By changing the composition and structure, some surface modification techniques not only enhance surface properties, but also mechanical properties of the metallic biomaterials.

## **1.2. Plasma Nitriding**

Plasma technologies have been improved very fast and established various kinds changing in particular applications over the time. Plasma nitriding is such a technique in which ions and electrons are efficiently used to enhance the surface properties of the biomaterials. Plasma nitriding (Conventional DC) is carried out in the region of abnormal glow discharge where the work piece to be nitrided is completely covered with energetic ions (Karakan 2003) and due to the interaction between the ionised nitrogen in the plasma and the surface of the work piece, nitrogen starts to diffuse into the specimen. The absorbed nitrogen forms a nitrogen-rich environment, which is named as nitrided layer or zone. If the nitrogen content in the surface is high enough, nitrides will be precipitated.

Also, there are other surface modification techniques in which energetic ions are used to enhance the surface properties of metallic biomaterials. Ion beam techniques such as ion implantation, plasma immersion ion implantation and plasma technologies are some of efficient surface modification methods to form wear resistant layers on the surface of biomaterials. These surface modification techniques have been successfully applied to metallic biomaterials (stainless steels, titanium and cobalt-chrome alloys) to improve their wear resistance. Not only nitrogen is used in ion implantation and plasma technologies but also carbon, boron, silicon, and inert ions (Ar, He). Among the gaseous species nitrogen has been studied most extensively due to its abundance in nature and its observed ability to improve surface properties.

Plasma nitriding is widely used as a surface engineering technique to improve the surface hardness and wear resistance of various engineering materials. In recent years, nitriding of metallic biomaterials using the low temperature nitriding technology has been extensively investigated and rapidly gained industrial applications (Bell 2002). There are several advantages in plasma nitriding comparing to the ion implantation techniques. One of the main advantage of this process is low energies of ions. In ion implantation, the ions are highly energetic requiring high vacuum conditions and costs. The energies change between 1 keV and 100 keV while the ion energies are in the range of eV (10-100 eV) in plasma nitriding obtaining thicker protective nitrided layers according to applied time. One of the advantages accompanying the plasma nitriding is that it is a sputterless process. In ion implantation, high energetic ions sputter the surface removing the native oxide layer which gives the corrosivity to metallic biomaterials. Also, plasma nitriding is more suitable for complex shaped implants such as femoral head and femoral prostheses due to the three dimensional sight. Such implantation techniques limit their applications because of their line of sight application.

Plasmas are created by supplying energy to a neutral gas (Grill 1994, Rosnagel 1990, Rutscher 1983) by various ways. Any neutral gas always contains a few electrons and ions, for example, as the result of the interaction of cosmic rays or radioactive radiation with the gas. By the effects of electron-impact ionization or photoionization, electrons and ions are produced in the neutral gas when electrons or photons with sufficient energy collide with the neutral atoms and molecules in the feed gas. One of possible energy sources is thermal energy, while adiabatic compression of the gas is also capable of plasma generation. Another way to supply energy to a gas is to apply an electric field to a neutral gas. The dimensions of a plasma source are determined largely by particular applications for which the plasma is intended.

### **1.3. Expanded Austenite Phase ( $\gamma_N$ )**

Now it is well-established that nitrogen incorporation into the surface of austenitic stainless steels (304, 310, 316L, etc.) by a wide variety of ion beam methods at moderate surface treatment temperatures ( $\sim 400$  °C) lead to a high-N content face-centered-cubic (fcc) phase,  $\gamma_N$ , in the treated layers (Zhang 1985, Williamson 1994, Dearnley 1989, Ichii 1986). High strength (surface hardness values as high as 20 GPa),

good corrosion resistance and significantly improved wear resistance under high loads are a few of the technologically important properties reported in the literature for the  $\gamma_N$  phase, also known as the expanded austenite phase.

Recent studies (Chen 2008, Öztürk 2006) show that the expanded austenite phase ( $\gamma_N$ ) can also be formed on the surface of CoCrMo alloys by a variety of surface modification techniques with significant improvements in wear and corrosion behavior of these alloys. The investigated methods include plasma surface alloying (Chen 2007), conventional beamline nitrogen ion implantation (Öztürk 2006), high intensity plasma ion nitriding (Wei 2004) or plasma immersion ion implantation (PIII) (Lutz 2008). Similar to nitriding of austenitic stainless steel (Mändl 2007), insertion of nitrogen into the original lattice on interstitial site, a lattice expansion and an anomalous diffusion is observed for CoCr (Lutz 2008) alloys.

The understanding of N diffusion mechanism is very important. There have been reported some nitrogen diffusion mechanisms (Williamson 1998, Perdaza 2007, Abrasonis 2005, He 2003) in order to explain nitrogen diffusion enhancement of austenitic stainless steels (ASSs) under various types of nitriding techniques and of various treatment conditions. An earlier study of D. L. Williamson et. al (Williamson 1992) suggested a qualitative model that the substrate element Cr in the fcc ASS plays a significant role when coupled with the high flux N beam. Selective bonding between N and Cr has major effect on the mobility of nitrogen (Singer 1984). This can be explained by the trapping effect of Cr on the migration of nitrogen in these materials (Trapping-Detrapping model (TD)). The TD model is based on the fact that the Cr atoms act as trap sites for the nitrogen and, a faster diffusion of nitrogen is observed when all traps are saturated. Other models were also proposed to explain the shape of nitrogen depth profile and the enhanced diffusivity in ASS. The concentration-dependent diffusion model [ $D(C_N)$ ] was proposed as an alternative to the TD model. The  $D(C_N)$  model is motivated by the expansion of the austenitic lattice by dissolution of nitrogen, which is likely to facilitate the transfer of a nitrogen atom from octahedral to the tetrahedral interstitial sites (Christiansen 2008).

It has been established that plasma nitriding techniques are effective in improving both surface hardness and corrosion resistance of austenitic stainless steels (ASS), only when they are performed at temperatures lower than about 450 C° (Li 2004, Fewell 2000). In fact, by using such low temperatures the modified surface layer consists essentially of a metastable phase  $\gamma_N$  (Kumar 2000, Singh 2006) or S-phase,

which has proved to have high hardness and very good corrosion resistance. So, the main critical parameter in development of a precipitate-free S-phase is recognized to be the process temperature. In stainless steels, high temperatures lead to the formation of chromium nitrides above 450 °C, which bind chromium from the solid solution, thereby lowering the resistance to corrosion (Samandi 1993).

Some study in the literature were done in order to analyze the temperature effect in austenitic stainless steels. As a result of these studies, in order to avoid the transformation of the chromium of lattice into chromium nitride at the surface or in the bulk, the process temperature is limited to 400-450 °C (Zhang 1985). As mentioned before, Cr is attributed to the anticorrosive property of the ASS and CoCrMo, so if the Cr loss is realized in the lattice then automatically the material will be open to corrosion.

A recent study by X.L. Xi et. al. intended to study temperature effect on plasma nitrided austenitic stainless steel by plasma nitriding technique at 400 °C and 500 °C. TEM and XRD results suggested that the plasma nitrided layer produced at 500 °C is composed mainly of  $\alpha$  (bcc) and CrN phases, while there is no evidence found for CrN at 400 °C forming only  $\gamma_N$ . Another study (Stinville 2009) suggest this by adding CrN formation cannot be observed at 400 °C however long the plasma nitriding time (160 h). It is suggested the CrN would precipitate when raising the treatment temperature 500 °C. J. Lutz et. al. reported some comparative experimental data to calculate activation energies of stainless steel and CoCrMo alloys. Whereas temperature independent activation energy of 0.7-0.8 eV is obtained for stainless steel alloys, a more complex behavior was identified for CoCr alloys. For moderate temperatures between 300 and 450 °C activation energy identical to that of stainless steel of about 0.75 eV can be ascribed to CoCr alloys. At lower temperatures, a higher value of 1-1.1 eV can be assigned, whereas value 0.3-0.5 eV are found for higher temperatures. At moderate temperatures we can say that the activation energies are same both austenitic stainless steels and CoCrMo alloys.

Although the mechanical improvement of the surfaces of the nitrided metallic biomaterials is due to the interaction of nitrogen with the surfaces of the materials and the change in the microstructure as a result of nitrogen diffusion, in most nitriding treatments hydrogen is also used in combination with nitrogen. Hydrogen effects in nitriding has been studied by various research groups (Kumar 2000, Negm 2006, Priest 2001, Matsumo 1983, Renevier 1998, Hudis 1973, Ricard 1993, Szasz 1989). In spite of

that the role of hydrogen, in nitriding of stainless steels, still has contrary opinions, the general opinion supports its beneficency. Some of contrary results were reported by Matsumo et. al. and Renevier et. al. In spite of Matsumo's conclusion that the addition of hydrogen into the nitrogen plasma decreases the reaction rate, Renevier et. al. concluded that the addition of hydrogen gas has no effect. On the other side, Ricard et. al stated that it is enoguh to see impressive results by adding only a slight ammount of H<sub>2</sub> to N<sub>2</sub>. Szasz et. al. reported that small amount of hydrogen are found to be necessary for nitriding process. Moreover, this hydrogen increases the surface sticking coefficient for nitrogen, which is followed by nitrogen diffusion into the native material in the form of nitrogen vacancy pairs. Hudis mentioned that addition of hydrogen provides more effective surface cleaning (removing the surface oxide layer, Cr<sub>2</sub>O<sub>3</sub>) and therefore superior nitriding. Also he added that replacing hydrogen with argon or any inert gas reduces the thickness of the nitrided layers and hardness.

More explanatory study was done by Kumar et al. (Kumar 2000). Kumar et al. investigated the effect of hydrogen on the growth of the nitrided layer in RF plasma nitrided austenitic stainless steel at 400 °C and concluded that the addition of hydrogen in the range between 5-50 % increase nitrided-layer thickness compared to pure nitrogen plasma while an excessive amount of hydrogen in the gas mixture (75%) retards the nitriding process. Also, it was stated that the beneficial effect of hydrogen must be sought in the action of hydrogen atoms and molecules at the workpiece contrary to that hydrogen has reversal effect on creation of active nitriding species.

In addition to hydrogen and nitrogen gas mixtures, alternative mixtures such as nitrogen+argon, nitrogen+hydrogen+neon, and combination of these are used to enhance the rate of nitriding in the plasma nitriding process. In one such study (Karakan 2003), the role of hydrogen and argon on plasma nitriding of a low-alloy steel (AISI 5140) was investigated. This study showed that the amount of Ar in dual gas mixtures must be at least 20% to obtain distinctive hardness values.

#### **1.4. Purpose of This Work**

The main objective of this research is to improve our understanding of surface modification of CoCrMo metallic biomaterial with RF plasma nitriding process. In addition to structural and compositional changes, surface mechanical properties such as



hardness and wear behaviour of the plasma nitrided layers for 1, 2, 4, 6, 20 hour nitriding times respectively under N<sub>2</sub> 60% + H<sub>2</sub> 40% gas composition at 400 °C are investigated.

The near-surface crystal structures are investigated by using a combination of symmetric and grazing incidence x-ray diffraction (XRD and GIXRD) techniques. The scanning electron microscopy (SEM), atomic force microscopy (AFM) and optical interferometry techniques are used to characterize the surface properties of the plasma nitrided CoCrMo samples. Also, cross-sectional SEM, AFM and optical microscopy as well as differential interference contrast optical microscopy (DIC-OM) are used to estimate the thickness of the nitrided layers. Compositional characterization of the plasma nitrided phases and nitrogen concentration depth profiles are analyzed with the help of energy dispersive x-ray spectroscopy (EDX) and glow discharge optical emission spectroscopy (GDOES). Mechanical properties of microhardness and wear were characterized by Vicker's microhardness system and pin-on-disc wear tribo-tester.

The results of this research should lead to enhanced predictability of the effects of plasma nitriding conditions on the development of various near-surface crystal structures and to an understanding of the surface mechanical improvements of CoCrMo alloy.

## CHAPTER 2

### EXPERIMENTAL METHODS

#### 2.1. Sample and Sample Preparation

Cobalt-chromium-molybdenum (CoCrMo) alloy is the base material for this study. It is specified as ISO 5832-12. The CoCrMo samples for this study have disc-like geometry with the radii of 10 mm (D10), 15 mm (D15) and 30 mm (D30), respectively. D30 samples were used for wear resistance measurements. The thickness of the samples is 3 mm. Their chemical compositions in weight and atomic percentage (taken from TIPSAN) are given in Table 2.1. The CoCrMo alloy used in this study is fundamentally face-centered cubic (fcc- $\gamma$ ) accompanying some amount of hexagonal-closed packed (hcp- $\epsilon$ ) structure. The  $\epsilon$  phase exists as thin plates (bands) in the fcc  $\gamma$  CoCrMo matrix. Figure 2.1 represents the fcc crystal structure of CoCrMo.

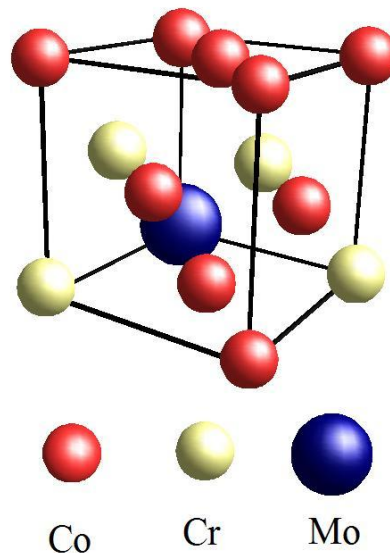


Figure 2. 1. Schematic diagram of fcc CoCrMo lattice.

Table 2. 1. Chemical composition of the CoCrMo alloy samples a) 30 mm (D30), b) 15 mm (D15), c) 10 mm (D10).

<b>a)</b>	Cr	Mo	Mn	Si	Al	Ni	C	Fe	N	Co
wt.%	27.10	5.60	0.81	0.59	0.036	0.07	0.06	0.08	0.19	Bal.
at.%	29.75	3.33	0.84	1.20	0.08	0.07	0.29	0.08	0.77	Bal.
<b>b)</b>	Cr	Mo	Mn	Si	Al	Ti	C	Zr	Fe	Co
wt.%	27.66	5.60	0.59	0.72	0.01	0.01	0.048	0.01	0.08	Bal.
at.%	30.78	3.38	0.62	1.48	0.02	0.01	0.23	0.01	0.08	Bal.
<b>c)</b>	Cr	Mo	Mn	Si	Cu	Ni	C	Fe	Al	Co
wt.%	27.66	5.72	0.57	0.38	0.01	0.44	0.033	0.31	0.01	Bal.
at.%	30.71	3.44	0.60	0.77	0.01	0.43	0.16	0.32	0.02	Bal.

Before RF plasma nitriding, all samples were polished by using a polishing system at IYTE. In polishing procedure described below, SiC grinding papers were used supplied from Buehler.

- i. First, with 320, 600, 800, 1200 grinding papers, 5 N forces applied for 5 minutes and 2400 grading paper, 5 N forces applied for 10 minutes. After each step, samples were cleaned in distilled water.
- ii. Second, with polishing cloths, 9  $\mu\text{m}$  diamond spray was used with 5 N forces for 10 minutes, 3  $\mu\text{m}$  diamond spray was used with 5 N forces for 15 minutes and 1  $\mu\text{m}$  diamond spray was used with 5 N forces for 20 minutes. After each step, samples were cleaned with ethanol in ultrasonic cleaner for 5 minutes, then cleaned in distilled water.
- iii. Last, with polishing cloth, alumina suspension (0.1  $\mu\text{m}$ ) was used with 2 N forces for 20 minutes. After that all samples were cleaned in ethanol ultrasonic cleaner for 10 minutes, then dried with nitrogen gas.

After polishing, substrate CoCrMo samples have reached 3 to 5 nm surface roughness as measured by AFM.

## 2.2. Plasma Nitriding

The plasma reactor, which is called URANOS (Unité de Réaction Assistée par plasma pour la Nitruration et l'Oxydation des Surfaces), used in this study was originally designed for the treatment of silicon in the 1980's in the CNET (Centre National d'Etude des Télécommunications) of Grenoble (Brevet International 1983). The plasma reactor URANOS dedicated to material treatment without any polarization, its potential is called the floating potential ( $V_F$ ), is different from conventional ion nitriding. The principal difference is plasma creation type. In this nitriding technique, the plasma is not a discharge; it is created by the intermediary of a field ratio operator frequency (13.56 MHz). An electromagnetic wave is propagated inside the quartz tube and ionizes the gas present in the enclosure; plasma diffuses then in the quartz tube and envelops the samples. A schematic diagram of the system is given in Figure 2.2. It combines the possibilities of heat treatment in reactive atmosphere and plasma treatment. URANOS reactor consists of four parts: a plasma chamber, a system of samples introduction, a pumping group and a radio frequency generator.

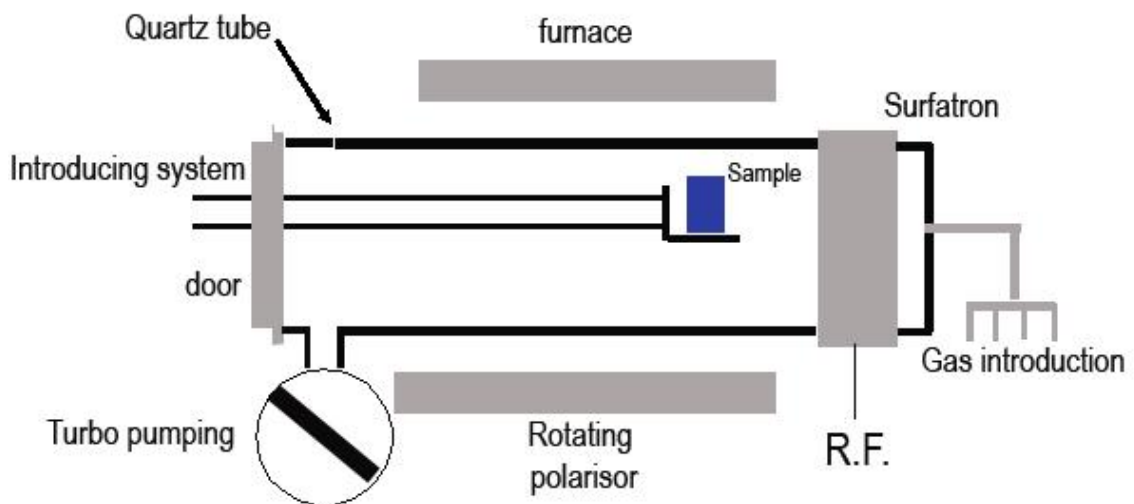


Figure 2. 2. The schematic diagram of RF Plasma Reactor.

The chamber constitutes of a quartz tube of 1.20 meter long and 18 cm in diameter. It is surrounded by a resistance furnace (with 90 cm of length) to achieve a maximum temperature of 1000 °C. The picture of RF Plasma reactor can be seen in Figure 2.2. The furnace is divided into three parts where the two sides are bonded to the central portion in order to maintain the temperature difference less than 1° in the central

area (50 cm). The temperature measurement is performed by three thermocouples located between the tube and the furnace. Ramp heating of the samples depends on the temperature. It takes about 30 minutes for the sample temperature to reach 700 °C and stabilize, which makes possible to have a homogeneous temperature over a length of two or three tens of centimetres. Moreover, the temperature can be controlled independently of the parameters of plasma power. It is possible to work from the ambient temperature to 1000°C.

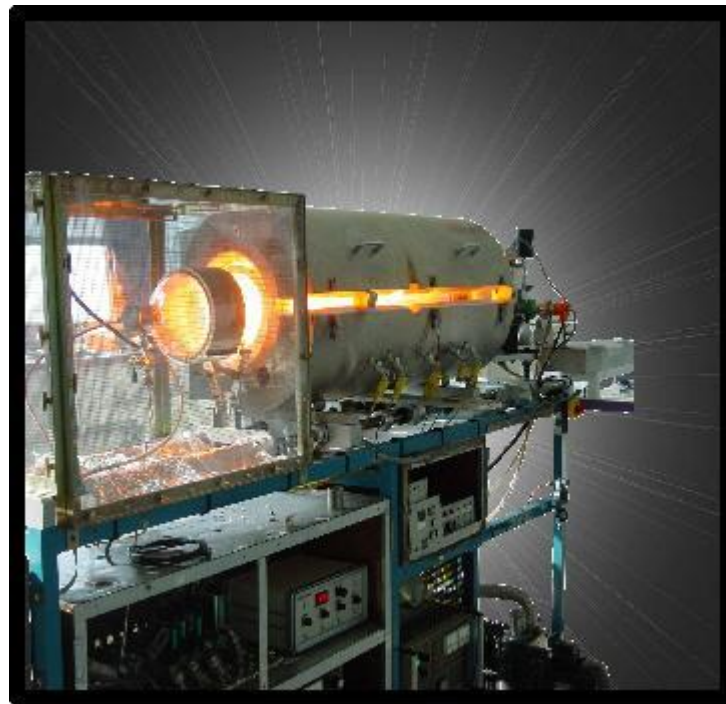


Figure 2. 3. RF Plasma Reactor.

The tube is a closed furnace having two introduction system; a sample introduction system with a mobile door and a gas introduction system with mass flow controllers. These two introductions are placed to two end of the tube. The sample introduction system includes a quartz sample holder consisting of two parallel and interdependent cantilever arms animated by an electric motor. This system also allows changing the position of the samples under vacuum. At first stage, the samples are introduced into outside of the tube (cold zone) and then, at second stage, and after vacuum enclosure, the samples are placed in the central part of the tube (hot zone). The reverse movement allows a rapid cooling of the sample without obligation to give air. In gas introduction system, several gas mixtures or solutions such as oxygen, nitrogen,

hydrogen and ammonia or their mixtures can be used according to experimental aims by regulating mass flow controllers.

The vacuum in the tube is done by two pumps: a primary pump and a turbo molecular secondary pump. During nitriding, the pressure control in the quartz tube is done by the intermediary of an electromagnetic slice gate drawer to variable conductance of type VAT. The nominal flow of primary pump, allowing  $10^{-2}$  Pa vacuum, is about  $19 \text{ m}^3/\text{h}$ . The turbo-molecular pump turning with the velocity of 6000 rev/min inhales the gas molecules in the tube. The high rotation velocity gives a good pumping for light gases. The pumping flow is about  $500 \text{ s}^{-1}$  for nitrogen resulting in a vacuum limit of  $1 \times 10^{-5}$  Pa ( $1 \text{ Pa} \sim 1.0 \times 10^{-5} \text{ bar} \sim 0.0075 \text{ torr}$ ) while the vacuum limit within the reactor is usually about  $5 \times 10^{-5}$  Pa. An automatically drawer valve and gas flow rates are used to enslave the pressure in the chamber during treatment (typically 0.1 mbar;  $1 \text{ atm} \sim 1 \text{ bar} \sim 1.0 \times 10^5 \text{ N/m}^2$ ).

In addition to this thermal processing equipment, low pressure system allows the generation of plasma. Radio-frequency generator consisting of a surfatron type electrode is placed around the quartz tube, following the gas introduction system (coupling zone). The radio-frequency generator delivers power through an impedance adaptation box. The plasma stabilization is realized by the intermediate of the impedance adaptation box allowing an optimal transfer of the forward power to the plasma. The efficiency of the gas ionization depends on the injected power, but, for this set-up, it has been shown to increase till a power of 600 W and to remain mostly constant for higher one. A forward power of 700 W was then chosen for all the experiments of this study. The plasma is created by the radio-frequency excitation (13.56 MHz). Obtaining plasma and a good transfer of energy to gas require an adjustment of the capacity of the box depending on the impedance of the gas, i.e. the pressure and temperature. The plasma created at the electrode diffuses and remains consistent throughout the tube (1.5 m) as the pressure is sufficiently low (less than 1 mbar). The lower the pressure in the interior of the tube, the more diffusion length of the excited species will be high. Therefore the gas is ionized all along the tube providing good homogeneity of the plasma in large volumes.

The functionality of this system is to give permission of combining heat treatment and plasma treatment simultaneously and independently as well. Any risk of pollution in the tube from its spray over the coupling zone is avoided by using an external electrode. Ions accelerated in this area can hit the walls of the chamber.

However, in the range of pressures used, the powdered particles having a mean free path of 0.1 cm undergo a large number of shocks and they are deposited back on the walls. Thus, sources of pollution are kept to a minimum.

### 2.2.1. Plasma Characteristics

The nitriding processes were performed by Prof. Dr. Jean Paul Riviere and his research group at PhyMat laboratories at Universite de Poitiers. The ions energies are mainly controlled by the wall temperature of the chamber. Under floating conditions (no bias), the sample surface is not bombarded by energetic ions and there is no sputtering. The various previous studies on this reactor have shown that the efficiency of gas ionization was dependent on the injected power but it does almost beyond 600 W. Therefore, a power of 700 W was chosen. For a pressure of 0.1 mbar ( $n_{\text{NH}_3} = 10^{15}$  atoms/cm<sup>3</sup>), one then gets an electron density of about  $10^{10}$  electrons/cm<sup>3</sup>, energy distribution of electrons around 3 to 5 eV. No current can cross the sample; its potential takes an equilibrium value compared to the plasma potential ( $V_P$ ) in order to push back the flow of the electrons. The floating potential ( $V_F$ ) is presented in Equation 2.1:

$$V_P - V_F = 5 kTe \quad (2.1)$$

As a consequence, the sample thus attracts the positive ions and accelerates them to energy of approximately  $\sim 15$  eV (for  $kTe \approx 3$  eV). This energy is quite lower than the threshold of sputtering of the majority of materials. No sputtering of the surface can thus occur during the treatment. The active species of neutral plasma (molecules, radicals) and excited ions reacts with surface and are absorbed, then diffuse in-depth in material under effect of the temperature. In addition to the initial composition of the materials, the parameters of nitriding like the nature and the composition of reactive gas, the temperature and the duration of the treatment, influence the morphology and the extent of the nitrided layers. Plasma is composed of electrons, ions ( $\text{N}_2^+$ ,  $\text{H}^+$  for example), radicals  $\text{NH}_x^*$  and also neutral species  $\text{N}_2$ ,  $\text{H}_2$ .

The samples are introduced automatically in the central part of the tube, pumping is done down to  $5 \times 10^{-4}$  Pa, the furnace temperature is increased, and the gas mixture 40% $\text{H}_2$  + 60%  $\text{N}_2$  (tested and optimized on austenitic stainless steels) is

introduced in the tube with a standard cubic centimeter flowing 50 sccm, then the plasma is produced with a power of 700 W; during nitriding the pressure inside the reactor is controlled at a value of 7.5 Pa. The sample is placed on an insulated holder and placed at the floating potential. They were flushed with dry nitrogen prior to introduction into the plasma reactor. No other cleaning procedure was applied.

The treatment cycle is the following:

- i. The samples are set on the sample holder of the reactor and moved to the working zone of the furnace.
- ii. The reactor is then pumped down to a pressure lower than  $5 \times 10^{-6}$  mbar (turbo molecular pump). This takes about 3 hours.
- iii. The samples are heated under vacuum to  $T_s = 360$  °C (furnace set at 370 °C) in one hour.
- iv. The desired gases are introduced in the reactor (60 sccm  $N_2$ , 40 sccm  $H_2$ ) and the pressure is set to 60 mTorr.
- v. The RF power (700 W) is then switched on giving extra heating of the sample up to  $T_s = 385-390$  °C.
- vi. The effective nitriding duration is counted from  $T_s = 385$  °C.
- vii. At the end of the process, the sample is moved to the “cold zone of the reactor” and cooled down to room temperature under 60 mTorr of flowing nitrogen.



Table 2. 2. RF plasma nitriding conditions.

Sample Name	# of Samples	Gas (sccm)		Working Pressure (mTorr)	Temperature (°C)			Reactor (W)	Cooling Ambiance	Heating Ambiance	Heating Time (min)	Treatment Duration (min)	Remark
		N <sub>2</sub>	H <sub>2</sub>		Nom.	Min.	Max.						
		D10-1h	2		60	40	60						
D15-1h	1	60	40	60	400	364	385	700	void	void	60	60	
D30-1h	1	60	40	60	400	364	385	700	void	void	60	60	
D15-2h	3	60	40	60	400	367	388	700	N <sub>2</sub>	void	60	150	
D30-2h	3	60	40	60	400	367	388	700	N <sub>2</sub>	void	60	150	
D10-4h	2	60	40	60	400	353	390	700	N <sub>2</sub>	void	60	250	
D15-4h	1	60	40	60	400	364	383	700	void	void	60	240	
D30-4h	1	60	40	60	400	364	383	700	void	void	60	240	
D15-6h	3	60	40	60	400	360	389	700	N <sub>2</sub>	void	55	385	15min without H2 at the beginning
D30-6h	3	60	40	60	400	360	389	700	N <sub>2</sub>	void	55	385	15min without H2 at the beginning
D15-20h	3	60	40	60	400	350	388	700	void	void	50	1225	
D30-20h	3	60	40	60	400	350	388	700	void	void	50	1225	

Table 2.2 shows the plasma nitriding conditions. The substrate temperature  $T$  was measured by thermocouples attached to the back of the samples. Figure 2.4 illustrates the nitriding temperature versus nitriding treatment time procedure for 1 hour plasma nitrided sample. The other plasma nitrided samples have the same type of temp vs. time procedures.

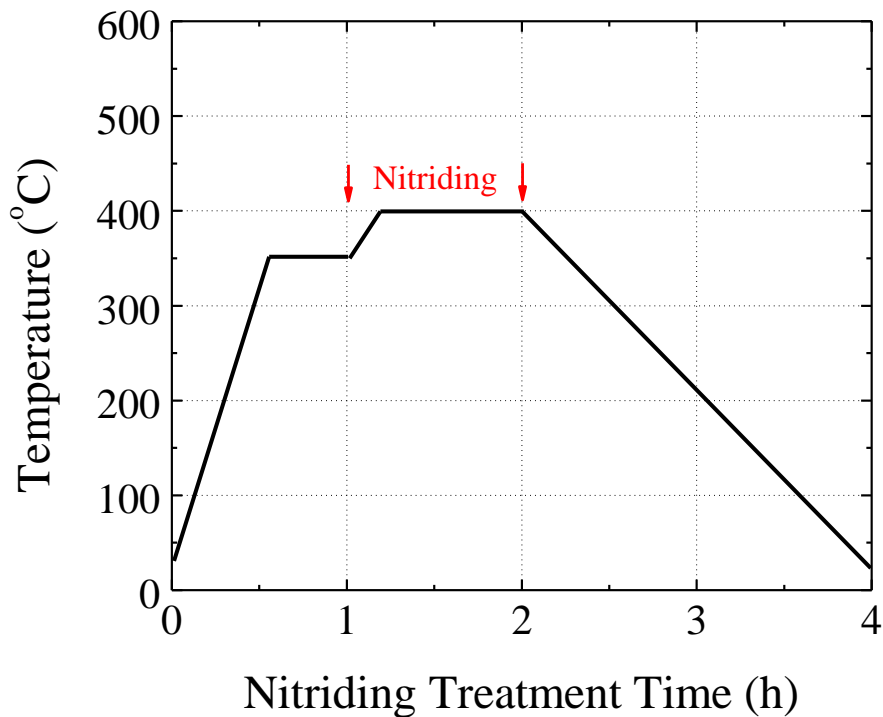


Figure 2. 4. Nitriding temperature versus nitriding treatment time for the 1 h nitrided specimen.

### 2.3. Cross-Sectional Sample Preparation

RF plasma nitrided samples were prepared for experiments which were aimed to analyze their cross-sections. Firstly, the plasma nitrided samples were cut into pieces by using wire electrical discharge machining (MAKINO'S U32j Wire EDM) technique (NEKA Kalıp, Organize Sanayi, Manisa. Electric discharge machining (EDM) is a manufacturing process whereby a work-piece is obtained using electrical discharges. Then, these pieces were mounted with bakalite by Struers CiroPress-1 (3 minutes heating and 3 minutes cooling) for ease of handling. The cross-sectional samples were polished by the polishing procedure described above. Lastly, the cross-sectional

samples were etched by two different techniques; electrochemical and  $\text{Ar}^+$  ion beam etchings.

### 2.3.1. Electrochemical Etching

In order to reveal the plasma nitrided layer, the polished cross-sections of the plasma nitrided CoCrMo samples were etched by a homemade electrochemical etching system. Figure 2.5 represents the schematic illustration of the electrochemical etching system. The etchant used in electrochemical etching was 5 ml HCl and 100 ml  $\text{H}_2\text{O}_2$ . The voltage and the current applied during electrochemical etching were 5 V and 1 mA for 30 seconds.

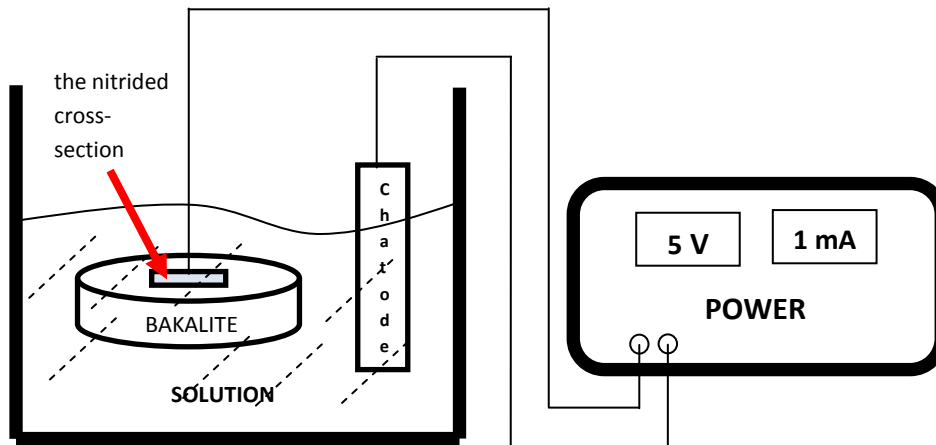


Figure 2. 5. The schematic diagram of electrochemical etching system.

### 2.3.2. $\text{Ar}^+$ Beam Etching

$\text{Ar}^+$  beam etching on the nitrided cross-sections were carried out to reveal the plasma nitrided layers, specifically to determine the nitrided layer thicknesses.  $\text{Ar}^+$  beam etching was done in a sputtering system. The energy of the  $\text{Ar}^+$  ions were 400 eV. Firstly, the cross-sections of the nitrided samples were etched by  $\text{Ar}^+$  ions for 30 minutes at the angle of  $62.5^\circ$ , but the nitrided layers could not be observed. Then, the cross-sections of the nitrided samples were etched by  $\text{Ar}^+$  ions for 4x15 min (60 min) at the angle of  $90^\circ$ . The second etching was done with liquid nitrogen to keep the temperature constant therefore to avoid melting the mounting resin (bakalite) that surrounds the plasma nitrided CoCrMo.

## **2.4. Microstructural and Compositional Characterization**

In this study, microstructures and compositions of the formations on the CoCrMo samples due to the RF plasma nitriding were analyzed by using various kinds of analytical techniques such as:

- X-Ray Diffraction (XRD): Bragg-Brentano XRD and Grazing Incidence XRD
- Optical Spectroscopy (OS): Optical Microscopy (OM) and Differential Interference Contrast Microscopy (DIC-M)
- Atomic Force Microscopy (AFM)
- Scanning Electron Microscopy (SEM): Energy Dispersive X-Ray Spectroscopy (EDX), Scanning Electron (SE) and Back Scattering Electron (BSE) Microscopy
- Optical Interferometry (OI)
- Glow-Discharge Optical Emission Spectroscopy (GDOES)

All these techniques have different benefits in terms of analytical approach. The aims of the analyses were to investigate the resulting near surface crystal structures by XRD and GIXRD, compositions by EDX and GDOES, surface morphology by SEM, AFM and OM, nitrided layer thicknesses by SEM, OM and AFM, surface roughness by AFM and OI after the plasma nitriding. The data obtained from these analyses were also used in semi-quantitative calculations, which will be discussed later.

### **2.4.1. XRD Analysis**

X-ray diffraction has a long history in material characterization field starting with its accidental discovery by Röntgen in 1895. X-rays have been used for decades to study the structure of the bulk crystalline materials. Basically, the information is obtained by the diffraction of x-rays by a crystalline material, which is a process of scattering of the beam by the electrons associated with the atoms in any crystal. Destructive and constructive interferences of these scattered x-rays due to the periodic arrangement of the atoms in the crystal and its symmetry have main role for identification of materials by creating different x-ray patterns for any individual material. In spite of that x-rays have been mainly used for identification of unknown

compounds and phases by the following of its discovery, nowadays, its investigation capabilities show wide range of diversity and help researchers for reaching valuable information about their materials such as composition, phase transformation, texture, stress in crystal lattice, refractive indices, roughness and even layer thickness. Mathematical methods are commonly being used for many applications, including profile fitting to obtain peak positions and resolve overlapped peaks; full-pattern fitting to find accurate lattice parameters and determine to crystal properties such as crystallite size and strain.

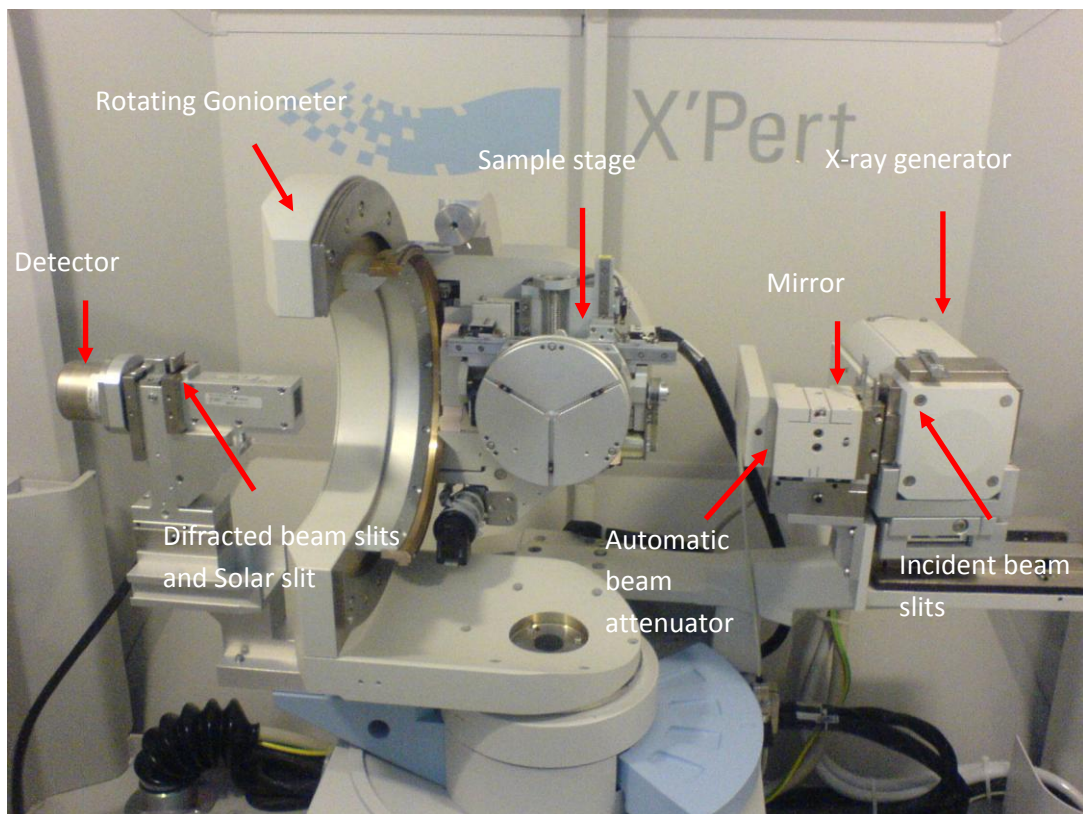


Figure 2. 6. The graph shows Thin Film Philips X'Pert Pro MRD System which is used for XRD experiments in this study

Over a few decades, various companies have built complex X-Ray Diffraction machines to perform different kinds of X-ray diffraction tasks in order to obtain more detailed data. In our studies, Philips X'Pert Pro MRD System Thin Film X-Ray Diffraction machine (illustrated in Figure 2.6), which was facilitated by Physics Department of Izmir Institute of Technology, is used in order to gain knowledge about microstructure of plasma nitrided samples. The fundamental physical and chemical knowledge obtained by these analyses were that of crystal structure identification, layer

thickness determination and composition, expansion of cells, crystallite sizes and texture evolution.

#### **2.4.1.1. Bragg-Brentano Method**

The process of reflection is described in terms of incident and reflected (or diffracted) rays, each making an angle  $\theta$  with a fixed crystal plane. Reflections occur from planes set at angle  $\theta$  with respect to the incident beam and generates a reflected beam at an angle  $2\theta$  from the incident beam. The possible d-spacing defined by the indices  $h, k, l$  are determined by the shape of the unit cell. Rewriting Bragg's law is shown in Equation 2.2:

$$2d\sin\theta = n\lambda \quad (2.2)$$

In the experiments, Cu-K $\alpha_1$  ( $\lambda=1.5406 \text{ \AA}$ ) x-rays was used. The x-ray generator voltage and current were held at 45 kV and 40 mA, respectively. The x-ray generator was fixed in this experiment while the sample and the detector were allowed to rotate along a goniometer circle on the sample-detector plane, the sample being at the center of the circle. The samples rotate  $\theta$  while the detector rotates  $2\theta$ . The reflection angle  $2\theta$  was varied from  $30^\circ$  to  $90^\circ$  with a signal time of 0.5 s/step. The scanning range was narrowed down to  $35^\circ$ - $55^\circ$  to focus on the peaks of interest. The data collection was made with a computer-controlled system.

A mirror was also positioned between the source and the sample holder, to maintain parallel incident beams on the sample surface at all times. To narrow the beam and decrease anti-parallel scattering,  $\frac{1}{2}$  mm wide slit was placed at the exit of the mirror. Also, solar slit was placed in front of the detector in order to parallel the diffracted beams arriving at the detector. This has an advantage of reducing sensitivity to sample displacement from the rotation axis.

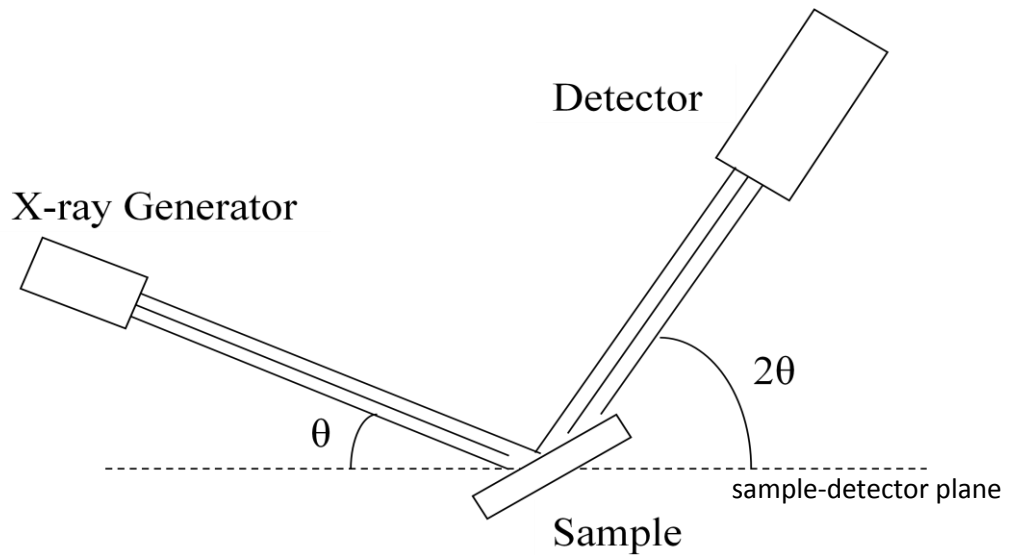


Figure 2. 7. Schematic diagram of an x-ray diffractometer illustrating its main components and the angular shift.

One disadvantage of this geometry is that the effective depth probed by the incident beam always changes during the scan due to the change in the angle of the incident beam. Due to change in the incident beam angle, the effective depth probed by the beam at  $2\theta = 90^\circ$  degree is approximately 3 times deeper than the effective depth probed by the beam at  $2\theta = 30^\circ$  degrees. This property of the method might cause some misinterpretation if it is not taken notice on examining for example, a material having a layered-structure. This introduces the concept of fixing the angle of the incident beam and scanning the scattered beam.

#### 2.4.1.2. Grazing Incidence X-Ray Method

In GIXRD measurements, the grazing angles were kept at the angles of  $0.25^\circ$ ,  $0.5^\circ$ ,  $1^\circ$ ,  $2^\circ$ ,  $3^\circ$ ,  $4^\circ$ ,  $5^\circ$  and  $10^\circ$ , respectively in order to analyze the peaks and peaks shifts. The aim was to obtain further information about near-surface changes with respect layer depth. The grazing incidence geometry is surface selective, largely avoids scattering from the substrate. It is difficult to analyze thin films and coatings because of their small diffracting volumes resulting in low diffracted intensities compared to substrate and background. High background and substrate signals make difficult to identify the phases formed on substrate. Being different from the Bragg-Branteno method, GIXRD facilitates diffraction from the planes which are not parallel to the

sample surface. Normally this method uses very small incident angles providing information from quite thin layers. The main power behind this method involves providing the information layer by layer just changing the incident beam angle on the sample surface. Since the effective depth probed by the fixed x-ray beam incident on the sample is mainly dependent on the grazing angle ( $\sin\omega/\mu$ , where  $\omega$  is the fixed angle and  $\mu$  is the mass absorption coefficient (Cullity 1956)).

Figure 2.8 shows the grazing incidence geometry used in this study. For the thin film arrangement, the incident and diffracted beams are made nearly parallel with the help a narrow 1/32 slit on the incident beam and a long soller slit on the detector side. During the collection of the diffraction spectrum, only the detector rotates through the angular angle, thus keeping the incident angle, the beam path length, and the irradiated area constant. In addition, the stationary incident beam makes a very small angle with the sample surface, which increases the path length of the x-ray beam through the films or coatings. This helps to increase the diffracted intensity while at the same time, reduces the diffracted intensity from the substrate. Overall, there is a dramatic increase in the film signal to the background ratio.

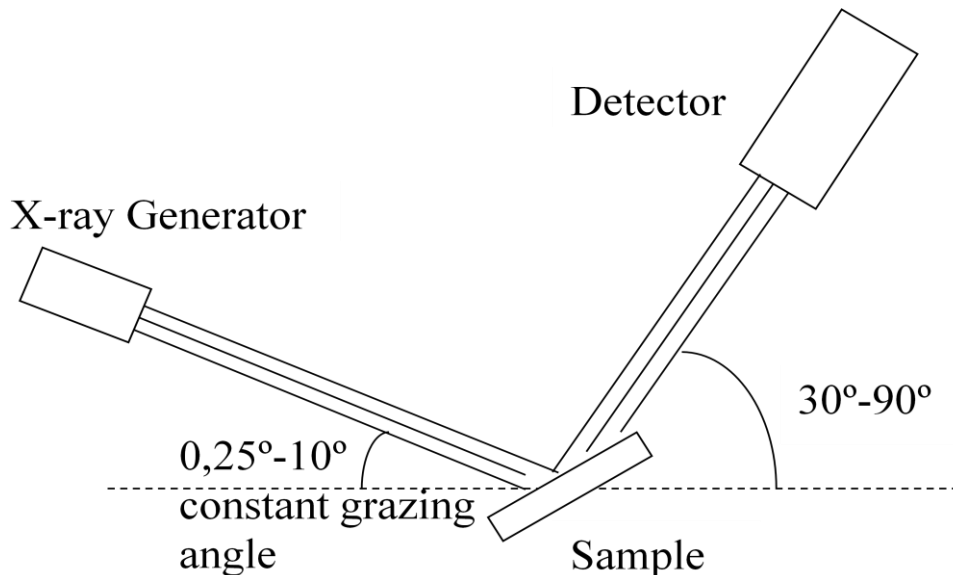


Figure 2. 8. Schematic diagram of GIXRD measurements.

Due to extremely low incident angles the scattered beam mainly lacks of enough intensity and parallelism, which might lead to missing or wrong information. Using Göbel mirror and parallel beam optics may solve this problem.



### **2.4.2. Optical Spectroscopy**

In order to characterize the substrate and plasma nitrided surfaces and cross-sectional plasma nitrided samples, the optical spectroscopy was used. The images from optical microscope were taken under different magnifications ranging from 10X to 100X. The images were acquired by using a digital camera connected to a computer. Also, images of cross-sectional plasma nitrided samples were obtained by using differential interference contrast optical microscopy (DIC). Differential interference contrast microscopy is an optical microscopy illumination technique mainly used to enhance the contrast in samples. DIC works on the principle of interferometry to gain information about the optical density of the sample, to see invisible features.

### **2.4.3. SEM Analysis**

In the experiments, Philips XL-305 FEG Scanning Electron Microscope SEM techniques were used to analyze topographical changes on the surface of plasma nitrided CoCrMo samples as well as to measure the thicknesses of the nitrided layers from the nitrided sample cross-sections. EDX mode was also used to characterize the chemical compositions of the plasma nitrided CoCrMo samples.

### **2.4.4. Atomic Force Microscopy**

AFM analysis was used to investigate surface morphology and roughness ( $R_a$ ) of polished and plasma nitrided samples. Atomic force microscopy (AFM) was invented in 1986 by Gerd Binnig, Calvin F. Quate and Christopher Gerber (G. Binnig 1986). The AFM working principle is the measurement of the interactive force between a tip and the sample surface using special tips made by an elastic cantilever with a sharp tip on the end. It can be seen a schematic working principle of AFM in Figure 2.9. The force applied to the tip by the surface, results in bending of the cantilever. By measuring the cantilever deflection, it is possible to evaluate the tip-surface interactive force.

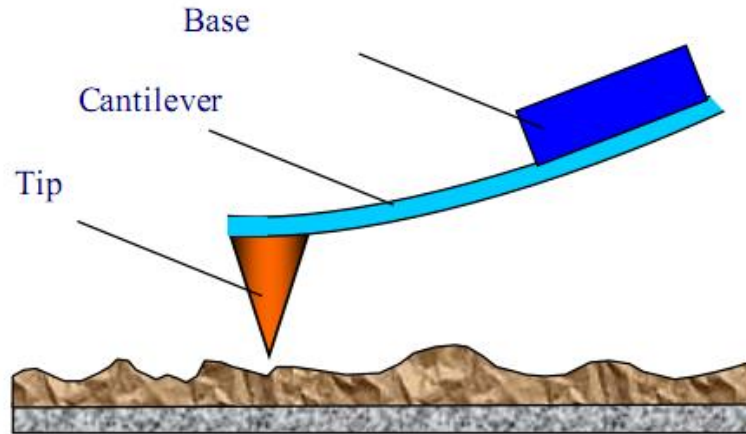


Figure 2. 9. A schematic picture of AFM cantilever.

Lenard-Jones potential allows estimating the interaction force of a tip with a sample. The energy of the tip-sample system can be derived, adding elementary interactions for all the tip and sample atoms. In order to detect changes in the amplitude and in the phase of cantilever oscillations in non-contact mode high sensitivity and stability of the feedback is required. In practice the so-called 'semi-contact' (also named tapping mode) is used more frequently. In this technique the forced cantilever oscillations are excited near a resonance frequency with an amplitude about 10-100 nanometers.

AFM surface characterization was performed in semi-contact (tapping) mode by using commercial AFM (Solver Pro 7 from MNT-MDT, Russia). During all scans a conductive diamond like carbon coated tip (DLC tip from the same company) with a curvature of 75 nm was employed, and the closed loop feedback system was kept active. Current information and scanner tips positions recorded by a computer. The scan area for all the samples was the 30  $\mu\text{m}$  x 30  $\mu\text{m}$  and for each sample several scans on different regions were performed.

#### **2.4.4.1. Roughness Measurements**

Surface roughness measurements were performed on both as-polished substrate and plasma nitrided samples by using AFM and surface optical interferometer. During plasma nitriding processes material surfaces are subjected to different expansions of differently oriented grains (due to nitrogen) which might be detrimental to the surface

quality. To get an idea about roughness of the surfaces and the effects on the specimens of each process, the specimens were subjected to roughness measurements: roughness profiles and mean roughness values were obtained. The roughness values were obtained from several measurements.

## **2.5. PeakFit Program**

The PeakFit program was used in quantitative investigations of characteristic x-ray spectrum of both substrate and plasma nitrided samples, particularly to estimate an average nitrided layer thickness and an average nitrogen concentration value for the nitrided layers. In Peakfit, any x-ray spectrum is fitted by using various mathematical equations. Such quantitative properties; accurate  $2\theta$  peak positions, full-width-of-half-maximums, integrated areas of peaks, etc. are identified after fittings.

Any XRD peak can consist of one or more characteristic peaks. If any x-ray spectrum has hidden peaks (other characteristic phase peaks or the peaks resulted from stresses in the crystal lattice) or large background and noise, the values from this spectrum can lead us to misinterpretations of the peaks. Therefore, it will be more convenient for obtaining more accurate results to use fitted spectrums that have importance in characterization like in this study.

## **2.6. Compositional Characterization**

In this study, compositional characterization of substrate and plasma nitrided samples was investigated with the help of glow discharge optical emission spectroscopy (GDOES) and energy dispersive x-ray spectroscopy (EDX). Also, the nitrogen concentration depth profiles were obtained from GDOES.

## **2.7. Mechanical Characterization**

In this study, mechanical characterizations of the RF plasma nitrided specimens were analyzed by using the techniques such as:

- Vicker's Microhardness measurements
- Pin-on-disc Wear analysis

These two techniques have different benefits in terms of analytical approach. The aims of the analyses were to investigate the resulting mechanical properties of near surface crystal structures and to compare with mechanical properties of substrate CoCrMo.

### 2.7.1. Microhardness Measurements

In this study, SHIMADZU HMV-2000 model microindenter was used to perform microhardness measurements. This tester uses the indentation hardness test method. In this tester, the Vickers indenter (a diamond in the form of a right pyramid with a square base having the angle between the opposite faces at the vertex of 130°) for a Vickers hardness is available. Vickers hardness is determined based on the test load used when penetrating a Vickers indenter on the surface of test piece and the indentation area calculated from the indented diagonal length. The microhardness values were obtained from the following formula:

$$HV=0.1891 \frac{F}{d^2} \quad (2.3)$$

HV: Vickers hardness

F: Test load (N)

d: Mean of the indentation diagonal length (mm)

The surface hardness profiles of the polished and the plasma nitrided samples were obtained as a function of the indenter load. The loads and the corresponding Vickers numbers were 5 g (HV 0.005), 10 g (HV 0.01), 25 g (HV 0.025), 50 g (HV 0.05), 100 g (HV 0.1), 200 g (HV 0.2), 300 g (HV 0.3), 500 g (HV 0.5), 1000 g (HV 0.1). For each indentation, experiments were repeated several times and average values were calculated. The hardness values of HV 0.005 and HV 0.01 of the plasma nitrided samples were not measured directly by optical microscope connected to the system due to limitation of resolution of the optical microscope used. The hardness values of HV 5 and HV 10 of the plasma nitrided samples were investigate by scanning electron microscope.

### 2.7.2. Wear Test (Pin-on-disc and Oscillating TRIBOTester)

Tribological testing was done on the polished substrate and 2, 6 and 20 h plasma nitrided samples by using a ball-on-disc wear tester under dry cyclic sliding motion. During the measurements, 6 mm ruby ball was used to form wear tracks on the surface of the selected samples. 1 and 4 N loads were applied to the nitrided specimens with the sliding wear distances of 200 and 600 m. Under these loads, the ball induces wear tracks circumferentially around the disc at predetermined radius that was chosen to be 7, 8, 10 and 11 mm respectively. Assuming that each rotation of the testing sample under wear mode corresponds to the cyclic load of the samples, the measurement then can be carried out based on the number of laps of the rotational motion (100 rpm).

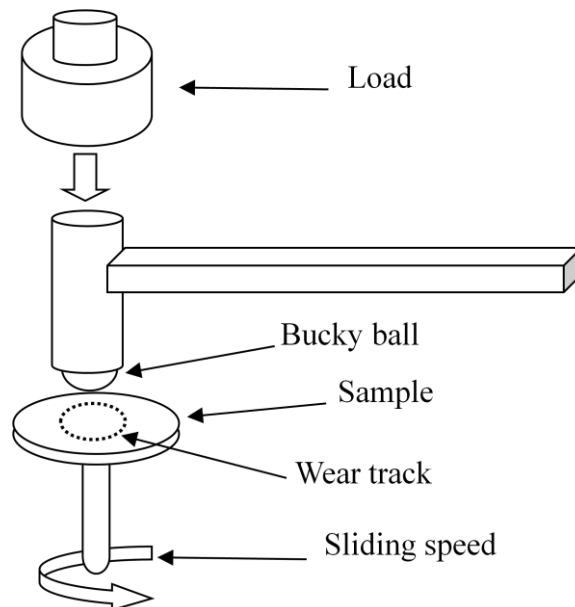


Figure 2. 10. Schematic diagram of wear test.

During all the measurements no lubricant was used (i.e. dry sliding) and the measurements were carried. When the tests were finished quantitative wear results were obtained from the optical interferometer. Also, optical microscopy were used to measure the wear widths. Probing the wear track by the profilometer, the area of the wear tracks as well as the wear profiles are obtained.

## CHAPTER 3

### DATA ANALYSIS AND MODELING

#### 3.1. XRD Data Curve Fitting

Experimental XRD data were fitted by a non-linear least-squares curve-fitting program (PeakFit v4.11) to obtain accurate peak centers and integrated intensities (areas under the fitted curves) for both the nitrated and the substrate phases. These quantities were then used in estimating the volume fractions of the substrate  $\gamma$  phase to the substrate  $\epsilon$  phase, lattice constants of substrate and plasma nitrated samples, N concentration and nitrated layer thicknesses. The fitting function used was Pearson VII (a four parameter function with two width parameters; according to the variation of one of the parameters, this function becomes either Lorentzian or Gaussian). Such quantitative properties of accurate  $2\theta$  peak positions, full-width-of-half-maximums, integrated areas of peaks, etc. of any XRD spectrum are identified after curve-fits. Figure 3.1 illustrates an actual curve-fit result of one hour plasma nitrated CoCrMo sample.

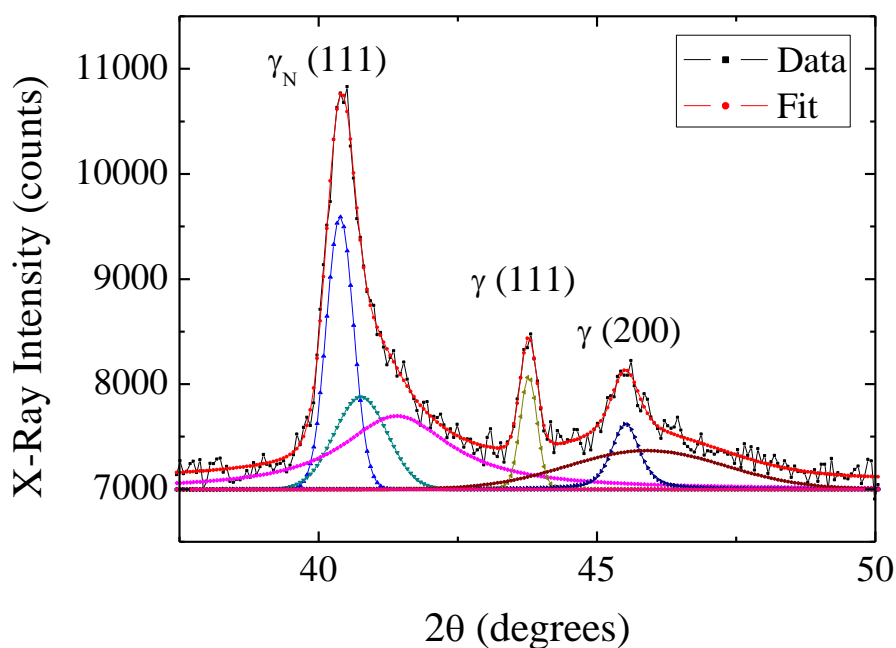


Figure 3. 1. Curve-fit of XRD data of 1 h plasma nitrated CoCrMo sample (D15).

As can be seen from Figure 3.1, any peak may consist of one or more one peaks. For example, the XRD data labeled as  $\gamma_N$  (111) is fitted with 3 peaks. If any x-ray spectrum has hidden peaks (other characteristic phase peaks or the peaks resulted from stresses in the crystal lattice) or large background and noise, the values from this spectrum can lead us to misinterpretations of the peaks. Therefore, it will be more convenient to use curve-fitted XRD spectrums for obtaining more accurate results.

### 3.2. Epsilon Phase Analysis

As stated before, CoCrMo substrate materials used in this study has two different crystal phases, mainly face centered cubic (fcc)  $\gamma$ -(CoCrMo) and hexagonal closed packaged (hcp)  $\epsilon$ -(CoCrMo), in bulk. The  $\epsilon$ -(CoCrMo) phase is considered to be distributed as thin plates within the  $\gamma$ -(CoCrMo) matrix. In Chapter 4, the role of  $\epsilon$ -(CoCrMo) phase during plasma nitriding will be discussed more.

Figure 3.2 shows curve-fit results of CoCrMo substrate (D10) XRD data. In this figure, red line represents the curve-fit result while the black one represents the actual XRD data. After the curve-fit of the CoCrMo substrate XRD data, the integrated areas of  $\gamma$ (200) and  $\epsilon$ (101) peaks are calculated in order to find the volume fraction of  $\gamma$ -(CoCrMo) and  $\epsilon$ -(CoCrMo) by using Equation 3.1.

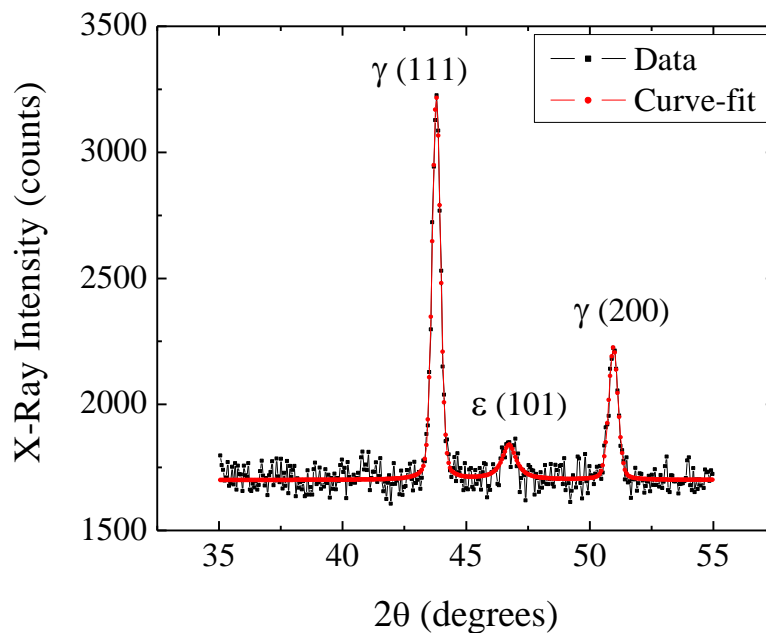


Figure 3. 2. Curve-fit of the CoCrMo substrate XRD data (D10).

Based on the integrated intensities (Chiba 2007) of the  $\gamma(200)$  and the  $\epsilon(101)$ , the volume fractions of  $\epsilon$ -phase in substrate samples (D10, D15, D30) are estimated. The Equation 3.1, below, is used to calculate the volume fraction of  $\epsilon$ -(CoCrMo) phase.

$$\text{volume fraction} = \frac{\epsilon(101)}{\epsilon(101) + \frac{3}{2}\gamma(200)} \times 100 \quad (3.1)$$

### 3.3. Lattice Parameter and Nitrogen Concentration Analyses

The lattice parameter ( $a_0$ ) of the substrate material phase  $\gamma$ -(Co,Cr,Mo) was calculated as 3.579 Å (very close to lattice parameter of 316L SS, 3.573 Å (O. Öztürk 2009)) by the method of least squares and linear fit (Cullity 1956). Figure 3.3 represents Nelson-Riley plot of CoCrMo substrate (D10), which shows fcc lattice constants in different crystallographic directions and linear fit. In Figure 3.3, the linear fit of substrate lattice constant can be seen as almost straight line. According to Figure 3.3, the crystal structure of CoCrMo substrates used in the study has mainly face-centered-cubic (fcc) crystal structure. Slight differences of lattice constants of different crystallographic directions may be due to low internal stresses in fcc crystal lattices. Also, hcp phase distribution may contribute the differences between lattice constants of fcc crystallographic directions.

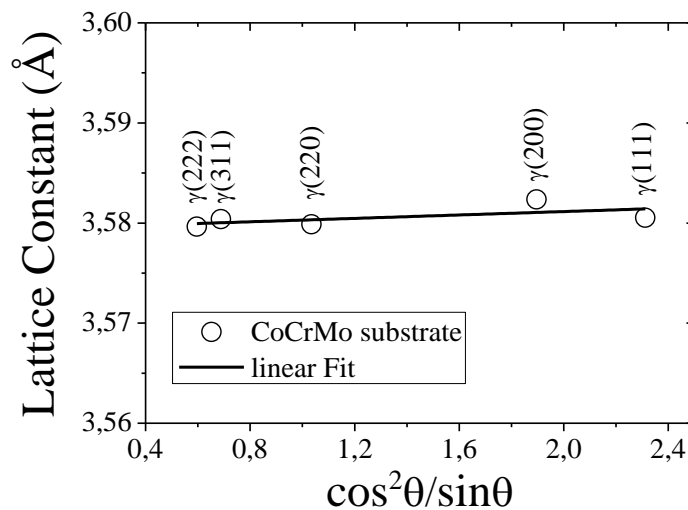


Figure 3. 3. Nelson-Riley plot of the CoCrMo substrate sample (D10).



After PeakFit simulations, obtained accurate peak positions ( $2\theta$ ) are used in equations below to obtain the lattice constants and lattice expansions of different crystallographic directions.

$$2d \sin \theta = n\lambda \quad (3.2)$$

$$d = \frac{a}{(h^2 + k^2 + l^2)^{1/2}} \quad (3.3)$$

$$\frac{\Delta a}{a} = \frac{a_N(\text{hkl}) - a_0(\text{hkl})}{a_0(\text{hkl})} \quad (3.4)$$

In above equations,  $d$  represents the distance between the same fcc crystal planes,  $\theta$  is characteristic x-ray diffraction angles from different fcc crystal planes,  $\lambda$  is wavelength of the  $\text{CuK}\alpha$  used in XRD experiments whose value is  $1,5402 \text{ \AA}$ , respectively  $h$ ,  $k$  and  $l$  are Miller indices and  $n$  is the integer, generally used as 1.

Equation 3.5 is used to estimate an average nitrogen concentration for the  $\gamma_N$  layers of plasma nitrided CoCrMo samples. This is done by careful examination of the plasma nitrided  $\gamma_N$  (111) and  $\gamma_N$  (200) peaks and the substrate  $\gamma$  (111) and  $\gamma$  (200) peaks. The lattice constants;  $a_N$  and  $a_0$  found from previous equations are used in Equation 3.5 in order to estimate nitrogen concentrations of different crystallographic planes,  $C_N$  (111) and  $C_N$  (200). XRD nitrogen composition analysis is done by using the following formula;

$$a_N = a_0 + \alpha C_N \quad (3.5)$$

This is a well established equation for the lattice constant of  $\gamma$ -Fe (fcc) as a function of atomic percent interstitial nitrogen up to  $\sim 10 \text{ at. \%}$  (Ozturk 1995). This equation can be applied to materials and alloys with fcc structure. In this equation, as applied to the  $\gamma_N$  layer,  $a_0$  is the lattice constant of the substrate  $\gamma$ -(CoCrMo),  $C_N$  is the atomic percent N concentration for the  $\gamma_N$  layer,  $\alpha$  is known as Vegard's constant and equals to  $0.0078 \text{ \AA/at.\%N}$  for pure  $\gamma$ -Fe (Ozturk 1995). In literature, Vegard's constant is given as  $0,0080 \text{ \AA/at.\%N}$  for 300 series stainless steels (304, 310, 316, 316L). There is no actual data for Vegard's constant of  $\gamma$ -(CoCrMo) in literature. The constant is assumed as  $0,0080 \text{ \AA/at.\%N}$  for  $\gamma$ -(CoCrMo) used in this study relying on a study that

316L SS, which has also fcc crystal structure, was nitrided by the same technique and the value of constant was used in estimating the N concentrations (Öztürk 2009).

### 3.4. Layer Thickness Analysis

The thickness of the plasma nitrided grains are calculated (Ozturk 1995) by using x-ray diffraction datas. In this calculations,  $2\theta$  peak centers, the integrated areas under the XRD peaks of the nitrided samples and linear mass absorption coefficients ( $\mu$ ,  $\mu[N]$ ) are used.

In order to accomplish these quantitative investigation, firstly, the linear mass absorption coefficients are calculated for both substrate and plasma nitrided samples. The linear mass absorption is different for plasma nitrided samples (the linear mass absorption coefficient is different for each material in nature and it represents the way which x-rays takes in that material (Cullity 1956)). In order to calculate the linear mass absorption coefficient of plasma nitrided samples, the model, presented in Figure 3.5., are suggested. According to the model, the mass absorption coefficient was calculated either the nitrogen occupies the octahedral sites in CoCrMo fcc crystal structure or not. From the model, two linea mas absorption coefficients ( $\mu$  and  $\mu[N]$ ) were calculated.

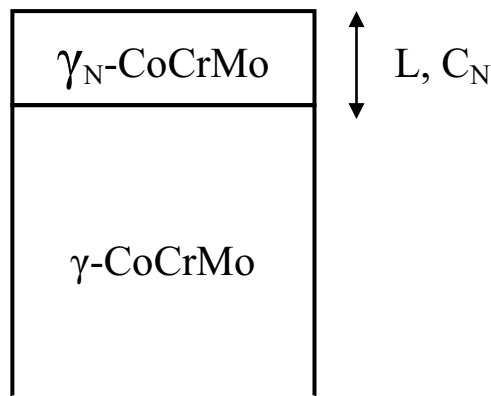


Figure 3. 4. The model for calculation of the linear mass absorption coefficient.

Below, Equation 3.7 represents the general formula that is used to calculate linear mass absorption coefficient of any substance. Equation 3.8 is used to calculate linear mass absorption coefficients of CoCrMo sample according to the model

illustrated above. Also, Table 3.4 lists the GDOES values used in linear mass absorption coefficient calculations. The elemental composition data of substrate and plasma nitrided samples used in Equation 3.8 are taken from GDOES compositional characterization experiments.

$$\mu_x = \rho_x \sum_i \omega_i \frac{\mu_i}{\rho_i} \quad (3.6)$$

$$\begin{aligned} \left(\frac{\mu}{\rho}\right)_{\text{CoCrMo}} &= (\text{wt. \%})_{\text{Co}} \left(\frac{\mu}{\rho}\right)_{\text{Co}} + (\text{wt. \%})_{\text{Cr}} \left(\frac{\mu}{\rho}\right)_{\text{Cr}} + (\text{wt. \%})_{\text{Mo}} \left(\frac{\mu}{\rho}\right)_{\text{Mo}} \\ &+ (\text{wt. \%})_{\text{Mn}} \left(\frac{\mu}{\rho}\right)_{\text{Mn}} + (\text{wt. \%})_{\text{Si}} \left(\frac{\mu}{\rho}\right)_{\text{Si}} + (\text{wt. \%})_{\text{N}} \left(\frac{\mu}{\rho}\right)_{\text{N}} \end{aligned} \quad (3.7)$$

Table 3. 1. The values used in estimation of linear mass absorption coefficients for both substrate and plasma nitrided samples.

	Linear Mass Absorption Coefficient ( $\text{cm}^{-1}$ )	Density ( $\text{g}/\text{cm}^3$ )	Wt.% (without N)	Wt.% (with N)
Co	338.6	8.8	66.28	57.70
Cr	252.3	7.19	27.41	29.34
Mo	158.3	10.22	5.73	03.92
Mn	272.5	7.47	0.6767	00.63
Si	65.32	2.33	0.888	00.74
N	7.142	0.001165	-	07.67

According to the values and the equations, the linear mass absorption coefficients were calculated as  $2129 \text{ cm}^{-1}$  according to first model (N occupies octahedral sites) and as  $2530 \text{ cm}^{-1}$  according to second model (no N occupies octahedral sites). These calculations suggest that the substrate  $\gamma$ -(Co,Cr,Mo) is denser than the structure with nitrogen  $\gamma_{\text{N}}$ -(Co,Cr,Mo) and x-rays penetrate more in nitrided grains. Table 3.5 lists the estimated linear mass absorption coefficients and the coefficient of the previous study. The difference between the linear mass absorption coefficients is nearly 16% for two model.

In the previous study (Turkan 2004), the mass absorption coefficient value of CoCrMo is calculated as  $2540 \text{ cm}^{-1}$  (without nitrogen). The value found in this study is  $2530 \text{ cm}^{-1}$ , very close to Turkan's mass absorption coefficient. The difference probably

arises from slight differences in chemical compositions of both CoCrMo alloys used in these experiments.

Table 3. 2. The linear mass absorption coefficients ( $\text{cm}^{-1}$ ).

$\gamma_{\text{N}}$ -CoCrMo	2129
$\gamma$ -CoCrMo	2530
$\gamma$ -CoCrMo (Turkan 2004)	2540

The thickness of the nitrided layers are calculated according to the two linear mass absorption coefficients found above. Also the integrated areas under the peaks  $\gamma$  and  $\gamma_{\text{N}}$  reflections are found by curve-fit analysis. The following equation (Equation 3.8) is used in estimating the  $\gamma_{\text{N}}$  layer thicknesses.

$$\frac{I(\gamma_{\text{N}})}{I(\gamma)+I(\gamma_{\text{N}})} = 1 - \exp\left(\frac{-2\mu L}{\sin\theta}\right) \quad (3.8)$$

In this equation,  $\mu$  is the linear mass absorption coefficient and  $\sin\theta$  is the average value for both phases ( $\gamma$  and  $\gamma_{\text{N}}$ ). The main assumption used in deriving this equation is that the  $\gamma_{\text{N}}$  layer extends uniformly from the surface to a depth  $L$  with an average concentration ( $C_{\text{N}}$ ) (see Figure 3.5). Also, in this equation,  $I(\gamma_{\text{N}})$  refers to the integrated intensity of the  $\gamma_{\text{N}}$  layer while  $I(\gamma)$  refers to that of substrate  $\gamma$  phase. It is considered that (111) and (200) oriented plasma nitrided layers have different thicknesses. This will be evaluated in details in the experimental results chapters.

## CHAPTER 4

### PLASMA NITRIDED CRYSTAL STRUCTURES

#### 4.1. XRD Results

Figure 4.1 shows the XRD spectrum of the polished CoCrMo substrate (D15) sample between the angles  $30^\circ$  and  $100^\circ$ . As stated before, CoCrMo substrates have dual crystal structures, fcc  $\gamma$ -(CoCrMo) and hcp  $\epsilon$ -(CoCrMo) structures, which are labelled as  $\gamma$ (hkl) and  $\epsilon$ (hkl) in Figure 4.1. According to the epsilon ( $\epsilon$ ) phase analysis of the substrate XRD data, the volume fraction of the  $\epsilon$ -(CoCrMo) in the fcc  $\gamma$ -(CoCrMo) matrix changes between  $\sim 26\%$  and  $\sim 38\%$  in substrate samples (D10, D15 and D30). As can be seen from the substrate XRD spectrum, the CoCrMo substrate is mainly composed of fcc  $\gamma$ -(Co,Cr,Mo) phase and a large majority of the fcc grains (the ones parallel to the surface) are in [111] direction.

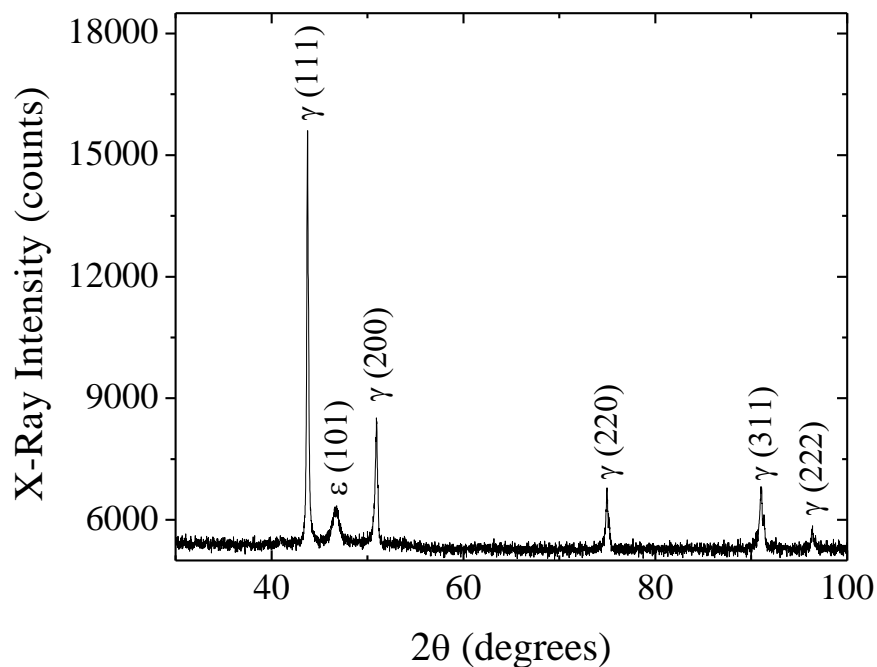


Figure 4. 1. X-ray diffraction spectrum of CoCrMo substrate (D15).

Figure 4.2 comprises the XRD results of the plasma nitrided samples for 1, 2, 4, 6 and 20 hours as well as substrate sample (D15) for comparison. The XRD spectrums of the plasma nitrided and substrate samples are plotted between the angles 35° and 55°. This range allows the observation of the region of the (111) and (200) peaks, which are considered to give more information about plasma nitrided samples compared to the higher (hkl) data range.

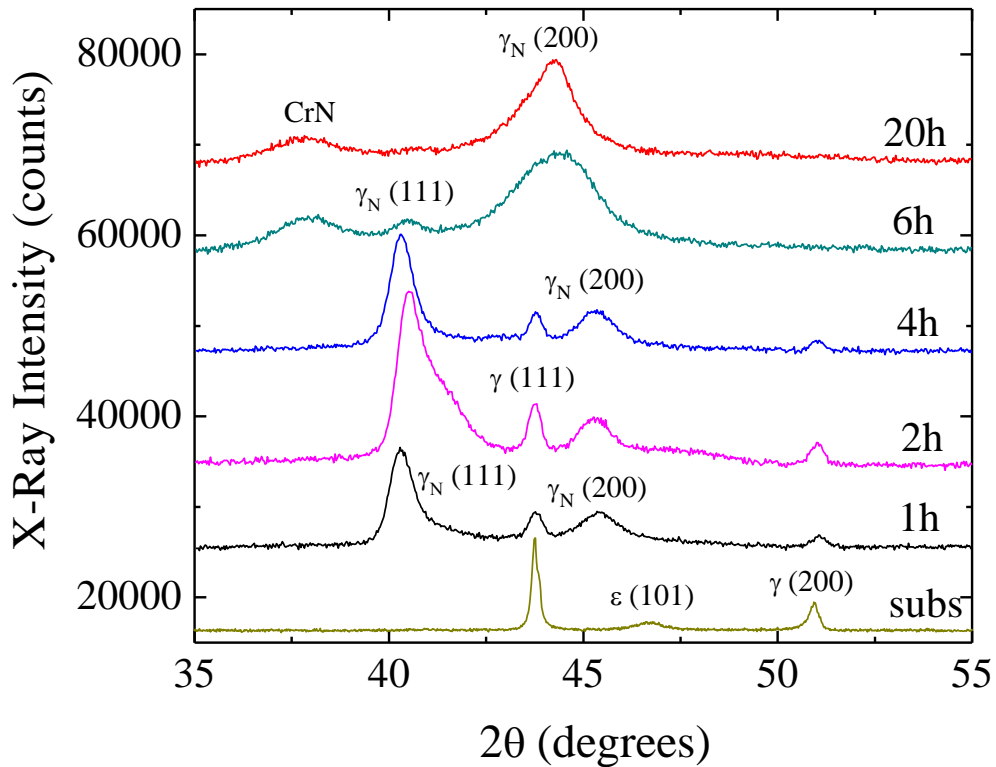


Figure 4. 2. XRD spectrums of substrate and plasma nitrided CoCrMo samples.

The XRD results for the 1, 2, 4, 6 and 20 h plasma nitrided specimens clearly show a new phase,  $\gamma_N$ -(Co,Cr,Mo), which is called expanded austenite phase, solid solution phase or nitrogen in interstitial sites phase (the plasma nitriding induced peaks associated with the various crystallographic planes are labeled as  $\gamma_N$ (hkl) in Figure 4.2). As a result of plasma nitriding, nitrogen atoms enter to the octahedral sites in fcc crystal lattice of CoCrMo samples resulting the expanded fcc crystal lattice. In literature, this phase is observed in fcc austenitic stainless steels (304, 310, 316, 316L) as  $\gamma_N$ -(Fe,Cr,Ni) in many different surface treatment experiments with nitrogen (Baldwin 1998, Ozturk 1995, Öztürk 1994) when the processing temperature is around 400 °C.

Some surface treatment experiments with carbon (C) for austenitic stainless steels and CoCrMo alloys also showed that the expanded austenite phase also forms as  $\gamma_C$ -(Fe,Cr,Ni) or  $\gamma_C$ -(Co,Cr,Mo) after carburizing (Sun 2005, Tsujikawa 2005, Li 2007). Figure 4.3 illustrates a schematic representation of fcc  $\gamma_N$ -(Co,Cr,Mo) phase resulted after the plasma nitriding, which indicated that the nitrogen occupies interstitial sites in the fcc CoCrMo lattice.

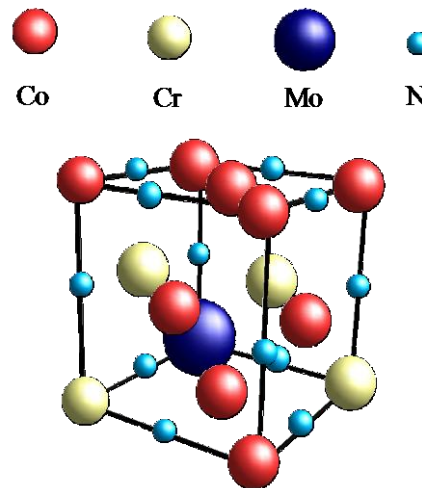


Figure 4. 3.  $\gamma_N$ -(Co,Cr,Mo) crystal structure in plasma nitrided CoCrMo alloy.

Similar to  $\gamma_N$ -(Fe,Cr,Ni) phase in fcc stainless steels (fcc (Fe,Cr,Ni) alloys) in literature (Turkan 2004),  $\gamma_N$ -(Co,Cr,Mo) XRD peaks are shifted to lower  $2\theta$  angles compared to the substrate alloy  $\gamma$ -(Co,Cr,Mo) peaks after plasma nitriding treatment. The main reason for these shifts is due to that nitrogen in fcc lattice creates expansion. Also, the residual stress that the  $\gamma_N$  layer is under is responsible for the shifts. The nitrided peaks ( $2\theta$  peak centers) associated with the shifts and CoCrMo substrate peaks are listed in Table 4.1. As can be seen in Table 4.1, the plasma nitrided  $\gamma_N(200)$  peaks are shifted more than  $\gamma_N(111)$  peaks. The greater shifts of  $\gamma_N(200)$  peaks comparing to the  $\gamma_N(111)$  peaks suggest larger lattice expansions in [200] direction than in [111] direction.

As seen in Figure 4.2, the peaks  $\gamma_N(111)$  and  $\gamma_N(200)$  have not a normal gaussian peak shape for 1, 2 and 4 hour plasma nitrided samples. According to curve-fit results,  $\gamma_N(111)$  and  $\gamma_N(200)$  peaks of 1, 2 and 4 hours nitrided CoCrMo samples consist of more than one peak. This means that nitrogen has not distributed homogenously along the 1, 2 and 4 hours plasma nitrided layers. The nitrogen concentrations change along

the plasma nitrided layer and less and less expanded phases are seen with the increasing depth.

Table 4. 1.  $2\theta$  peak centers of  $\gamma(111)$ ,  $\gamma(200)$ ,  $\gamma_N(111)$  and  $\gamma_N(200)$  of plasma nitrided samples as well as substrate sample obtained after curve-fit analyses.

Nitriding Time (h)	$\gamma(111)$	$\gamma_N(111)$	$\gamma(200)$	$\gamma_N(200)$
0	43.743	-	50.927	-
1	43.801	40.401	51.074	45.506
2	43.756	40.505	51.028	45.269
4	43.795	40.396	51.023	45.313
6	-	40.486	-	44.278
20	-	40.637	-	44.323

One interesting feature in Figure 4.2 is the  $\gamma_N(200)$  peak shape of 6 and 20 hours plasma nitrided samples. As can be noticed, the peaks almost correspond to a gaussian shape while full width of half maximums (FWHM) of  $\gamma_N(200)$  peaks (broad peaks) are relatively higher. The broadness of the peaks are due to that nitrogen concentration changes along the 6 and 20 hours plasma nitrided layers. This induces differently expanded  $\gamma_N(200)$  grains along the layers. According to curve-fit results,  $\gamma_N(200)$  peaks consist more than one charactersitic peak. Also, one explanation for broadness of these  $\gamma_N(200)$  peaks may be because of defects (intergranular cracks) in microstructure of the plasma nitrided layers in [200] direction make  $\gamma_N(200)$  broader.

One key feature in Figure 4.2 obtained from the comparison of the  $\gamma_N(111)$  and  $\gamma_N(200)$  peaks is that  $\gamma_N(111)$  peak is getting smaller in intensities when the nitriding time increases, while  $\gamma_N(200)$  peak is getting dominant with the increasing nitriding time (note 6 and 20 hours XRD spectrums). This behaviour of the  $\gamma_N(111)$  and  $\gamma_N(200)$  peaks can be explained with the rotation of the plasma nitrided grains (texture effect). The results suggest a preferential (200) orientation of  $\gamma_N$  grains parallel to the surface with increasing nitriding times. When the plasma nitriding time increases, plasma nitrided (111) grains rotate in [200] direction due to nitrogen incorporation to the grains. The reason for the grain rotation may also be caused by the compressive stresses in the nitrided layers.

One explanation can be made for the disappearance of the  $\gamma_N(111)$  peak in 6 and 20 hours plasma nitrided samples that may be due to x-ray probe depth, which x-rays can not reach the  $\gamma_N(111)$  planes in nitrided layers. From Figure 4.2 one can say that the



$\gamma_N(200)$  planes (parallel to the surface) are almost dominant on the surface of 6 and 20 hours plasma nitrided CoCrMo samples. In literature, there is no actual data which explains the texture effect on plasma nitrided CoCrMo samples, even FeCrNi stainless steel materials. The texture effect on plasma nitrided layers will be discussed more later.

Another interesting result obtained from Figure 4.2 is that the substrate peaks,  $\gamma(111)$  and  $\gamma(200)$  seems to disappear after 6 hours plasma nitriding. The reason for this can be the increasing nitrided layer thicknesses with increasing nitriding time. Since x-rays do not reach to substrate phase due to the thicker nitrided layers. One can also say for disappearance of  $\gamma(111)$  peak (initially more grains parallel to the substrate surface are in [111] direction) that due to the greater shift of 6 and 20 hours nitrided samples'  $\gamma_N(200)$  peaks,  $\gamma(111)$  substrate peaks may hide in broad  $\gamma_N(200)$  peaks of 6 and 20 hours nitrided samples.

The XRD data in Figure 4.2 clearly shows some structural changes taking place in the CoCrMo samples nitrided for 6 and 20 h, resulting in CrN phase ( $2\theta \sim 37.5^\circ$ ). CrN formed in 6 and 20 h plasma nitrided layers has NaCl crystal structure and its lattice constant is estimated to be 4.1 Å. The clear observation of CrN at 400 °C (for longer plasma durations) of this study is not consistent with earlier studies (Loh 1999, Michler 1998) which show that CrN begins to precipitate when high-chromium steels are nitrided at temperatures above 450 °C. Also, Stinville's study (Stinville 2009) shows no CrN formation in 316L polycrystalline austenitic stainless steel for very long plasma nitriding times at 400 °C. As stated before, CoCrMo has higher Cr (~ 30 at.%) content in its elemental composition compared to FeCrNi alloys (304, 310, 316, etc.) (18-20 at.%). Chemical differences between 316L SS (FeCrNi) and CoCrMo (Cr content in composition) can be the reason for CrN formation in CoCrMo alloy after plasma nitriding at 400 °C for longer times (6 and 20 hours). The reason for CrN formation after plasma nitriding at 400 °C has not been identified in CoCrMo samples yet. There is no evidence in the literature, which shows CrN formation in CoCrMo samples after plasma nitriding at 400 °C. Further investigation on CrN formation will be discussed in next sections (GIXRD Results and Composition Analysis).

According to the XRD spectrums of the plasma nitrided samples in Figure 4.2, the substrate hcp  $\epsilon$ -(CoCrMo) phase is completely disappeared after plasma nitriding, even after one hour plasma nitriding. Not having much clear statements about this situation in literature, during nitriding process, it can be assumed that the substrate  $\epsilon$ -(CoCrMo) phase is converted to the substrate  $\gamma$ -(Co,Cr,Mo) phase, and then the  $\gamma$ -

(Co,Cr,Mo) phase is converted to the  $\gamma_N$ -(Co,Cr,Mo) phase (J. Chen 2008). As can be seen from the SEM images of plasma nitrided sample surfaces, there is no evidence of  $\epsilon$ -(CoCrMo) bands after plasma nitriding. This correlates quite well with the XRD results in Figure 4.2.

Figure 4.4 illustrates Nelson-Riley plot, showing distributions of the  $\gamma_N$  phase lattice constants  $a_N(111)$  and  $a_N(200)$  of the plasma nitrided samples as well as the  $\gamma$  phase lattice constants  $a_0(111)$  and  $a_0(200)$  of the substrate sample (D10) for comparison (the anisotropy in the lattice constants associated with (hkl) reflections can be illustrated by a plot of lattice parameters versus  $\cos^2\theta/\sin\theta$ , known as a Nelson-Riley plot) (Cullity 1956).

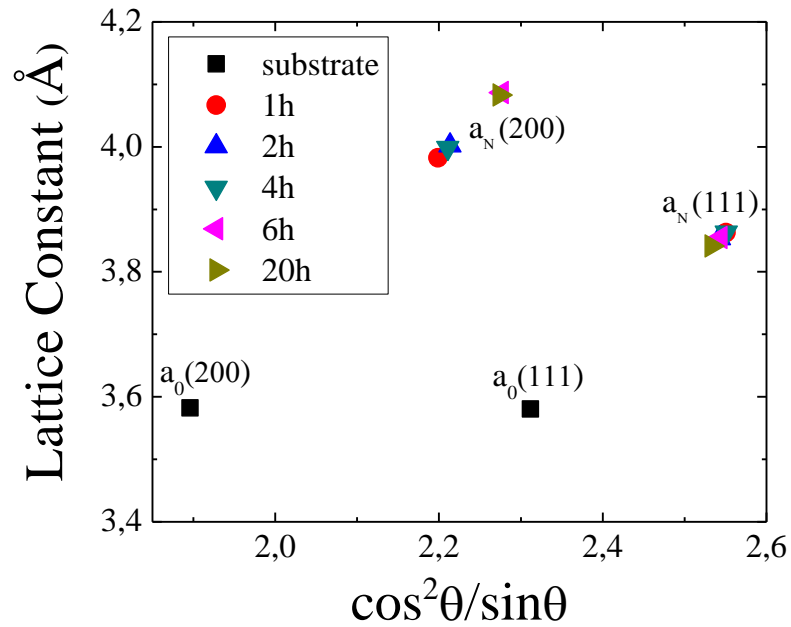


Figure 4. 4. Distribution of (111) and (200) lattice constants of plasma nitrided and substrate CoCrMo samples.

Figure 4.4 reveals some interesting features related to the plasma nitrided CoCrMo samples. Note that there is no difference between plasma nitrided lattice constants  $a_N(111)$  with respect to plasma duration while lattice constants  $a_N(200)$  clearly increased at higher plasma durations (6 and 20 hours). This could be explained by the fact that more nitrogen goes into the (200) oriented grains as a function of the nitriding time. Also, the strong influence of compressive residual stress on the interplanar spacings of different crystallographic planes parallel to the specimen surface may cause

this difference. The data suggest that the influence of the stress on the (200) planes might be higher than on the (111) planes. So, it can be inferred that the fcc lattice expands more in [200] direction than in [111] direction. This anisotropic lattice expansion can be explained in part by elastic constants of individual lattice planes, which show that the elasticity may be different for [111] and [200] directions. Under a uniform compressive stress assumption, the lattice constant  $a_N(200)$  is expected to be larger than lattice constant  $a_N(111)$  because of the elasticity in [200] direction.

Table 4.2 lists the lattice constant values,  $a_{111}$  and  $a_{200}$  for both the substrate and the nitrided specimens, average lattice constant values,  $\langle a \rangle$  in Å, lattice constants expansions,  $\Delta a_{111}/a_{111}$  and  $\Delta a_{200}/a_{200}$  (in %). Also, in this table, nitrogen concentrations of the plasma nitrided (111) and (200) grains,  $C_N(111)$  and  $C_N(200)$ , and average nitrogen concentration values  $C_N$  (in at.%) can be found.

Table 4. 2. Lattice parameters,  $a$ , in Å for the CoCrMo alloy  $\gamma$ -(CoCrMo) phase and the fcc  $\gamma_N$ -(CoCrMo) phase.  $\langle a \rangle$  represents average lattice parameters, while  $\Delta a/a$  refers to the relative difference in lattice parameters. Also, nitrogen concentrations,  $C_N$  in at.% for  $\gamma_N$ -(CoCrMo) and  $\langle C_N \rangle$  represents average nitrogen concentration along the plasma nitrided layers.

Nitriding Time (h)	$a_{111}$ (Å)	$a_{200}$ (Å)	$\langle a \rangle$ (Å)	$\frac{\Delta a_{111}}{a_{111}}$ (%)	$\frac{\Delta a_{200}}{a_{200}}$ (%)	$C_N(111)$ (at.%)	$C_N(200)$ (at.%)	$\langle C_N \rangle$ (at.%)
0	3.579	3.579	3.579	-	-	-	-	-
1	3.863	3.982	3.922	7.92	11.26	35.500	52.000	43.750
2	3.853	4.002	3.928	7.65	11.81	34.250	52.875	43.562
4	3.863	3.998	3.930	7.93	11.70	35.500	52.375	43.938
6	3.855	4.087	3.971	7.70	14.18	34.500	62.750	49.000
20	3.841	4.083	3.962	7.32	14.07	32.250	62.750	47.875

As can be seen from Table 4.2 (also from Figure 4.4), the substitution of nitrogen results in a much larger lattice constants in comparison to that of substrate. As can be seen in the table, the main reason this is due that the nitrogen concentration of (200) oriented planes are higher than the concentration of the (111) oriented ones. The nitrogen concentration difference between the (111) and (200) planes even reaches two times. Note that, for the 20 h nitrided specimen, the nitrogen concentration of (200) planes is  $\sim 52 - 63\%$ , while the concentration is  $\sim 35\%$  for (111) planes. Also, lattice expansion shows an anisotropic behaviour during plasma nitriding because of the elastic properties of different lattice directions, which can be seen in Table 4.2 that lattice

constant expansions  $\Delta a_{200}/a_{200}$  are higher than lattice constant expansions  $\Delta a_{111}/a_{111}$ , moreover, at higher nitriding times (6 and 20 hours), difference between the expansions of  $\Delta a_{111}/a_{111}$  and  $\Delta a_{200}/a_{200}$  reach two fold; ( $a_{111} < a_{200}$ ). In a previous study with nitrogen implanted 304 austenitic steels at moderate temperatures (350 °C – 450 °C) (O. Ozturk 1995), the same anisotropic expansion in different oriented lattice constants is observed.

One can notice in Table 4.2 that there is a very good correlation between the lattice constant calculations and nitrogen concentration calculations, both of which based on XRD experimental data. The nitrogen concentration of (111) grains are almost constant regardless of plasma nitriding time, which means that however long the plasma nitriding time there is always same amount of nitrogen in (111) planes. This result correlates well with that lattice expansion in [111] direction is also constant regardless of plasma nitriding time.

Also one interesting result obtained from Table 4.2 is that while the nitrogen concentration of (111) grains are almost constant with respect to plasma nitriding time, the nitrogen concentrations of (200) grains show an increasing manner. At higher nitriding times (6 and 20 hours), the nitrogen concentration of (200) grains reaches two-fold of the nitrogen concentration of (111) grains. As a consequence of the anisotropy in the lattice constants of the  $\gamma_N$  layer (stated before), the predicted nitrogen concentration values for the nitrided later may become orientation dependent, being larger for the (200) crystallographic planes.

In addition to this, as a result of macroscopic stresses, the nitrogen concentration values can be higher than the real values (it should be kept in mind that these values are relied on semi-quantitative approaches). In the literature, the general conclusion about nitrogen concentration is that the nitrogen concentration reaches the maximum values of 30 at.% after nitriding as it can be seen in the composition analysis part of this study (~ 32 at.%) as well. Also, the reason for the higher nitrogen concentration obtained from semi-quantitative XRD results might be due to Vegard's constant used in calculations, which is not for  $\gamma$ -(CoCrMo). The validation of the equation which is used for calculation of the nitrogen concentration is still controversial for higher nitrogen concentrations (> 10 at.% N).

Table 4.3 lists the  $\gamma_N$  layer thicknesses for the nitrided samples (1, 2 and 4 h) based on the (111) and (200) oriented grains. The thicknesses of (111) and (200) oriented layers nitrided for 1, 2 and 4 hours and their average thicknesses depending on

two different linear mass absorption coefficients found in the data analysis chapter, in one of which nitrogen is taken to be in the octahedral sites in the fcc CoCrMo lattice, while, in the other, nitrogen is not taken into account for calculations. The thicknesses of 6 and 20 hours plasma nitrided CoCrMo samples can not be calculated because no detection of substrate peaks is observed in their XRD spectrums.

Table 4. 3. The estimated  $\gamma_N$  layer thicknesses based on (111) and (200) oriented grains and their average values.

Nitriding Time	$\mu= 2530$ $\text{cm}^{-1}$		$\mu[\text{N}]=2129$ $\text{cm}^{-1}$		$\langle L_{\mu} \rangle$ ( $\mu\text{m}$ )	$\langle L_{\mu[\text{N}]} \rangle$ ( $\mu\text{m}$ )
	$L_{111}$ ( $\mu\text{m}$ )	$L_{200}$ ( $\mu\text{m}$ )	$L_{111}$ ( $\mu\text{m}$ )	$L_{200}$ ( $\mu\text{m}$ )		
1h	2.13	2.52	2.53	3.00	2.33	2.76
2h	2.93	3.39	3.48	4.03	3.20	3.71
4h	2.13	3.54	2.53	4.21	2.33	3.88

As seen in Table 4.3,  $L_{200}$  thicknesses are always larger than  $L_{111}$  thicknesses for 1, 2 and 4 h plasma nitrided CoCrMo samples. The relative intensity analyses of  $\gamma_N$  and  $\gamma$  reflections of (111) and (200) orientations indicate that the total  $\gamma_N$  layer thickness for grains with (200) orientation is greater than (111) ones. These results clearly represent that nitrogen diffuses deeper in the direction associated with the (200) oriented grains. This can be explained like that, when the plasma nitriding starts, the nitrogen diffuses in (200) grains easier and (200) grains behave as a preferential grain for nitrogen. This indicates that (200) grains present faster diffusion paths for nitrogen. In a study (Öztürk 1994), step-wise sputtering was carried out on nitrogen implanted 304 ASS. In this experiment, complete disappearance of  $\gamma_N$  (111) peak was observed after 9<sup>th</sup> sputter step, while the  $\gamma_N$  (200) peak was still present in x-ray diffraction patterns. This results clearly provides the strong evidence of deeper nitrogen diffusion in the (200) oriented grains and explains the thicker nitrided layers associated with the (200) orientations. More experimental evidences will be presented in next chapters, cross-sectional SEM analysis of nitrided layers, which shows significant variations in layer thickness along the nitrided layers.

One can find the XRD analysis calculated  $\gamma_N$  thicknesses of 1, 2 and 4 hours plasma nitrided layers as controversial because of the decreasing manner of the plasma

nitrided layer with respect to increasing nitriding time. But it should be considered that the thickness calculations in this section come from XRD experimental data and semi-quantitative approaches, so, these thicknesses may not be reliable than the thicknesses which are obtained from other experiments (GDOES, SEM, AFM), that are discussed in next sections.

## 4.2. GIXRD Results

The GIXRD results at the grazing incidence angle  $\omega=1^\circ$  for the 1, 2, 4, 6 and 20 hours plasma nitrided samples are shown in Figure 4.5. At this grazing angle, penetration depth of x-rays is calculated as  $\sim 82 \text{ nm}$  ( $x \sim \sin\omega/\mu[\text{N}]$ ) (the linear mass absorption coefficient used in x-ray penetration depth calculation is calculated according to the model which nitrogen occupies the octahedral sites in fcc lattice). One of the key results observed from Figure 4.5 is that the intensities of  $\gamma_{\text{N}}(200)$  peaks increase with respect to the nitriding time while the intensities of  $\gamma_{\text{N}}(111)$  peaks decrease with respect to the nitriding time. It is believed that even the thicknesses of overall plasma nitrided layer increase, the thicknesses of layers associated with  $\gamma_{\text{N}}(200)$  and  $\gamma_{\text{N}}(111)$  grains has different extension manners with respect to plasma nitriding time. This correlates quite well with the semi-quantitative  $\theta$ - $2\theta$  XRD results of plasma nitrided samples. As can be noticed above,  $\gamma_{\text{N}}(200)$  and  $\gamma_{\text{N}}(111)$  have different lattice constants, nitrogen concentrations and, as a result, different layer thicknesses.

Note that, in Figure 4.5,  $\gamma_{\text{N}}(200)$  peak is highly dominant on the 6 and 20 hours plasma nitrided surfaces. This can be explained by the help of grain rotation (texture effect); as the plasma nitriding time increase, the plasma nitrided grains start to rotate in the [200] direction and the grain rotation reaches its maximum value at 20 hours plasma nitriding surface (compare the peak areas of  $\gamma_{\text{N}}(200)$  and  $\gamma_{\text{N}}(111)$  peaks of 6 and 20 hours nitrided samples). Being related to the N concentrations, the grain rotations in the nitrided layers form high compressive stresses resulting in defective structures along the plasma nitrided layers (as can be seen in cross-sectional characterization section, 6 and 20 hours plasma nitrided layers have cracks along the nitrided layers).

One of the other features obtained from Figure 4.5 is the clear formation of CrN in 6 and 20 h plasma nitrided samples. As can be seen in Figure 4.5, there is no CrN formation in 1, 2 and 4 h plasma nitrided samples. This result also correlates well with

the  $\theta$ - $2\theta$  XRD results of plasma nitrided samples discussed above. In order to gain more knowledge about CrN formation in CoCrMo samples nitrided at 400 °C, the GIXRD spectrums of 6 and 20 h plasma nitrided samples are taken at different grazing angles;  $\omega = 0.5^\circ, 1^\circ, 2^\circ, 2.5^\circ, 3^\circ, 4^\circ, 5^\circ, 10^\circ$ .

Figure 4.6 shows the GIXRD spectrums of 20 h plasma nitrided CoCrMo taken at various grazing angles ( $\omega = 0.5^\circ, 1^\circ, 2^\circ, 2.5^\circ, 3^\circ, 4^\circ, 5^\circ, 10^\circ$ ); x-rays penetration depth in the 20 hours plasma nitrided layer changes between 41 and 816 nm ( $\sin\omega/\mu[N]$ ) for the grazing angle range (from 0.5 to 10). The most important result obtained from Figure 4.6 is that CrN (probably in precipitate form) are distributed homogeneously in 20 h plasma nitrided  $\gamma_N$  layer. Homogeneous CrN distribution can be explained by the observation that proportion of the integrated peak areas of CrN and  $\gamma_N(200)$  peaks of 20 h plasma nitrided sample do not change with respect to increasing grazing angle of x-rays. If CrN is distributed on the top of the treated layer, it should be seen that the integrated areas of CrN peaks get smaller with the increasing grazing angles. There is no actual data in literature that explains this homogeneous distribution of CrN phase in plasma nitrided CoCrMo and austenitic stainless steels (ASS). The effect of CrN formation in treated layers on mechanical properties of 6 and 20 h plasma nitrided layers will be discussed next chapters.

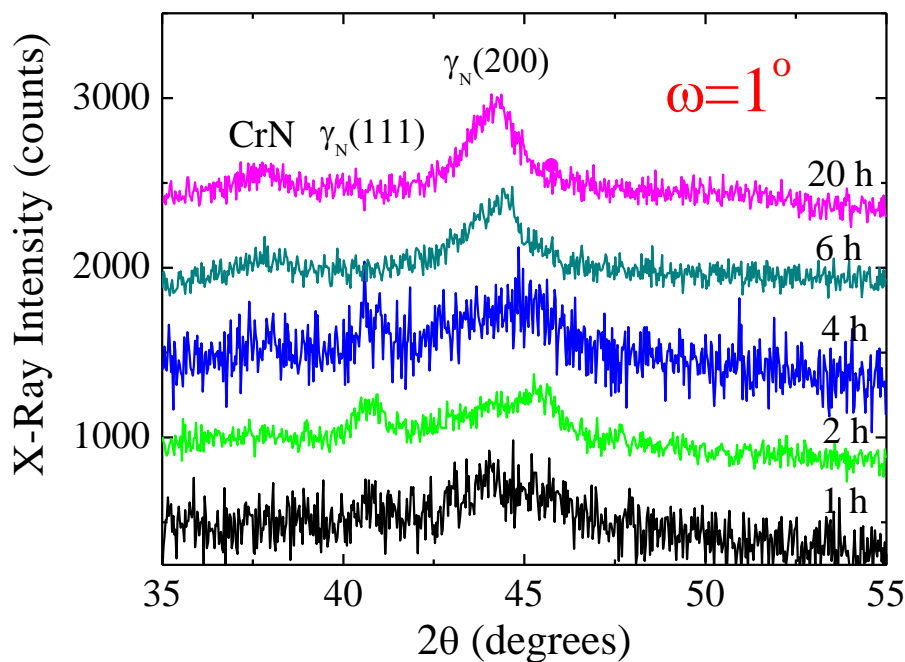


Figure 4. 5. GIXRD spectrums ( $\omega = 1^\circ$ ) of 1, 2, 4, 6 and 20 h plasma nitrided samples.

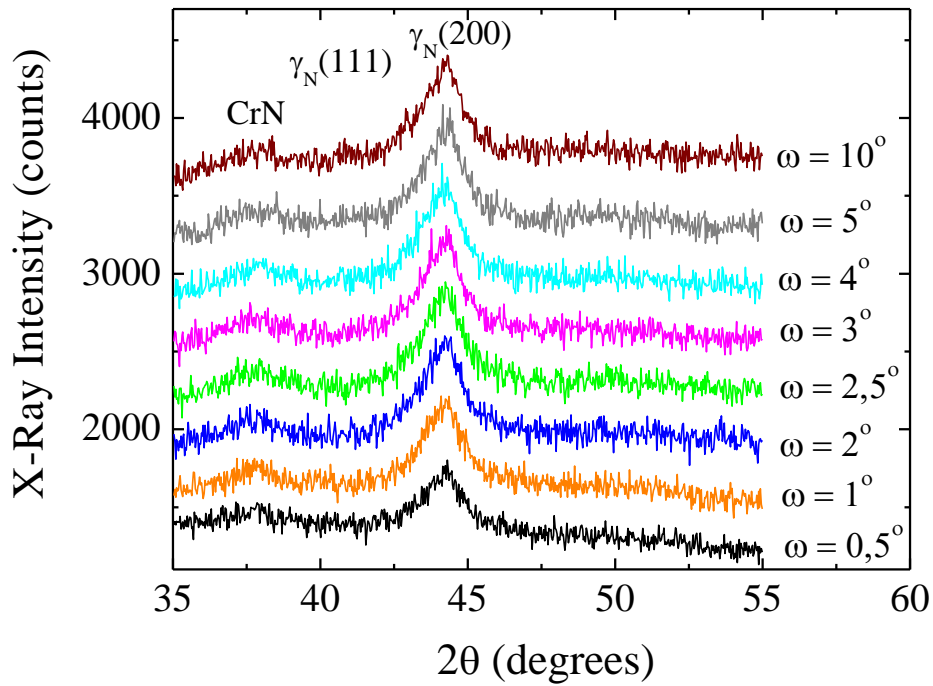


Figure 4. 6. GIXRD spectrum of 20 h plasma nitrided CoCrMo at various grazing angles;  $\omega = 0.5^\circ, 1^\circ, 2^\circ, 2.5^\circ, 3^\circ, 4^\circ, 5^\circ, 10^\circ$ .

Another interesting feature in Figure 4.6 is that  $\gamma_N(111)$  peak does not appear up to the grazing angle  $10^\circ$ . This is closely related to the x-ray penetration depth. The x-ray penetration depth at the grazing angle  $10^\circ$  for the 20 hours plasma nitrided layer is 816 nm. The GIXRD data clearly show that, on the very surface (maximum 816 nm) of the 20 h plasma nitrided specimen, all the (111) nitrided grains almost rotated to the [200] direction. From this result, there may be a correlation between the grain rotation (or texturing) and the nitrogen concentration through the nitrided layer.



## CHAPTER 5

### TOPOGRAPHICAL CHARACTERIZATION

The surface topographies of as-polished and plasma nitrided CoCrMo surfaces are investigated by using SEM, AFM, optic microscope and surface profilometer (Talysurf CCI Optical Interferometry). The aim of the experiments is to characterize the plasma nitrided surfaces as well as to observe the structural changes on plasma nitrided surfaces. In addition to these, the average ( $R_a$ ) and RMS (root-mean-square) roughnesses of the as-polished and plasma nitrided CoCrMo surfaces are investigated by AFM (for small areas,  $35\ \mu\text{m} \times 35\ \mu\text{m}$ ) and optical surface profilometer (scan areas  $\sim 350\ \mu\text{m} \times 350\ \mu\text{m}$ ).

#### 5.1. CoCrMo Substrate Surfaces

Before plasma nitriding, all CoCrMo samples (D10, D15 and D30) were polished to mirror like quality. After polishing, CoCrMo substrate surfaces (D10) are etched by using two different etching techniques,  $\text{Ar}^+$  beam etching and electrochemical etching (see experimental section), in order to investigate the CoCrMo substrate surface structures. After plasma nitriding of CoCrMo samples, SEM, AFM and surface profilometer measurements were performed in order to investigate the surface morphologies of all plasma nitrided CoCrMo specimens.

Figure 5.1 shows CoCrMo substrate surface (D10) after Ar beam etching (above) and electrochemical etching (below) under two different magnifications (2000X and 5000X). As can be seen from these pictures, the CoCrMo substrate surface is smoothly revealed by Ar beam etching compared to the electrochemical etching. The photos clearly show the grain structures of the substrate phases ( $\gamma$ -(CoCrMo) +  $\epsilon$ -(CoCrMo)). In the photos in Figure 5.1, the  $\epsilon$ -(CoCrMo) phase can be seen as thin bands in  $\gamma$ -(CoCrMo) matrix. One feature obtained from Figure 5.1 is that the substrate material does not have an homogenous grain structure on the surface, grain size and shape change through the surface. The grain sizes for CoCrMo samples of this study, measured in an earlier study, change from  $5\ \mu\text{m}$  to  $15\ \mu\text{m}$  (O. Öztürk 2006).

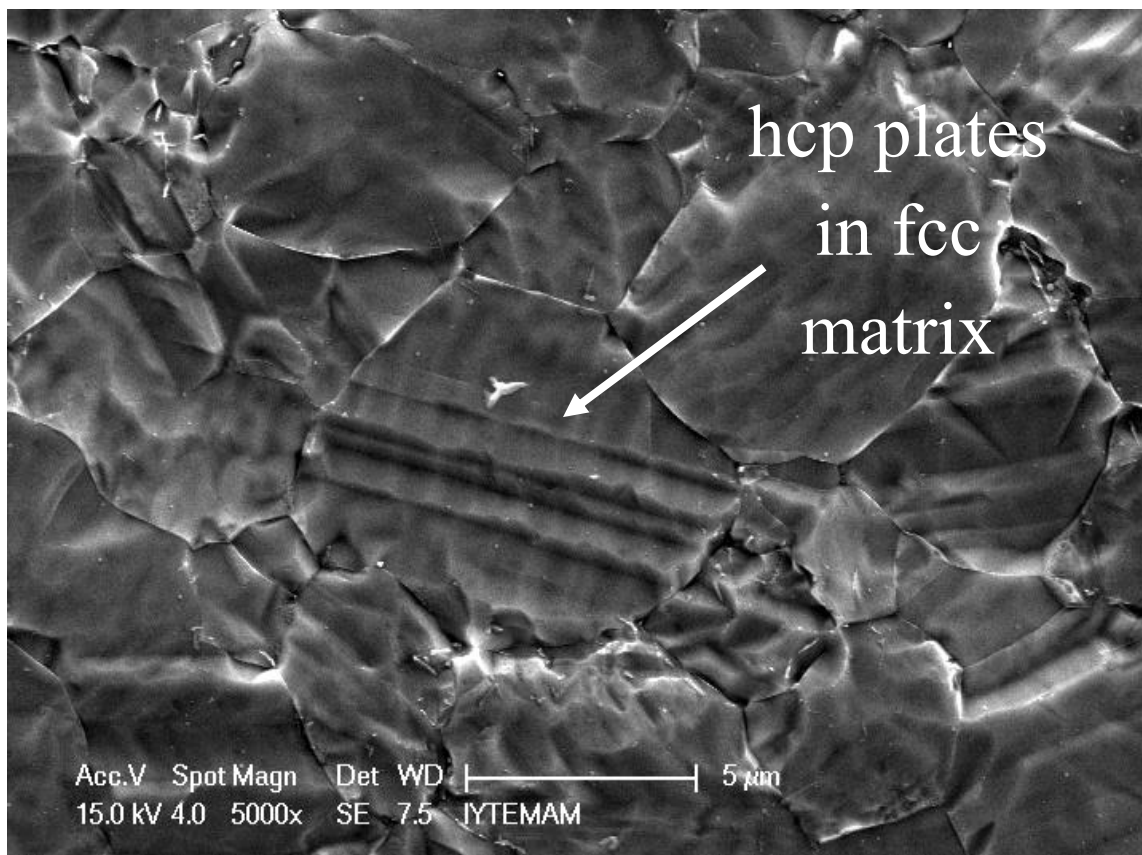
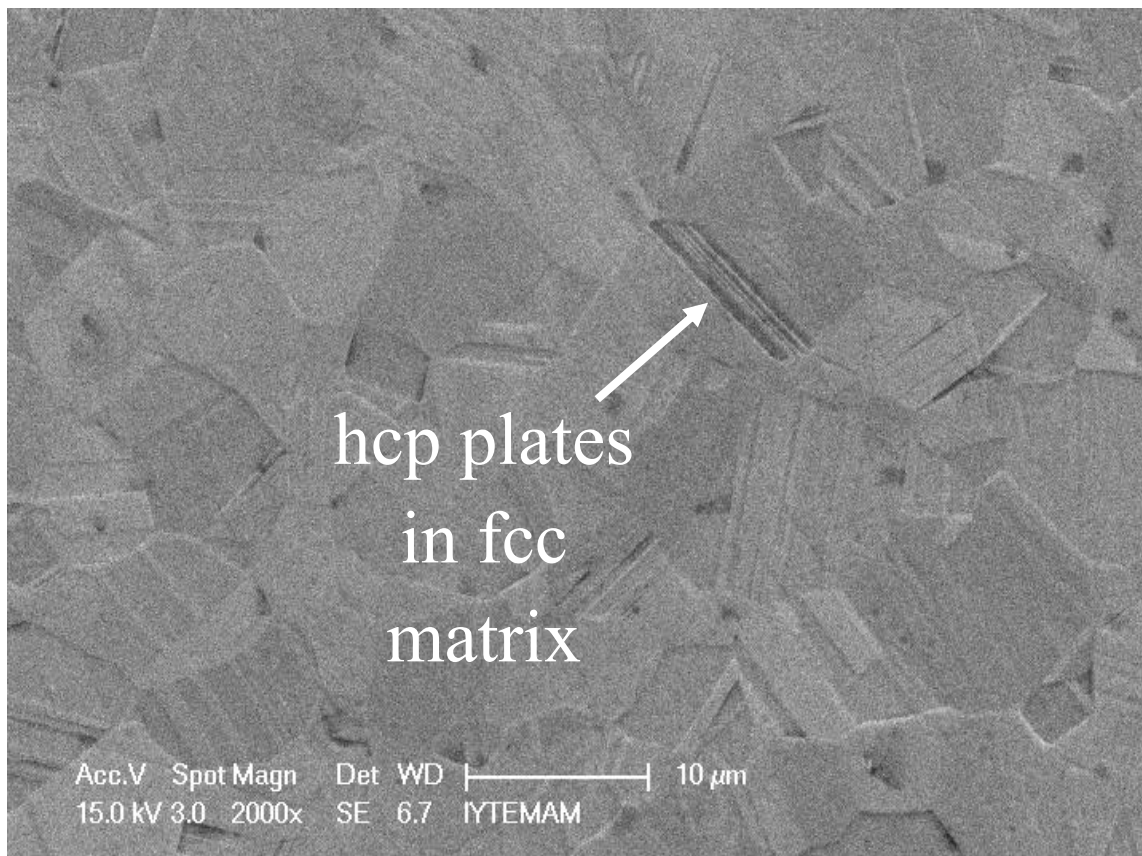


Figure 5. 1. SEM images of CoCrMo substrate surface (D10) after Ar beam etching (above) and electrochemical etching (below).

## 5.2. Plasma Nitrided Surfaces

Figure 5.2 represents optical interferometry results of as-polished CoCrMo substrate (D15), and 6 and 20 h plasma nitrided CoCrMo surfaces. It can be seen from Figure 5.2 that there are some small dots on the surface of the as-polished sample, and these are probably due to the diamond powder used in polishing of the samples. As can be seen from Figure 5.2, there is clear evidence that the nitrided surfaces are rougher than the as-polished substrate surface.

The average roughness ( $R_a$ ) and root mean square roughness ( $R_q$ ) of the substrate surface are 3.62 nm and 4.79 nm, respectively based on the AFM roughness analyses. The average roughness gives the deviation in surface heights, while the RMS roughness represents the standard deviation of the surface heights. So, it is expected that the RMS roughness is higher than the average roughness. Equation 5.1 represents the average roughness ( $R_a$ ) and Equation 5.2 represents the RMS roughness ( $R_q$ ).

$$R_a = \frac{1}{n} \sum_{i=1}^n |y_i| \quad (5.1)$$

$$R_q = \sqrt{\frac{1}{n} \sum_{i=1}^n y_i^2} \quad (5.2)$$

where  $R_a$  and  $R_q$  are average and RMS roughnesses, respectively.  $y_i$  is the height of the  $i^{\text{th}}$  scan, and  $n$  is the number of the scans.

Figure 5.3 and Figure 5.4 represent the 2-D and 3-D AFM graphs of the surface of the plasma nitrided surfaces with the scan area of  $35\mu\text{m} \times 35\mu\text{m}$  (The scan area was chosen as large as possible). There is no clear evidence about grain shapes and grain sizes in the AFM pictures. The grain boundaries could not be obtained from AFM micrographs. This is because AFM scans the height differences along the sample.

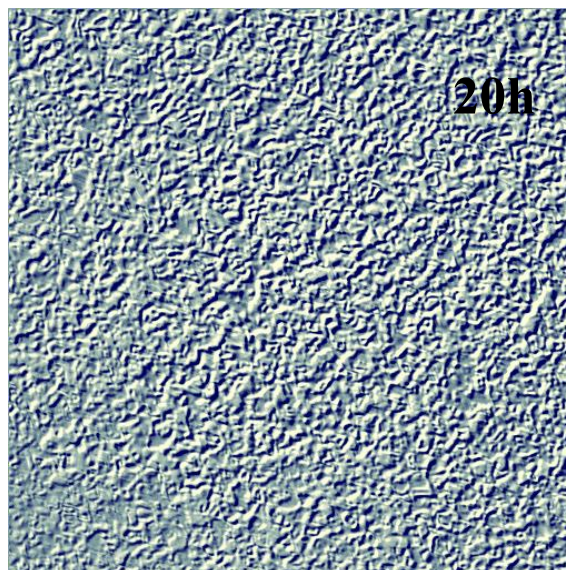
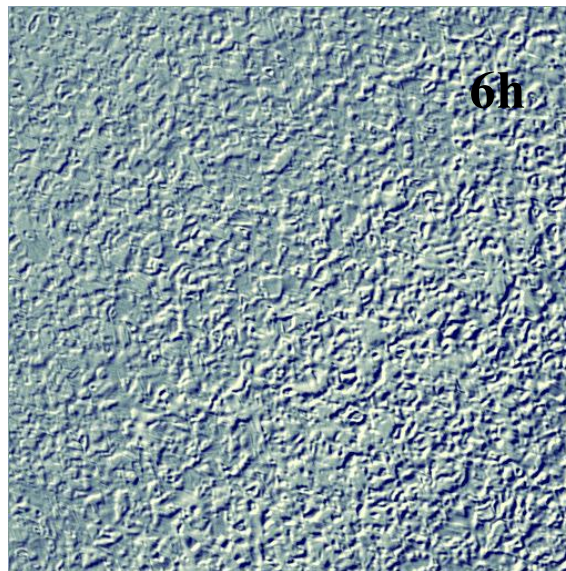
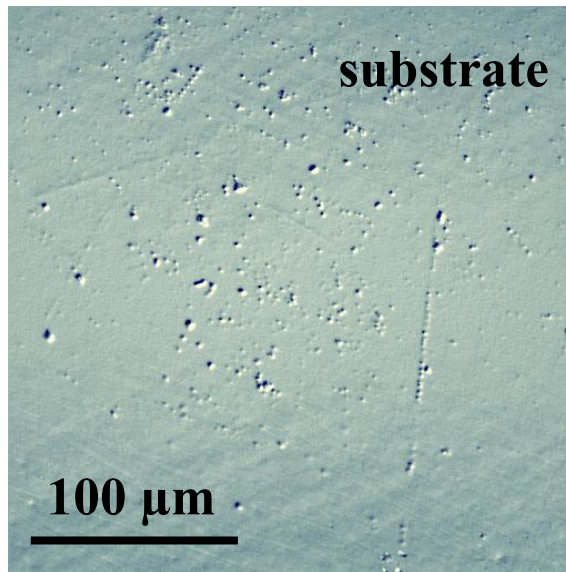


Figure 5. 2. The optical interferometry images of the plasma nitrided as well as the substrate CoCrMo surfaces.

As can be seen from these AFM figures, the surface is quite rough due to mainly different expansion rates of differently oriented grains (discussed in much more detail in the XRD results section) and possibly due to the compressive stresses. During the plasma nitriding, an outward nitrogen diffusion develops (swelling), although, inward nitrogen diffusion into the CoCrMo sample is more dominant. The swelling effect (the outward lattice expansion) is explained in much more detail in the XRD results section. The roughness values were obtained from the analysis of the AFM images in Figure 5.3 and Figure 5.4. At least, 3 scans were made for each surface to estimate the roughnesses of the surfaces.

Table 5.1 lists the average and RMS roughnesses of plasma nitrided as well as as-polished CoCrMo surfaces. As can be seen from this table, roughness values of plasma nitrided CoCrMo surfaces increase with respect to plasma nitriding time. Compared to the as-polished CoCrMo surface, the average roughnesses of plasma nitrided samples increased about 15 times with increasing nitriding time. The roughness of the as-polished surface is 3.6 nm, while the roughness of the nitrided surface reaches 60 nm for the surface of the 20 h nitrided sample.

Table 5. 1. Average and RMS roughness values of as-polished and plasma nitrided CoCrMo surfaces based on the AFM measurements.

Nitriding Time (h)	R <sub>a</sub> (nm)	R <sub>q</sub> (nm)
as-polished	3,6	4,8
1h	29,4	39,1
2h	30,0	39,0
4h	45,6	58,4
6h	46,2	59,6
20h	60,1	76,8

As can be seen from Figure 5.3 and Figure 5.4, there is no homogeneous structure on the plasma nitrided CoCrMo surfaces. It can be said that the different grains may have different roughness values depending on that different grains have different lattice expansions (implying different N contents). According to the XRD results, the nitrogen concentration of (200) oriented grains is two times higher than the nitrogen concentration of (111) oriented grains. Therefore, the reason for unhomogeneity of the

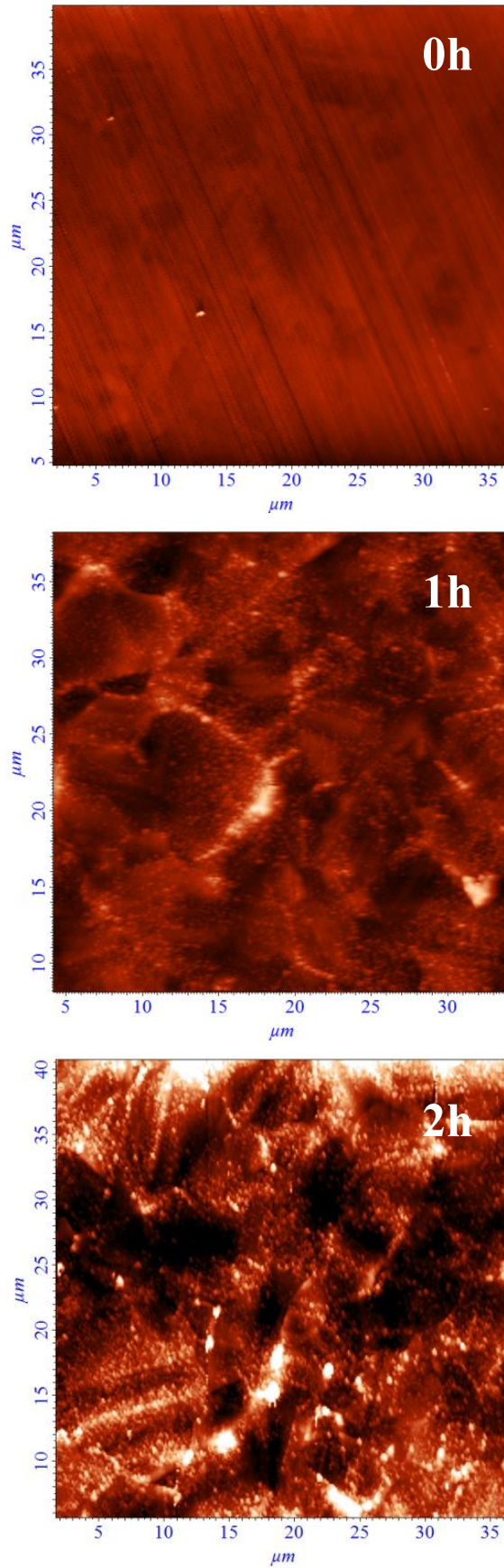


Figure 5. 3. 2-D AFM images of the plasma nitrided surfaces. AFM image of the substrate (0h) is also included.

**(cont. on next page)**

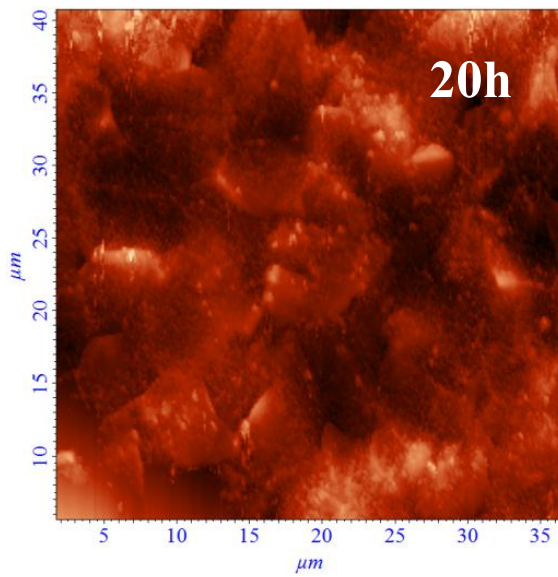
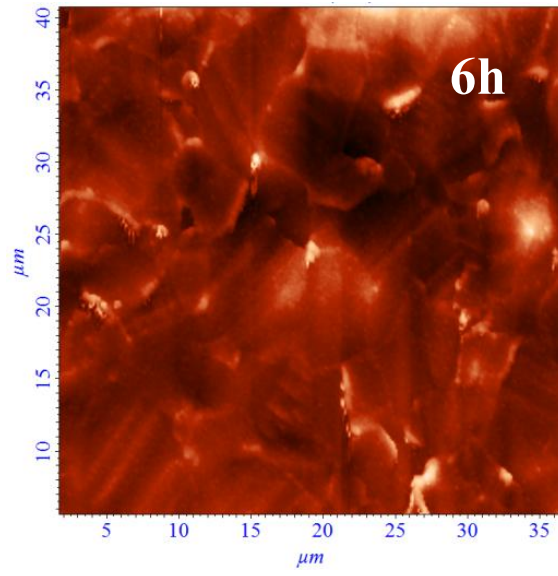
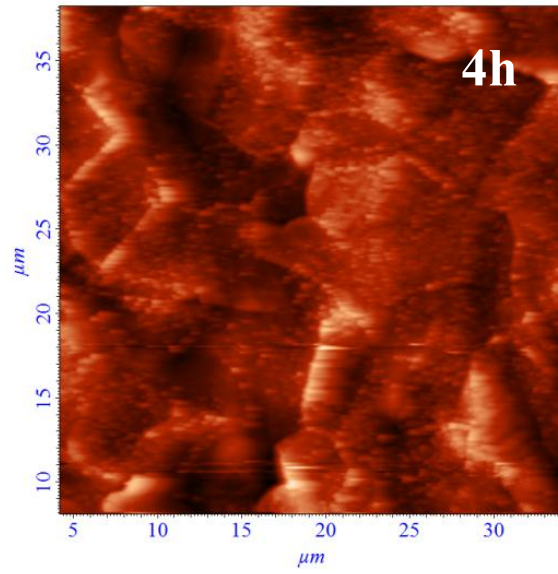


Figure 5.3 (cont.)

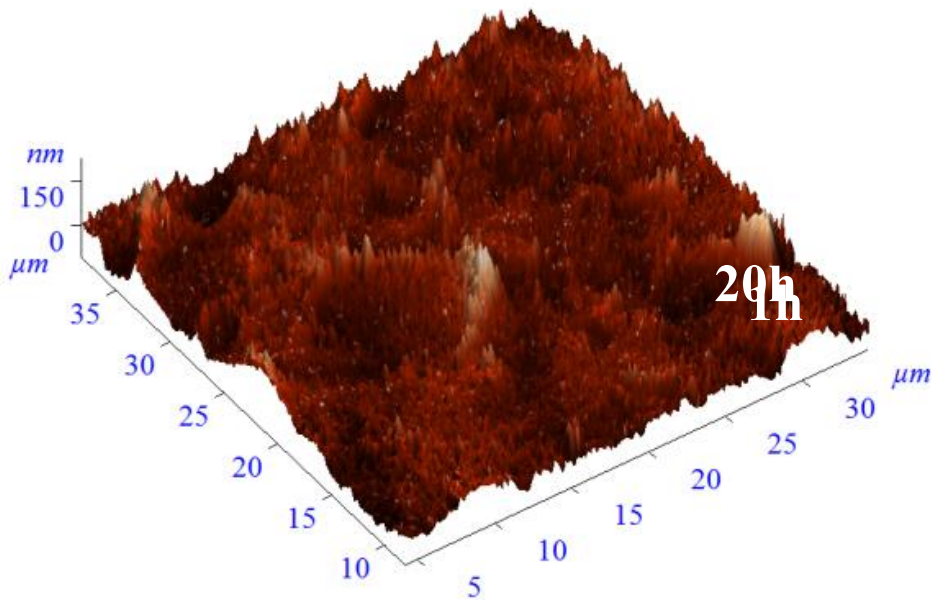
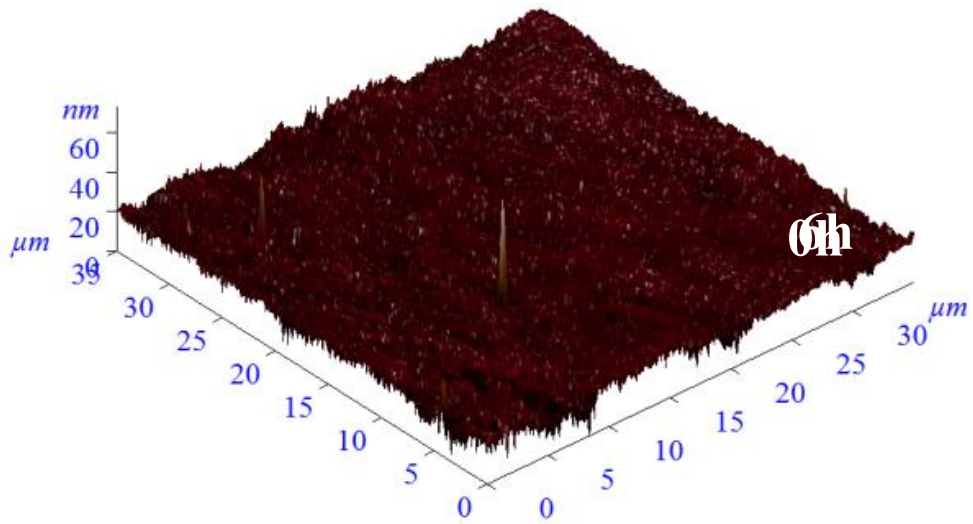


Figure 5. 4. 3-D AFM images of the plasma nitrided surfaces. AFM image of the substrate (0h) is also included.

(cont. on next page)



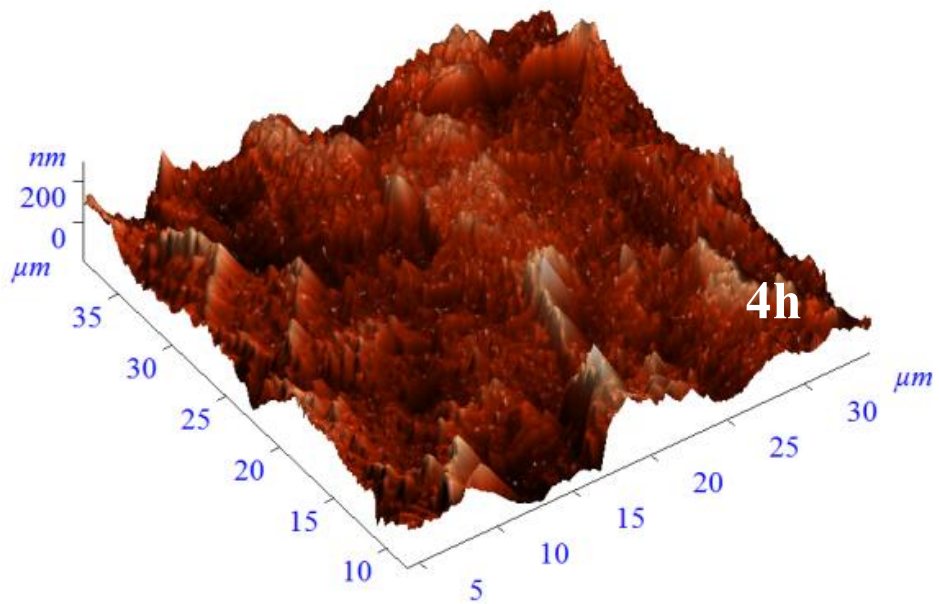
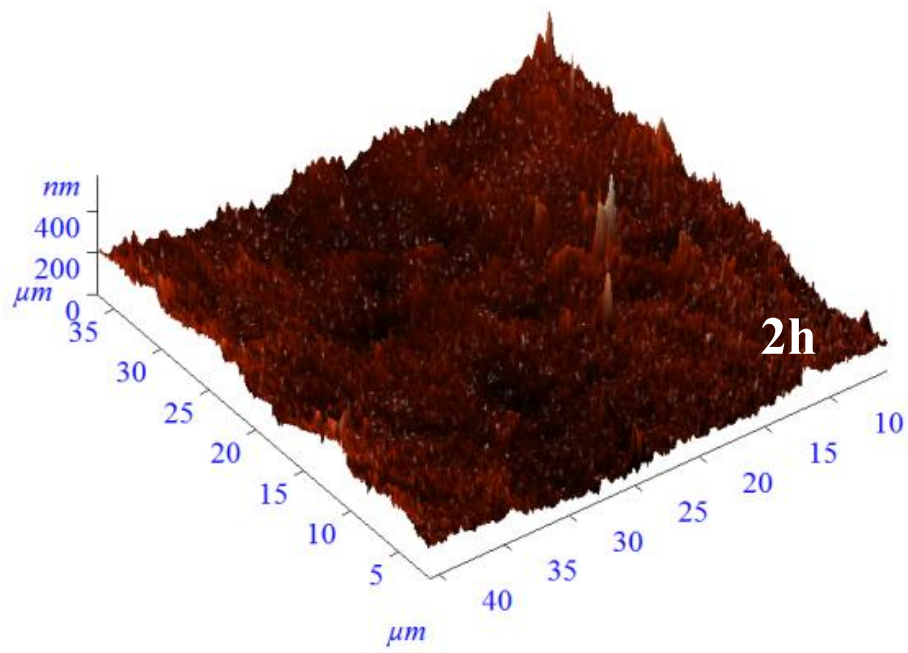


Figure 5.4. (cont.)

(cont. on next page)

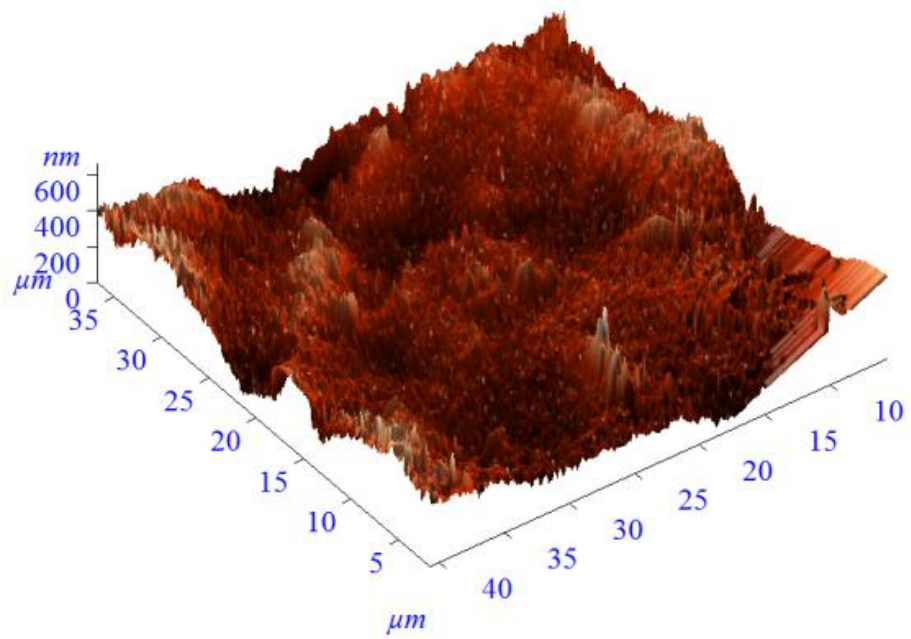
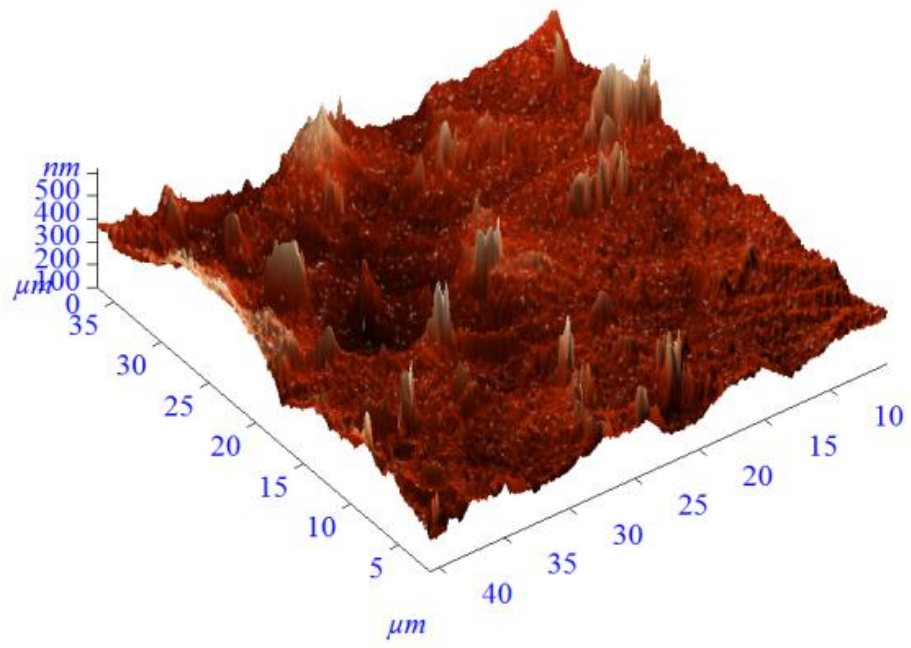


Figure 5.4. (cont.)

surfaces may be due to different nitrogen concentration of the grains as well as their different lattice expansions (both into the sample and outwards). Also, the compressive stresses that the nitrided layers are under may contribute to the increased surface roughness of the plasma nitrided samples.

Figure 5.5 shows the SEM micrographs of the 2 and 20 h plasma nitrided surfaces. Comparing the CoCrMo substrate SEM micrographs (Figure 5.1) and the nitrided SEM micrographs (Figure 5.5), there is a clear observation that the substrate grains are much more distinct than the nitrided grains in Figure 5.5. It can be presumably said that some regions in Figure 5.5 are the plasma nitrided grains which have similar grain shapes and sizes with the CoCrMo substrate material.

As can be seen from Figure 5.5, there are white spots on the surfaces of 2 h and 20 h plasma nitrided. These white spots are observed on the surfaces of all plasma nitrided samples. It is believed that the white spots are not related to either the CoCrMo substrate itself or the plasma nitriding of the CoCrMo samples. It can be assumed that the white spots formations on the nitrided surfaces due to contaminations in the plasma nitriding chamber (quartz tube). If the white spots were due to either CoCrMo substrate or the nitriding process, it should be expected that the white spots should have showed a time depended behaviour. For example, the white spots should have increased with respect to time being more on the 20 h plasma nitrided surface, but there is no correlation between the white spots and the nitriding time. White spots are the most on the 2 h nitrided surface based on the SEM micrographs. One weak possibility for the white spot formation can be that those white spots may be some oxides of Co, Cr or Mo elements, although, EDX results do not give a proper explanation about Co, Cr or Mo oxides. Also, in order to identify the white spots, careful GDOES characterizations were done on the plasma nitrided samples. But no clear observation has been found for these formations because GDOES has not enough depth sensitivity (it is believed that white spots on the top 5 or 10 nm of the plasma nitrided surfaces). The reasons of the white spot formation are still not identified. In order to identify the white spots, further experimentation needs to be performed by x-ray photoelectron spectroscopy (XPS) because it has a unique depth sensitivity and it also gives bonding information.

Also, as can be seen fom Figure 5.5, structural defects (intergranular cracks) occur on plasma nitrided surfaces due to the nitriding treatment. This observation correlates quite well with the discussion made in the XRD results section. The reason for the structural defects is mainly high compressive stresses in ntrided layers. These

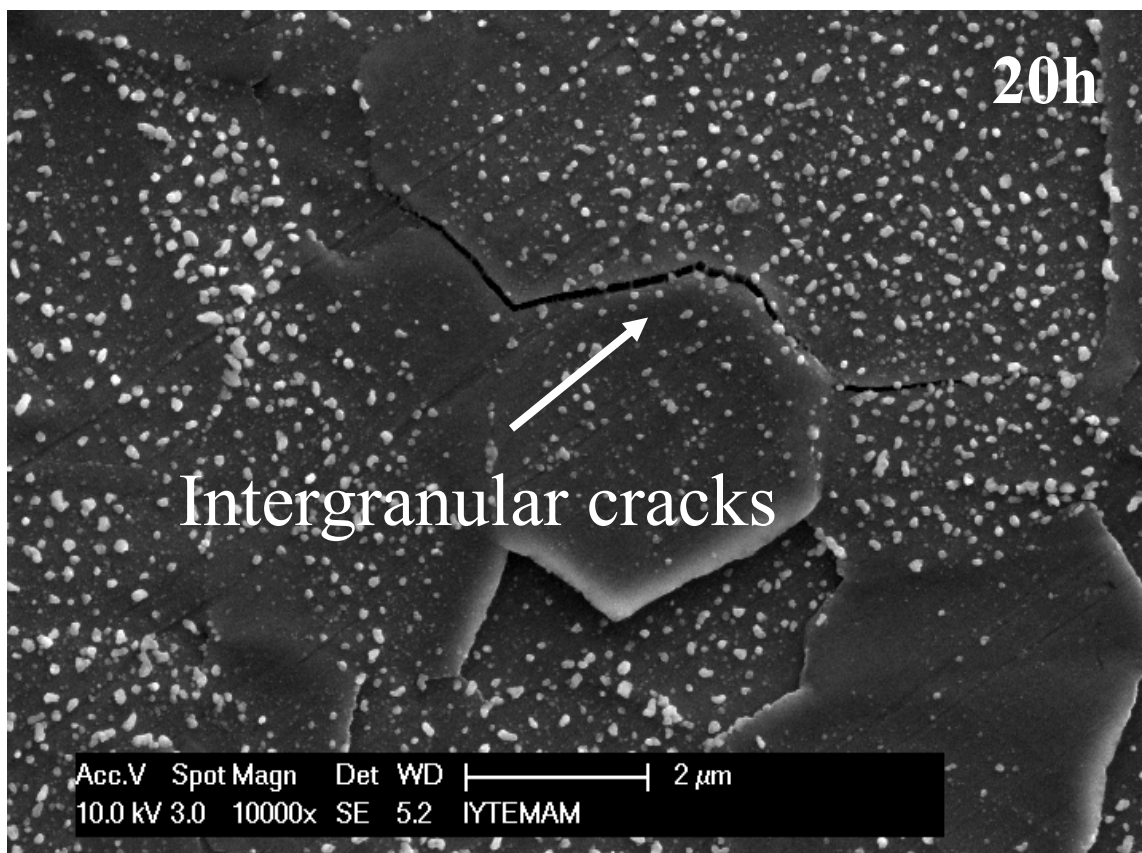
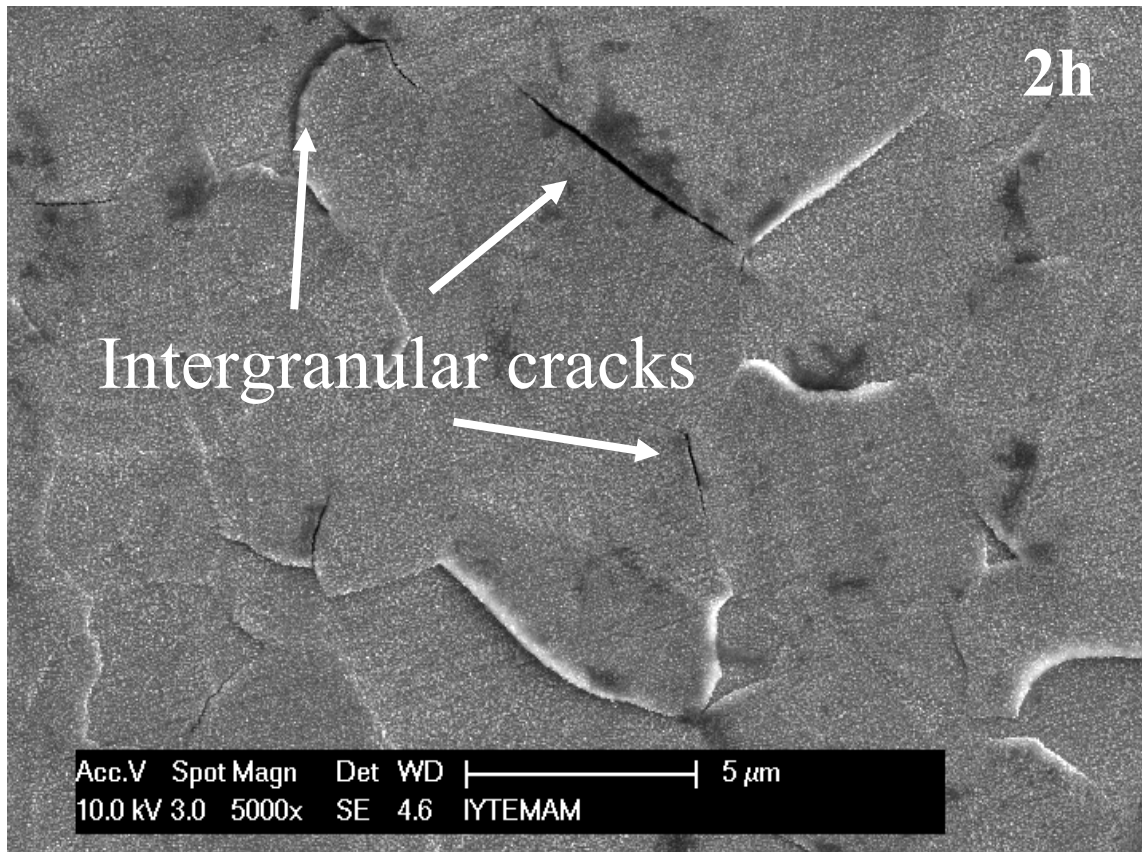


Figure 5. 5. SEM pictures of 2 h (above) and 20 hours (below) plasma nitrided CoCrMo surfaces.

kind of defects have been reported in an earlier study (Stinville 2009) of a plasma nitrated 316L austenitic stainless steel at 400 °C. This study found out that after very long nitriding times (160 h) there was the loss of grains on the nitrated surface due to high compressive stresses.

As can be seen from the photomicrographs of the nitrated CoCrMo samples (SEM, AFM and interferometry results), the surfaces became rougher compared to the substrate surface and gained an uneven property. One explanation is that different lattice expansions (both into the sample and outwards) and different N contents for differently oriented planes have an effect on the surface property of the nitrated samples. Also, compressive stresses and grain rotation (texture development) in the [200] crystallographic direction contribute the defects in the nitrated phase. According to the optical interferometry as well as the AFM pictures, the plasma nitrated surfaces are rougher than the as-polished (before nitriding) CoCrMo surfaces and the roughness of the surfaces clearly depend on the nitriding time (rougher surfaces for longer nitriding times). This is due to that when the plasma nitriding time increases the role of nitrogen on the grain rotation due to the different lattice expansions (related to the different nitrogen content in differently oriented grains and high compressive stresses) and defects increases.

## CHAPTER 6

### CROSS-SECTIONAL MICROSCOPY CHARACTERIZATION

Cross-sectional microscopy analysis of the plasma nitrided CoCrMo specimens were done after polishing, electrochemical etching and Ar beam etching. The cross-sectional sample preparation is described in the experimental methods chapter (Chapter 2). In order to characterize the cross-sections of the nitrided specimens, SEM, optical microscopy and AFM were used. The aim of the cross-sectional microscopy characterization is mainly to estimate the plasma nitrided layer thicknesses as well as to investigate the microstructure of the nitrided phases. In addition to these, some information about corrosion resistance of the plasma nitrided CoCrMo samples are obtained from the cross-sectional microscopy analyses.

#### 6.1. Cross-sections of Polishing Plasma Nitrided Samples

Figure 6.1 show cross-sectional SEM and optical microscope images of 6 and 20 h plasma nitrided specimens after polishing. The upper picture in Figure 6.1 shows the SEM image of 6 h plasma nitrided sample, while the bottom one shows the optical microscopy image of 20 h plasma nitrided sample. The optical microscopy image of the 20 h plasma nitrided specimen was taken in the DIC mode of optical microscope used (DIC mode of optical microscopy is explained in the experimental characterization chapter).

In Figure 6.1, both cross-sectional images clearly reveal the nitrided layer,  $\gamma_N$ -(CoCrMo), with relatively uniform layer thicknesses. In the cross-sectional microscopy results,  $\gamma_N$ -(CoCrMo) observation is quite similar with observations in the literature based on nitriding of CoCrMo studies (Öztürk 2006, Lutz 2008) and  $\gamma_N$ -(FeCrNi) observations based on nitriding of austenitic stainless steels (Öztürk 2009, Ozturk 1995). As can be seen from this, the 20 h nitrided layer thickness is nearly constant compared to the 6 h nitrided layer thickness. According to the thickness calculations

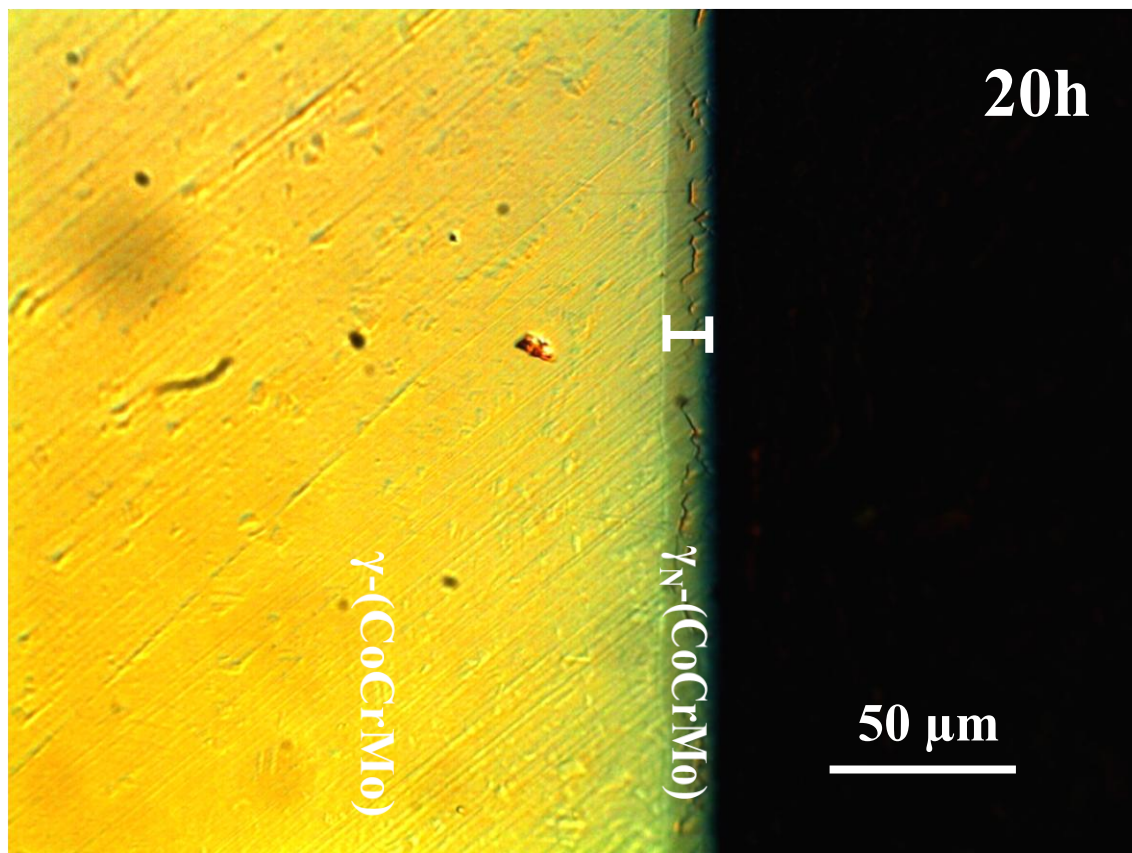
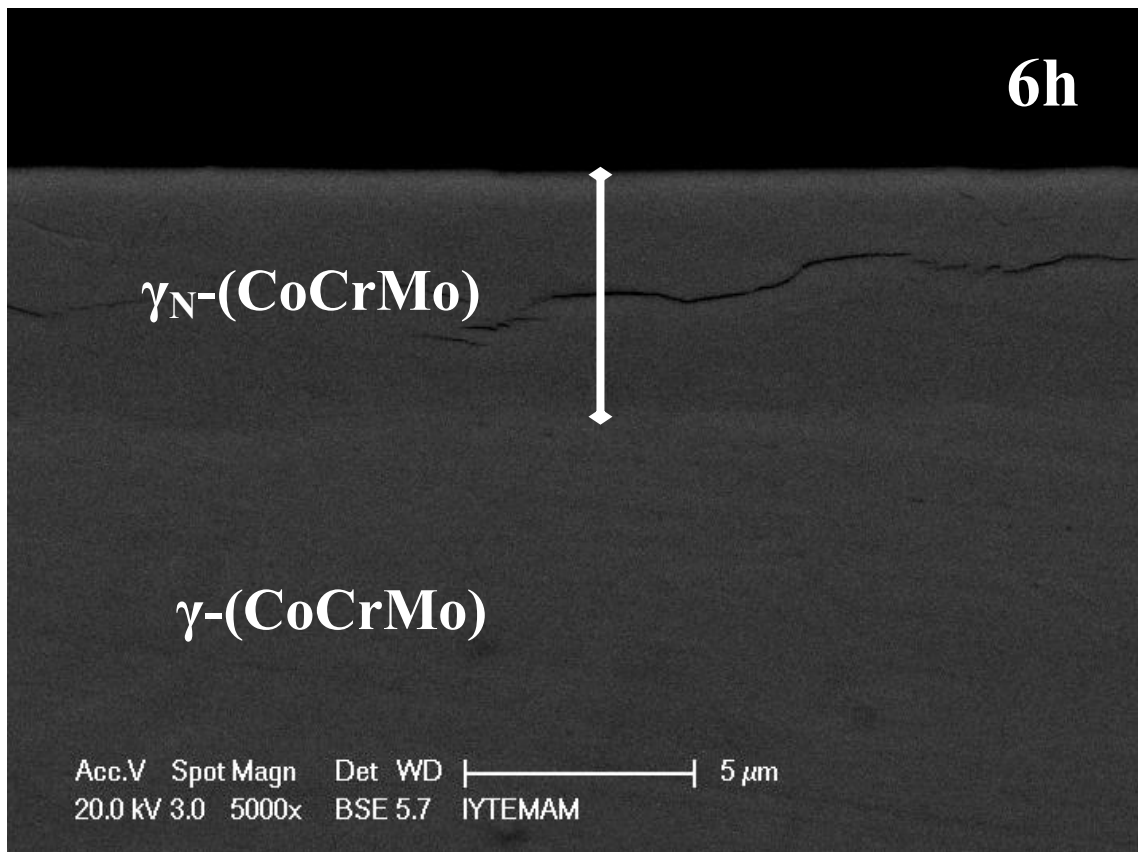


Figure 6. 1. SEM (top) and optical microscopy (bottom) images of the cross-sections of 6 and 20 h plasma nitrided samples, respectively, after polishing.

obtained from the cross-sections after polishing, the thickness of 6 h nitrided layer changes from 5.01  $\mu\text{m}$  to 5.48  $\mu\text{m}$  based on the several polished cross-sectional SEM pictures, while the thickness of the 20 h nitrided layer is measured as 10.52  $\mu\text{m}$  based on the several polished cross-sectional optical microscopy pictures. Based on the several images, the average thicknesses of the 6 and 20 h nitrided specimens were found to be 5.40  $\mu\text{m}$  and 10.50  $\mu\text{m}$ , respectively. The variations in the  $\gamma_{\text{N}}$  layer thicknesses according to the SEM analysis of the 6 h nitrided sample may be due to the larger nitrogen depths in the (200) grains as opposed to the (111) grains as it was shown to be the case according to the XRD semi-quantitative results of the plasma nitrided samples. The average thickness values of 1, 2, 4, 6 and 20 h nitrided layers are listed in Table 6.1 based on the analyses of polished cross-sectional SEM, optical microscopy and DIC optical microscopy measurements.

Also, in Figure 6.1, longitudinal cracks (structural defects) were observed along the 6 and 20 hours nitrided layers. The reason for the cracks are due to the compressive stresses in the  $\gamma_{\text{N}}$  layer due to the large lattice expansions in the plasma nitrided layers. In addition to the compressive stresses operating in the nitrided CoCrMo layers, it is assumed that the reason for the defect formation (cracks) along the  $\gamma_{\text{N}}$  layers of 6 and 20 h nitrided samples may be contributed by the texture development from the [111] direction to the [200] direction.

## **6.2. Cross-sections of Electrochemically Etched Plasma Nitrided Samples**

Polished cross-sections of the nitrided samples (Figure 6.1) were electrochemically etched (as described in the experimental section) and then their images were obtained by SEM. Figure 6.2 shows the cross-sectional SEM images of 2, 6 and 20 h plasma nitrided CoCrMo samples after electrochemical etching. Note that the cross-sectional SEM images were taken under different magnifications in order to obtain more accurate results about the nitrided layers. The cross-sectional SEM images of three samples clearly reveal the nitrided layers,  $\gamma_{\text{N}}\text{-(CoCrMo)}$ , with relatively uniform layer thicknesses. For the electrochemically etched cross-sectional 2, 6 and 20 h nitrided samples, several SEM images along the nitrided layer were used to estimate the layer thicknesses, presented in Table 6.1. The microscopy results of the electrochemically etched cross-sectional samples correlate well with the results obtained



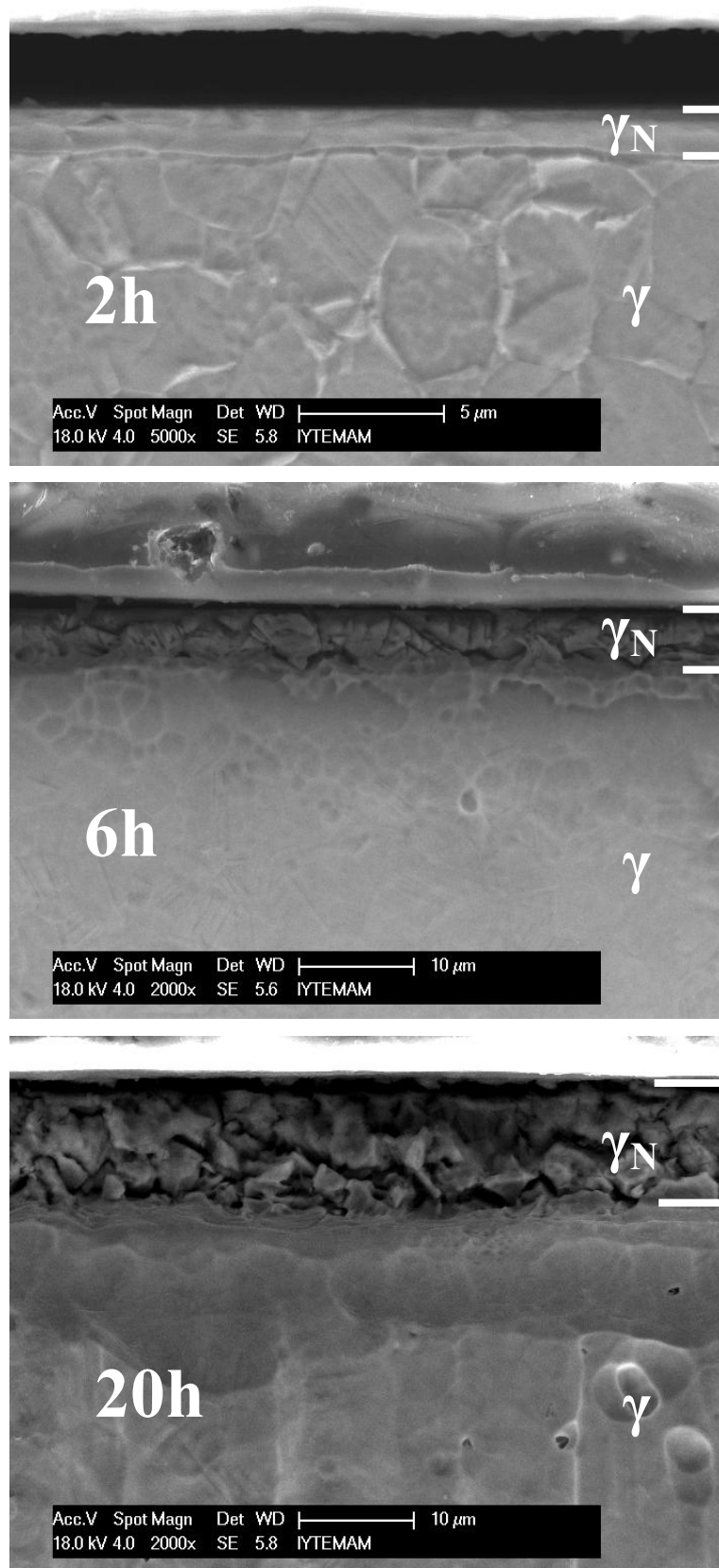


Figure 6. 2. Cross-sectional SEM images of 2, 6 and 20 h plasma nitrided samples after electrochemical etching.

from the polished cross-sectional samples (Figure 6.1). As can be seen from Table 6.1, the average thicknesses of the electrochemically etched 2, 6 and 20 h layers are 1.67, 4.90 and 10.25  $\mu\text{m}$ , respectively, while the average thicknesses of the polished 2, 6 and 20 h layers are 1.77, 5.12 and 10.43  $\mu\text{m}$ , respectively. The difference between these two measurements are less than 5%.

The cross-sectional SEM photomicrograph of the 2 h plasma nitrided sample in Figure 6.2 clearly reveal grain structure of the underlying CoCrMo substrate phase after the electrochemical etching. As can be seen from the cross-sectional SEM image of the 2 h nitrided sample, the grain boundaries of the substrate are not revealed when the substrate phase reaches the interface of the nitrided layer. The SEM image of this sample also shows that the  $\gamma_{\text{N}}$  layer is not attacked by the applied etchant (5 ml HCl and 100 ml  $\text{H}_2\text{O}_2$ ) during the electrochemical etching process. This may be due to the fact that the  $\gamma_{\text{N}}$ -(CoCrMo) phase has a better corrosion resistance compared to the substrate  $\gamma$ -(CoCrMo) phase. As contrary to the cross-sectional SEM results of the 2 h nitrided sample, the electrochemical etching of the 6 and 20 h cross-sectional samples did not reveal the grains of underlying CoCrMo substrate phase. This may be due to the fact that the acid solution used during the electrochemical etching of the 6 and 20 h nitrided cross-sections was not freshly prepared (it was the same acid solution that was used for the etching of the 2 h nitrided cross-section). It is believed that the impurities in the acid solution due to the previous etching (electrochemical etching of the 2 h nitrided cross-sectional sample) might have affected the strength of the acid solution used in the 6 and 20 h nitrided cross-sectional samples. Although the etching solution did not etch the substrate regions of the 6 and 20 h samples, however, it etched the nitrided layers for both samples. As can be seen from Figure 6.2, the 6 and 20 h plasma nitrided layers composed of  $\gamma_{\text{N}} + \text{CrN}$  show worse corrosion resistance compared to the 2 h nitrided sample. For the 6 and 20 h nitrided cross-sections, the SEM images clearly reveal the grain structures along the nitrided layers. It is assumed that the homogeneous CrN formation along the 6 and 20 h nitrided layers (based on the GIXRD results in Chapter 4) renders the corrosion resistance of  $\gamma_{\text{N}}$ -(CoCrMo) phase.

Typical cross-sectional SEM microstructures of plasma carburized (between 400  $^{\circ}\text{C}$  and 600  $^{\circ}\text{C}$ ) CoCrMo alloy (similar chemical composition to the CoCrMo used in this study) were found in the study of X.Y.Li et.al. (Li 2007). According to the study, when plasma carburizing temperatures are below 475  $^{\circ}\text{C}$  the plasma carburized layers appear unaffected by the etchant used in electrochemical etching (25% HCl at 10 V),

although the microstructure of the CoCrMo substrate is clearly revealed showing that the corrosion resistance (to acid) of the carburized layers is better than the CoCrMo substrate. However, when the plasma carburizing temperature reaches to 600 °C the plasma carburized layers suffered from heavily electrochemical attack indicating that the corrosion resistance (to acid) of the carburized layers is deteriorated by plasma carburizing at 600 °C. As can be seen from the cross-sectional SEM picture of the 2 h nitrided sample, in comparison, the results of the corrosion resistance of the  $\gamma_N$ -(CoCrMo) phase correlate well with the  $\gamma_C$ -(CoCrMo) phase based on the study of X.Y.Li et.al. Although there is no clear data for long plasma nitriding durations of CoCrMo alloys in literature, in addition to the high plasma carburizing temperature (600 °C), it is assumed that the longer plasma nitriding times (6 and 20 hours) also renders the corrosion resistance of the CoCrMo alloy due to the formation of CrN. In literature, also, there are studies (O. Öztürk 1995, 2009) investigating the corrosion resistance of the nitrided 300 series stainless steels (304 and 316L SS),  $\gamma_N$ -(FeCrNi). According to these studies, the  $\gamma_N$ -(FeCrNi) is also corrosion resistive phase. These results correlate well with the results obtained from the cross-sectional SEM analysis of the 2 h nitrided sample. These findings can be interpreted to be the first results related to the corrosion resistance of the  $\gamma_N$ -(CoCrMo) phase, however, there is no data found in the literature investigating the corrosion resistance of the  $\gamma_N$ -(CoCrMo) phase. In a recent nitriding study of CoCrMo alloy (Lutz 2008), the SEM analysis was done in the nitrided cross-sectional samples that were etched by 1 keV Ar<sup>+</sup> beam. While the SEM images in this study reveal the nitrided layers ( $\gamma_N$  at 380 °C), nothing is said about the corrosion resistance of the nitrided layers.

### **6.3. Cross-sections of Ar Beam Etched Plasma Nitrided Samples**

The polished cross-sections of the plasma nitrided CoCrMo alloys were also etched by using Ar<sup>+</sup> ions (as described in the experimental section). Figure 6.3 shows the cross-sectional SEM results of 1, 2, 4, 6, and 20 h plasma nitrided samples after Ar<sup>+</sup> ion beam etching. Note that the cross-sectional SEM images were taken under different magnifications in order to obtain more accurate results about the nitrided layers. The last image (bottom right), taken with an optical microscope, belongs to the 20 h plasma

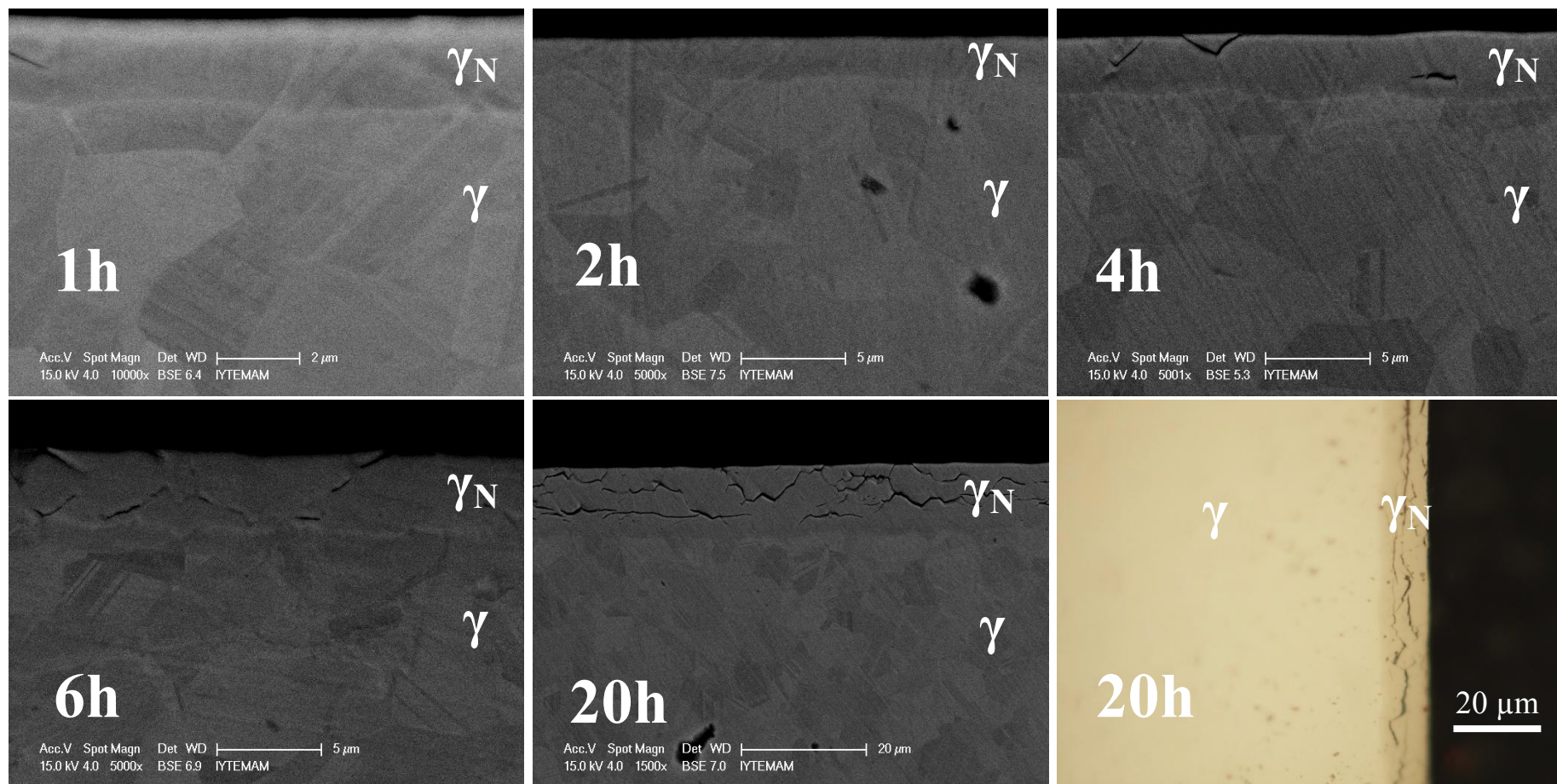


Figure 6. 3. Cross-sectional SEM images of the 1, 2, 4, 6 and 20 h plasma nitrided CoCrMo samples after Ar beam etching. The bottom right figure shows a cross-sectional optical microscopy image of the 20 h plasma nitrided sample.

nitrided sample. In Figure 6.3, the cross-sectional SEM images of the samples clearly reveal the nitrided layer,  $\gamma_N$ -(CoCrMo), with relatively uniform layer thicknesses. The average values of 1, 2, 4, 6 and 20 hours nitrided layer thicknesses were estimated from several cross-sectional photomicrographs taken along the nitrided layers after Ar beam etching. The microscopy results of the  $\text{Ar}^+$  beam etched cross-sectional samples correlate well with the results obtained from the polished and electrochemically etched cross-sectional samples. As can be seen from Table 6.1, the average thicknesses of the  $\text{Ar}^+$  beam etched 1 and 4 h layers are 2.04 and 2.90  $\mu\text{m}$ , respectively, while the average thicknesses of the polished 1 and 4 h layers are 1.99 and 2.98  $\mu\text{m}$ , respectively. The difference between these two measurements are less than 5%. Also, the average thickness of the  $\text{Ar}^+$  beam etched 6 h layer is 4.68  $\mu\text{m}$ , while the thickness of the electrochemically etched 6 h layer is 4.90  $\mu\text{m}$ . The thicknesses of the nitrided layers obtained from the cross-sectional SEM, optical microscopy and AFM measurements can be found in Table 6.1.

As contrary to the cross-sectional SEM results after electrochemical etching, the cross-sectional SEM photomicrographs of the all plasma nitrided samples in Figure 6.3 clearly reveal the grain structure of the underlying CoCrMo substrate phase,  $\gamma$ -(CoCrMo), after Ar beam etching. This is due to that all the cross-sections of the nitrided samples were exposed to energetic  $\text{Ar}^+$  ions and homogenously etched. As can be also seen from the  $\text{Ar}^+$  beam etched cross-sectional SEM images of the all nitrided samples, the interfaces between the nitrided layers ( $\gamma_N$  phase for the 1, 2 and 4 h nitrided layers and  $\gamma_N$  and CrN phases for the 6 and 20 h nitrided layers) and substrate phase,  $\gamma$  are clearly visible due to the etching.

According to Figure 6.3, the  $\gamma_N$  layers appear practically featureless, whereas the substrate contains distinct microstructural features, grains and grain boundaries. Except for the cross-section of the 1 h nitrided sample, the grain boundaries of the CoCrMo substrates completely disappear at the intersections of the substrate and the nitrided layers for 2, 4, 6 and 20 h nitrided samples. As can be seen from Figure 6.3, for the cross-section of the 1 h nitrided sample, the grain boundaries from the substrate continue into  $\gamma_N$  fading out as the surface is approached to higher N contents. This correlates well with the GDOES nitrogen concentration depth profiles (Chapter 7) showing that nitrogen concentration decrease with depth. The nitrogen concentration depending on the depth will be discussed in details in the next chapter.

Another interesting feature obtained from Figure 6.3 is that there are no cracks in 1 and 2 h plasma nitrided layers, but in 4, 6 and 20 h ones. As can be seen from these figures, the 4 h nitrided sample has less defective structure along the nitrided layer compared to the 6 and 20 h nitrided layers. Also, the 6 h nitrided layer has less defective structure along the nitrided layer compared to the 20 h one. It can be correlated that when the nitriding time increases, the defect formation in the nitrided layers increases. This means that the macroscopic stresses and grain rotations in the nitrided layers increase when the plasma nitriding time increases causing more defects in the nitrided layers. This correlates quite well with the XRD experimental data presented in Chapter 4.

In addition to the cross-sectional SEM and optical microscopy measurements, cross-sectional AFM measurements were performed to estimate the thicknesses of the Ar<sup>+</sup> beam etched cross-sections of the nitrided layers. The cross-sectional AFM images of the 1, 2, 4 and 6 h plasma nitrided layers did not give information about the thicknesses of nitrided layers, although, as can be seen from Figure 6.4, the thickness of the 20 h nitrided layer were estimated from the Ar beam etched cross-section of the 20 h nitrided sample (listed in Table 6.1). This is due to that the etching with energetic Ar<sup>+</sup> ions did not make a height difference between substrate and the nitrided phases except 20 hours nitrided layer sample.

In Figure 6.4, highly defective structure (cracks) are observed in the 20 h nitrided layer correlating well with the polished and electrochemically etched SEM and optical microscope cross-sectional observations (Figure 6.1 and Figure 6.3). As described before, the macroscopic stresses and the grain rotations in the nitrided layers cause these structural defects, however, the cracks observed in the Ar<sup>+</sup> beam etched SEM cross-sections for the 4 and 6 h nitrided samples were not observed in the cross-sectional AFM measurements. This may be due to that the crack formation in the 4 and 6 h nitrided layers are not intensive compared to the 20 h one.

Table 6.1 lists the thicknesses of the plasma nitrided layers obtained from the cross-sectional SEM, optical microscope and AFM measurements of the plasma nitrided samples after polishing, electrochemical etching and Ar<sup>+</sup> beam etching. According to this table, it can be said that the thickness calculations of the plasma nitrided layers correlate quite well with each other, however, there are some differences due to resolutions of the measurement techniques (SEM, optical microscopy (OM) and AFM). As can be seen from Table 6.1, the agreement between L<sub>SEM</sub> and L<sub>OM</sub> may be better for

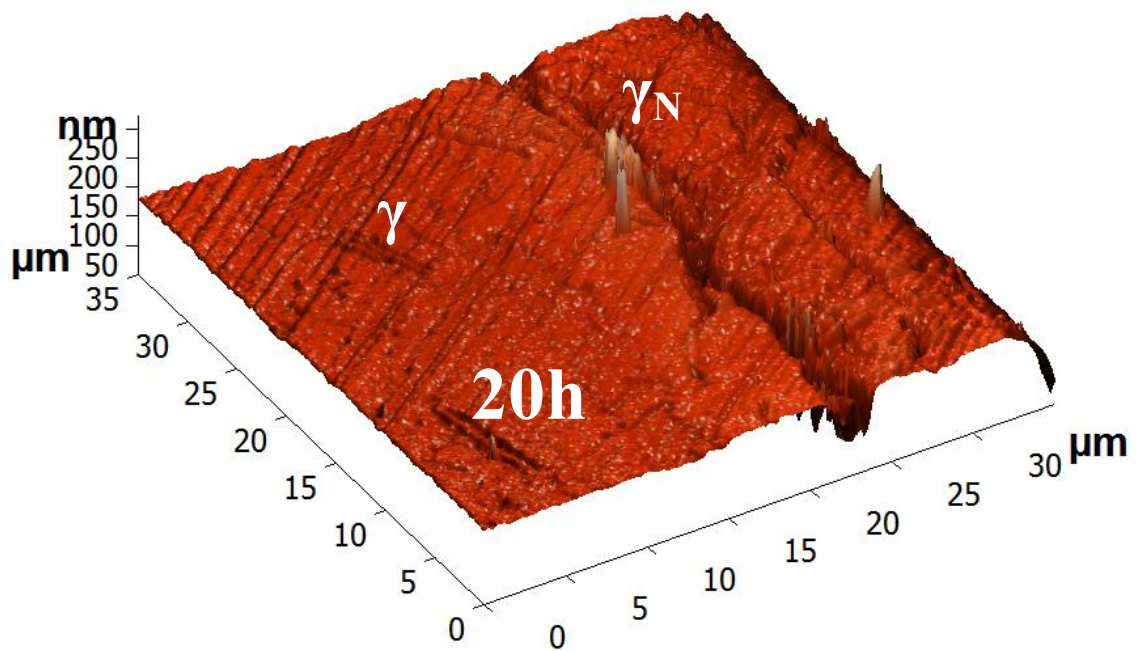
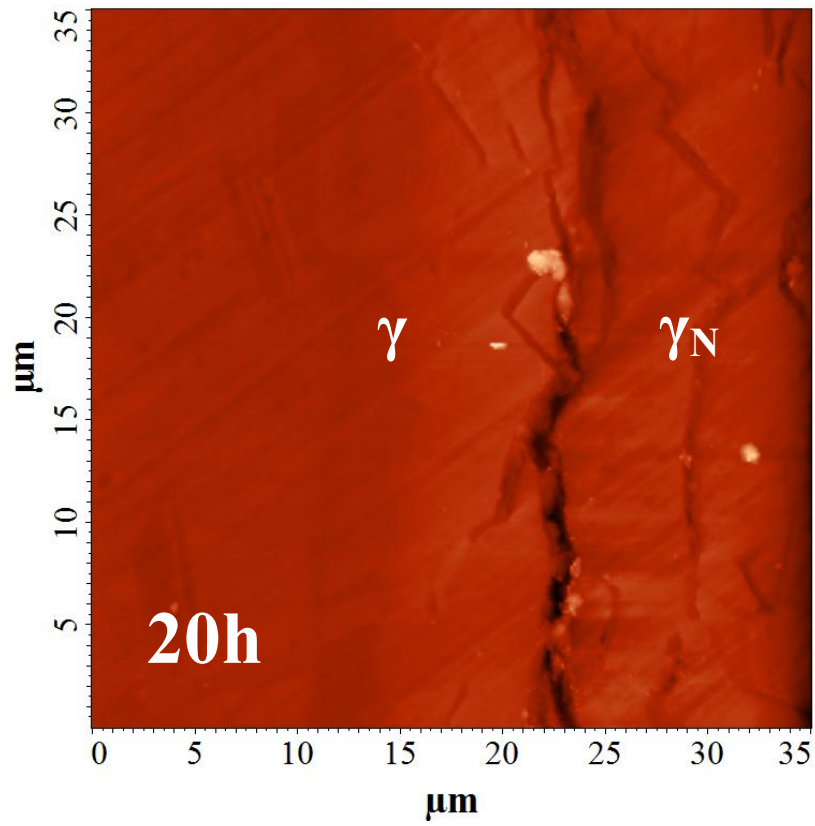


Figure 6. 4. 2-D and 3-D cross-sectional AFM graphs of 20 h plasma nitrided sample.

thicker layers (6 and 20 h nitrided layers) and poorer for thinner layers (1, 2 and 4 h nitrided layers). These thickness values also correlate with those that were obtained through the GDOES analysis experiments (to be discussed later).

Table 6. 1. Plasma nitrided layer thicknesses calculated after cross-sectional microscopy experiments (N.T: Nitriding Time).

N.T (h)	POLISHING				ELECTROCHE -MICAL ETCHING	Ar BEAM ETCHING			
	L <sub>SEM</sub> ( $\mu\text{m}$ )	L <sub>OM</sub> ( $\mu\text{m}$ )	L <sub>OM(DIC)</sub> ( $\mu\text{m}$ )	<L> ( $\mu\text{m}$ )		L <sub>SEM</sub> ( $\mu\text{m}$ )	L <sub>OP</sub> ( $\mu\text{m}$ )	L <sub>AFM</sub> ( $\mu\text{m}$ )	<L> ( $\mu\text{m}$ )
1	1.94	2.00	2.02	1.99	-	2.22	1.86	-	2.04
2	1.46	1.96	1.89	1.77	1.67	2.04	1.92	-	1.98
4	3.00	3.05	2.90	2.98	-	2.80	2.99	-	2.90
6	5.40	5.00	4.95	5.12	4.90	3.93	5.44	-	4.68
20	10.40	10.38	10.5	10.43	10.25	11.06	11.1	~13	11.70

The thicknesses of the 1 and 2 h plasma nitrided layers correlate quite well with the thicknesses found from the XRD semi-quantitative results, while the thickness of the 4 h plasma nitrided layer is found pretty much higher in cross-sectional layer thickness calculations compared to XRD semi-quantitative thickness calculations. As can be seen in Table 6.1, the thickness of 4 h plasma nitrided layer changes between 2.80  $\mu\text{m}$  and 3.05  $\mu\text{m}$ , but the average thickness values of 4 h plasma nitrided layer, as considering nitrogen-in-interstitial sites model and no nitrogen-in-interstitial sites models, were found to be 2.09  $\mu\text{m}$  and 1.76  $\mu\text{m}$ , respectively. The large differences between the thickness calculations of 4 h nitrided layer may be due to the XRD probe depths at the Bragg angles of interest. The Cu-K $\alpha$  x-rays used in the XRD experiments may not penetrate enough into the underlying substrate phases below the 4 h nitrided layer, so, the integrated areas of the 4 h nitrided x-rays peaks used in Equation 3.9 for calculation of the thicknesses of the nitrided layers are not reliable for the 4 hours nitrided sample, and may be interpreted as lower than the correct thickness value. Note that, in the XRD spectrum of 6 and 20 hours plasma nitrided samples (Figure 4.2), there is no observation of CoCrMo substrate peaks due to the limited x-rays penetration.



## CHAPTER 7

### COMPOSITION-DEPTH ANALYSES OF PLASMA NITRIDED LAYERS

#### 7.1. Compositional Characterization

Elemental compositions of the plasma nitrided CoCrMo and substrate samples were characterized by GDOES and EDX. Figure 7.1 shows the GDOES result of the substrate (D15) specimen. Atomic concentrations of the Mo, Si, Mn and N are multiplied by 10 in order to see clearly in the image. The composition of the substrate elements obtained from the GDOES measurement is listed in Table 7.1, both in at.% and wt.%. The results correlate well with the elemental composition (Chapter 2) data which were reported by TIPSAN (CoCrMo supplier company) and the EDX results.

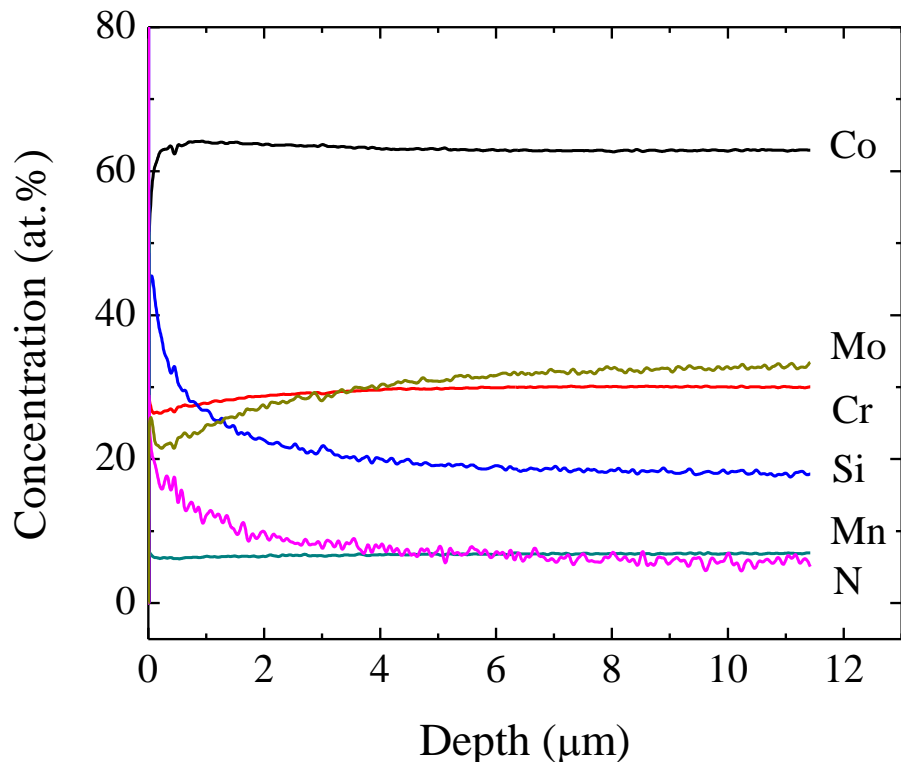


Figure 7. 1. The GDOES results of CoCrMo substrate sample (D15). Concentrations of Mo, Si, Mn and N elements are multiplied by 10 for clarity.

Table 7. 1. The GDOES elemental composition result of CoCrMo substrate.

	Co	Cr	Mo	Mn	Si	N
at.%	62.94	30.12	3.26	0.68	1.84	0.57
wt.%	64.59	27.40	5.43	0.64	0.81	0.13

Figure 7.2 shows the GDOES results for the 6 h nitrided sample. The concentration of the elements Mo, Si and Mn were multiplied by 10. As can be seen in Figure 7.2, the nitrogen has diffused to a depth of  $\sim 5.5 \mu\text{m}$  correlating quite well with the thickness results obtained from the cross-sectional SEM and optical microscopy measurements ( $5.12 \mu\text{m}$  for polished cross-sectional measurements). Also, it can be seen from Figure 7.2, the atomic weight concentrations of base elements of CoCrMo (Co, Cr and Mo) decrease in the nitrided layer. This might be due to that, during plasma nitriding, the nitrogen places interstitial sites in CoCrMo crystal structure by decreasing the atomic weight concentration of the base atoms in the lattice. But, as can be noticed, the decrease in the atomic weight concentration of chromium (Cr) is less compared to the concentration decrease of Co and Mo. This may be attributed to the CrN formation in  $\gamma_N$  layer agreeing with the GIXRD results of the 6 and 20 h plasma nitrided samples (Chapter 4). Also, the atomic weight concentration of the additive elements of Si and Mn do not decrease with the increasing nitrogen concentration. As can be seen from Figure 7.2, the average nitrogen concentration shows steady state up to the depth of  $\sim 4.5 \mu\text{m}$ , and then shows a very sharp decrease until the interface of the nitrided and the substrate phases ( $\sim 6 \mu\text{m}$ ). The average concentration in the steady state part of the concentration-depth profile of the 6 h nitrided sample is estimated to be  $\sim 25 \text{ at.}\%$  correlating quite well with the EDX data (Table 2).

Elemental compositions of the plasma nitrided CoCrMo alloy was also investigated by EDX. The EDX data were collected from both the surfaces and cross-sections of the plasma nitrided CoCrMo samples. The EDX measurements of the 2 h (from surface) and 4 h (from cross-section) plasma nitrided samples are presented in Figure 7.3. The red rectangular shapes on the images in Figure 7.3 represent the area from which the EDX data were collected. Note that the nitrogen concentrations obtained are different on the surfaces and on the cross-sections. According to the cross-sectional EDX measurements, the nitrogen concentration decreases with the depth ( $18 \text{ at.}\%$  on the cross-sectional area in Figure 7.3) compared to the surface EDX results ( $24.87 \text{ at.}\%$

on the surface area in Figure 7.3). The average nitrogen contents obtained from the surface EDX results correlate with the GDOES results.

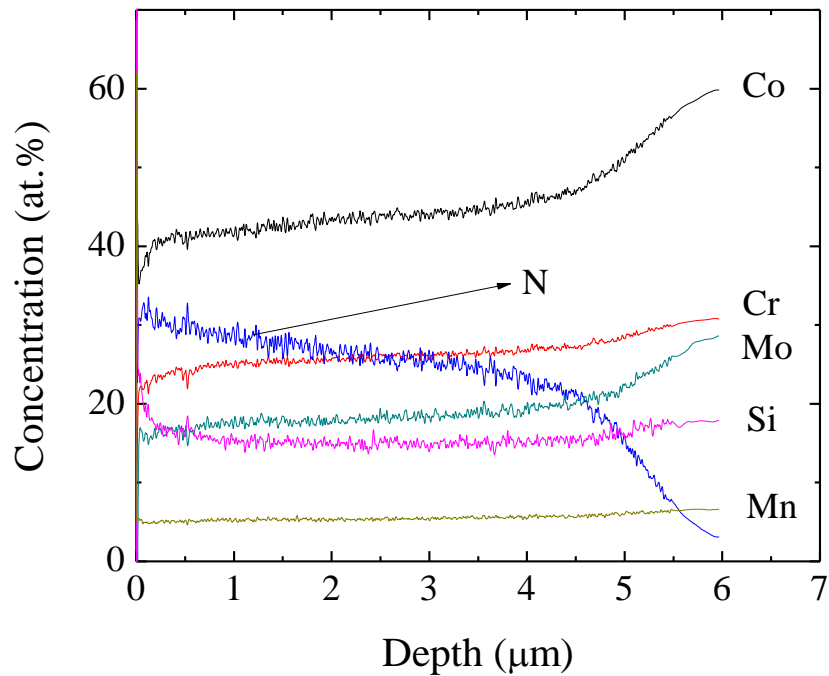


Figure 7. 2. The GDOES results of 6 h plasma nitrided CoCrMo sample. The concentration of Mo, Si and Mn are multiplied by 10 for clarity.

Table 7.2 lists average elemental compositions of the plasma nitrided CoCrMo samples after surface EDX measurements. The EDX measurements were repeated a few times on the nitrided surfaces for each nitrided CoCrMo sample. The concentrations listed in Table 7.2 represents average values of the elements. The data presented in the Table 7.2 correlates well with the GDOES composition depth results. As can be seen from the table, nitrogen concentration reached nearly 25 at.% for all the nitrided samples independent of the plasma nitriding time.

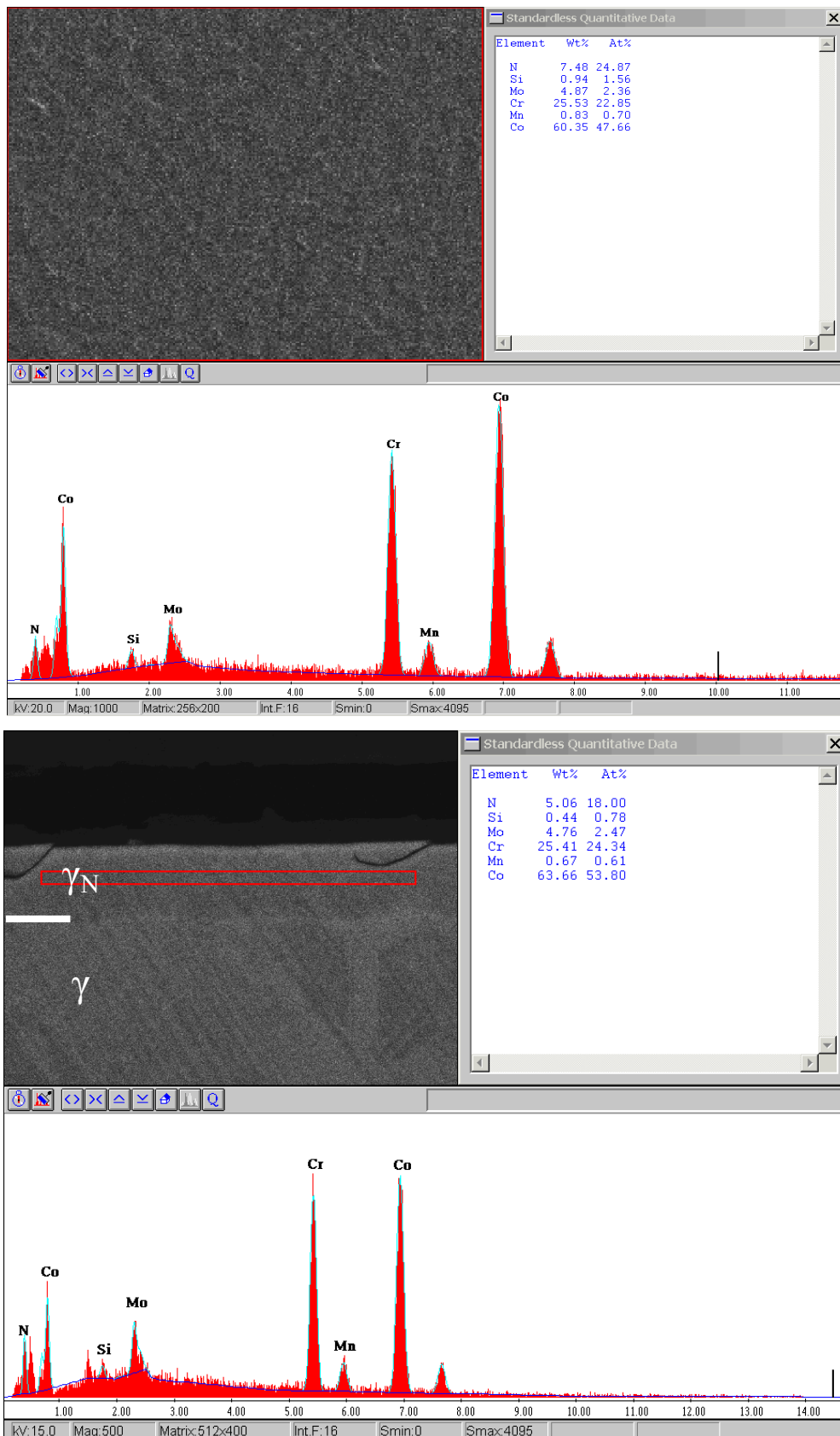


Figure 7. 3. The EDX results of the 2 h nitrided sample from surface (above) and cross-sectional EDX result of 4 h nitrided layer (below).

Table 7. 2. The EDX average elemental composition values of plasma nitrided CoCrMo samples as well as substrate sample (D15) (obtained on the surfaces).

	wt.%						at.%					
	0h	1h	2h	4h	6h	20h	0h	1h	2h	4h	6h	20h
Co	65.0	60.0	59.6	60.1	59.0	59.7	63.4	47.8	46.7	47.7	47.2	47.0
Cr	27.3	25.6	25.6	25.9	26.0	25.9	30.3	23.0	22.8	23.2	23.5	23.1
Mo	6.01	5.7	5.2	5.4	6.3	5.4	3.6	2.8	2.5	2.6	3.1	2.6
Mn	0.6	0.7	0.7	0.6	0.6	0.6	0.6	0.6	0.6	0.6	0.5	0.5
Si	1.0	0.5	1.0	0.6	1.0	0.8	2.1	0.9	1.7	1.0	1.7	1.4
N	-	7.4	7.8	7.4	7.2	7.7	-	24.9	25.7	24.8	24.0	25.4

## 7.2. GDOES Nitrogen Concentration Depth Profiles

Figure 7.4 comprises GDOES nitrogen concentration profiles of the plasma nitrided CoCrMo samples. As can be seen from these profiles, the nitrogen concentration values are quite high at the surfaces of plasma nitrided samples (ranging from ~ 28 to ~ 32 at.%) and then they decrease slowly to a level of ~ 20 to ~ 22 at.%. Within this range, the nitrogen depth profiles are of nearly rectangular shape for all the samples corresponding to a depth of ~70-80% of the nitrided layer. One study (Lutz 2008), investigating the nitrogen diffusion into CoCr alloys by plasma immersion ion implantation and plasma nitriding experiments at different process temperatures ranging from 250 °C to 600 °C, found out that the surface concentration of nitrogen reaches values between 30 and 35 at.%, nearly independent of the process temperature.

Concerning the nitrogen diffusion in CoCrMo in the nitriding experiments, there are few studies (Lutz 2008, Lutz 2009) intended to explain the nitrogen diffusion. The nitrogen depth profiles in austenitic stainless steels (ASS) and CoCr alloys (Figure 7.4) exhibit plateau-type shapes slowly decreasing from surface, followed by a rather sharp leading edge. According to the profiles in Figure 7.4, the leading edge starts around 20 at.%. Such profiles are not consistent with the standart analytical solution of the diffusion equation (Philibert 1991). In the literature, such diffusional profiles are well-known for 300 series austenitic stainless steels (300, 304, 310, 316). Also, such nitrogen diffusion profiles have recently been obtained for CoCr alloys (Lutz 2008, Lutz 2009, Johanna Lutz 2008) as well as the concentration depth profiles of the nitrided samples

in this study correlate well with the literature data related to the nitrogen diffusion in CoCr alloys.

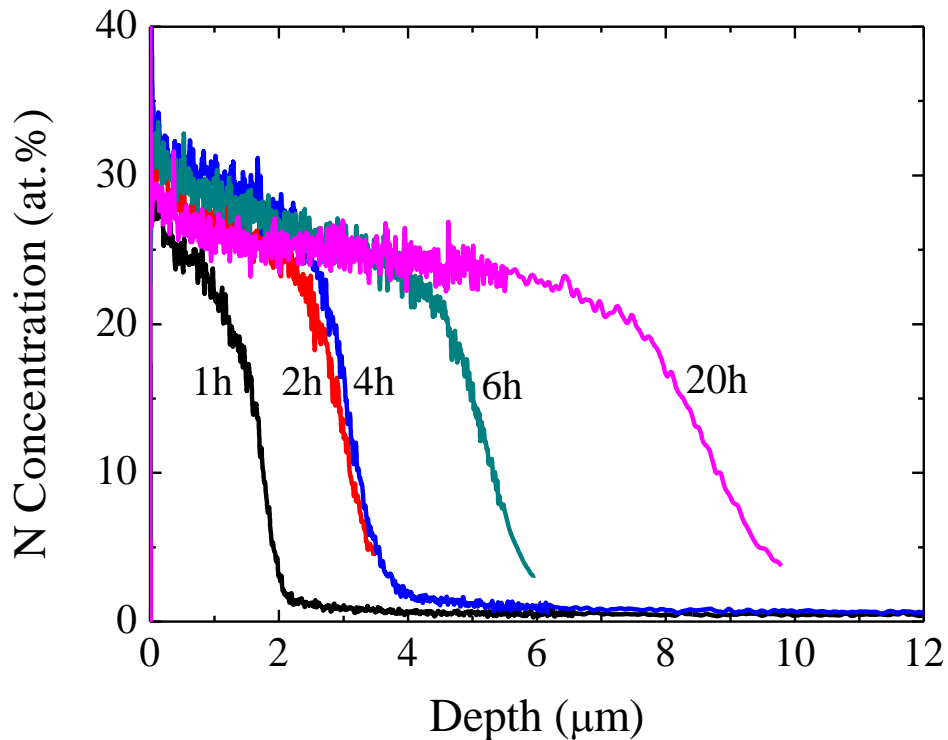


Figure 7. 4. GDOES nitrogen concentration-depth results of plasma nitrided CoCrMo samples.

Another key point in the Figure 7.4 is the nitrogen penetration depths for the plasma nitrided samples. Table 7.3 lists the nitrided layer thickness values obtained from the GDOES nitrogen concentration depth profiles. It is believed that the nitrogen concentration at the interfaces (between the nitrided and the substrate phases) obtained from the cross-sectional SEM and optical measurements may not be zero and it can change. In a study (Manova 2008), the thickness of the nitrided layer (plasma immersion ion implantation of 304 austenitic stainless steel at 450 °C) are estimated at 5 at.% of the nitrogen concentration in GDOES concentration-depth profile. The thickness values in Table 7.3 are estimated by taking 5 at.% (as a reference) nitrogen concentration of the leading edge of the nitrogen concentration depth profiles. The GDOES thickness data correlates quite well with the cross-sectional and XRD thicknesses results for 1, 4, 6 and 20 h plasma nitrided samples. But, as can be seen from Table 7.4, there is a big difference between the thickness values of previous results

(cross-section and XRD) and GDOES results for the 2 h plasma nitrided sample. The thickness of the 2 h nitrided layer is measured to be 3.37  $\mu\text{m}$  from the GDOES results, while the thickness of the 2 h nitrided layer changes between 1.80 and 2.13  $\mu\text{m}$  in previous thickness results (cross-section and XRD) representing the difference of 72% and 46%, respectively. The reason of the difference has not been identified yet. It is believed that the cross-sectional microscopy results give more accurate results compared to the GDOES thickness values for the thicknesses of the plasma nitrided layers.

Table 7. 3. Thickness of the plasma nitrided layers obtained from the GDOES results.

Nitriding Time (h)	1	2	4	6	20
Thickness ( $\mu\text{m}$ )	1.92	3.37	3.51	5.68	9,44

The understanding of N diffusion mechanism in CoCrMo and FeCrNi alloys is very important. According to the literature, the selective bonding between N and Cr has a major effect on the mobility of nitrogen (Singer 1984). There have been reported some nitrogen diffusion mechanisms (Williamson 1998, Perdaza 2007, Abrasonis 2005, He 2003) in order to explain the nitrogen enhancement of austenitic stainless steels (ASS) under various types of nitriding techniques and of various treatment conditions. One of these models is the trapping/detrapping model (TD) used to explain the shape of nitrogen profiles (Williamson 1994, Parascandola 2000, Abrasonis 2005, Christiansen 2006). According to the TD model, chromium (Cr) alloying element in the fcc austenitic lattice plays a significant role in enhancing nitrogen diffusivity in these alloys. Also another study of D. L. Williamson et. al (Williamson 1992) suggested a qualitative model that the substrate element Cr in the fcc austenitic stainless steels (ASS) plays a significant role when coupled with the high flux N beam. Another study experimented N diffusion in both fcc ASS and fcc Fe and found that nitrogen concentrations are higher in ASS comparing to in pure fcc  $\gamma\text{-Fe}$  (Ozturk 1995). This can be explained by the trapping effect of Cr on the migration of nitrogen in these materials. These studies can be seen as the first indications of Trapping-Detrapping model (TD) (Williamson 1994, Parascandola 2000), which is very consistent with many experimental results. The TD model was confirmed experimentally by  $^{15}\text{N}$  and  $^{14}\text{N}$  sequential implantation

(Parascondola 2000). It is most probably expected that similar diffusion mechanisms are also taking place in the fcc CoCrMo alloy because of the alloying element of Cr.

In the case of nitrogen diffusion, some characteristics are not well understood up to now. Some of these are the influence of alloy composition, especially Cr content, (Williamson 1998, Perdaza 2007) and crystalline orientation (Abrasonis 2005, He 2003) on the diffusion rate.

Concerning the Cr role in the nitrogen diffusion mechanism, one key point is the difference of Cr content in 300 series fcc stainless steels (SS) (15-20 at.% Cr) and CoCrMo alloy (~30 at.% Cr). According to the similar studies in literature, it is found that nitrogen diffuses deeper in fcc SS compared to fcc CoCr alloys (at 400 °C). One study (Öztürk 2009) found that the plasma nitriding of 316L austenitic stainless steel (an fcc FeCrNi alloy) for 72 min at 430 °C forms ~ 6 µm thick  $\gamma_N$  layer. Having similar conditions with this study, the plasma nitriding of CoCrMo for 1 h at 400 °C forms ~ 2 µm thick  $\gamma_N$  layer (Table 6.1). Note that the nitrogen diffuses 3 times deeper in 316L SS. Considering the TD model, this thickness difference can be explained that Cr atoms act as trap sites for the nitrogen and, a faster diffusion of nitrogen is observed when all traps are saturated. Diffusion under the influence of traps controls the transport of nitrogen in stainless steel and CoCrMo, with dynamic trapping at the Cr atoms of the alloys. So, it is expected that it takes longer time to saturate all Cr traps for CoCrMo (compared to ASS) exhibiting thinner nitrided layers due to more Cr content in CoCrMo.

The XRD results of the plasma nitrided samples (Chapter 4) indicates that the nitrogen diffusivity has a strong dependence on the crystalline orientation. According to the XRD results, the nitrogen diffuses more in the (200) oriented grains compared to the (111) grains and higher nitrogen concentration is found in the (200) planes compared to the (111) planes producing anisotropic lattice expansions and different nitrided layer thicknesses along the nitrided layers. This dependence of the diffusivity on the crystalline orientation has not thoroughly been explained in literature, however, the TD model have an ability to reproduce the shape and even fit the nitrogen depth profiles. In order to explain anisotropic lattice expansions (Hirvonen 1985, Mandl 2000, He 2003) and thickness variations of the nitrided layers (Williamson 1994), anisotropic dependence of the strain on the stress was proposed. It was suggested that the anisotropic charge density redistribution under strain could cause a variation of the diffusion coefficient along different lattice directions (Mandl 2000). The vast majority of the experiments cited above have been carried out on polycrystalline stainless steel.



In polycrystals, individual grains with different orientations exhibit different nitrided layer thicknesses, which contribute to an average depth profile (He 2003, Grigull 2000).

Some experiments (Pranevicius 2001) were intended to research the single crystal effects of ASS and reached that the results are in a good agreement with the above experiments. A comparative study was done by G. Abrasonis et. al. that single-crystalline ([001], [011] and [013] orientations) and polycrystalline 316L austenitic stainless steel were nitrided at moderate temperature (400 °C) by ion beam nitriding. Higher nitrogen penetration depths were found for the [100] and [013] oriented single crystals than the (110) one, correlating with the XRD results of this study, on contrary to nitrogen concentration does not depend on the orientation (~23-24 at%) (Rivière 2007). According to (Rivière 2007), in each single crystal, lattice expansions in the nitrided layer are similar for all the crystallographic planes. Also, it is stated that during nitriding a simultaneous lattice rotation of a few degrees ( $< 5^\circ$ ) of the nitrided layer accompanies the lattice expansion. This result suggests the results obtained from GIXRD experiments of this study concerning the texture development in the [200] direction.

Some other models were also proposed to explain the shape of nitrogen depth profiles and the enhanced diffusivity in fcc SS. The concentration dependent diffusion [ $D(C_N)$ ] model was proposed as an alternative to the TD model. The [ $D(C_N)$ ] model is motivated by the expansion of the austenitic lattice by dissolution of nitrogen, which is likely to facilitate the transfer of a nitrogen atom from octahedral to the tetrahedral interstitial sites (Christiansen 2008). Also, Christiansen et. al. (Christiansen 2008) reported experimental data confirming both models combined to describe the nitrogen diffusion. His approach was that the concentration dependent diffusion model alone leads to strong underestimation of the diffusion coefficient for low concentrations where the trapping has its most prominent influence. Hence the general diffusion model would take into account both the concentration dependent diffusion model and the TD model. In another study (Riviere 2002), radiation induced defects were proposed to explain the fast diffusion, but it was shown that nitrogen diffusion is faster than that of the induced defects (Williamson 1998). Recently another explanation was suggested by Abrasonis et.al. (Abrasonis 2006) based on a quasi-particle-enhanced mobility that stable and mobile intrinsic localized modes might be created by energetic ions and propagate along atomic chains, which could accelerate the diffusion of interstitial nitrogen atoms.

Also, microstructure effects, such as grain boundary diffusion, cannot be excluded considering nitrogen diffusion, which makes more difficult the interpretation of the results. One study (Manova 2007) attempted to find a correlation between the grain size of 304 austenitic stainless steel nitrided by PIII and the diffusion rate during ion nitriding. According to this study, thinner layers are highly correlated with an increased average grain size (parallel and perpendicular to the diffusion direction). However, a strong influence on the diffusion rate and the microstructure is observed, a layer thickness much smaller than the crystallite size (by a factor of 5–10) contradicts this argument. It was shown by another group (Tong 2003) that a decrease in the grain size of the steel from 1000  $\mu\text{m}$  to 13 nm results in 1000 times faster diffusion in ion nitriding. Additionally, different data sets are reported in the literature concerning nitrogen diffusion in austenitic stainless steel without providing any information about the grain size (Williamson 1998, Blawert 1999, Mändl 2003). In comparison the CoCrMo and 316L SS in terms of grain size, the grain size changes between  $\sim 25$  and  $50 \mu\text{m}$  for 316L SS substrate (Öztürk 2009), while the grain size changes between  $\sim 5$  and  $15 \mu\text{m}$  for CoCrMo substrate (Turkan 2004). So, it is expected that the nitrogen diffuses deeper in the CoCrMo compared to the 304 SS. But it was contrarily found that the nitrogen diffuses deeper in 316L SS (plasma nitrided for 72 min at  $430 \text{ }^\circ\text{C}$ ) compared to the CoCrMo (plasma nitrided for 120 min at  $400 \text{ }^\circ\text{C}$ ), the thickness of the nitrided layers are  $\sim 6$  and  $2 \mu\text{m}$ , respectively. There is no model trying to explain these strongly diverging results. It is believed that these difference are attributed to the Cr (different contents in SS and CoCrMo) which has a important role in nitrogen diffusion. No systematic study on nitrogen diffusion in steel and CoCrMo in connection with microstructure is performed, so the published diffusion values could be misleading.

In addition to these, the microstructure of the samples (FeCrNi and CoCrMo alloys) should have an effect on the nitrogen diffusion. The defects (twin boundaries or dislocations, slip planes) or dual phases ( $\epsilon$  and  $\gamma$  in CoCrMo) in microstructure can play a decisive role on the nitrogen diffusion length. It is considered that the model of formation of expanded austenite phase related to the microstructure of the substrate sample could help explain the exact mechanism of the nitrogen diffusion during nitriding. In order to investigate the microstructure effect on the nitrogen diffusion for stainless steel and CoCrMo alloys, it can be a good idea to study with the samples which have different microstructural properties, such as different volume fraction of  $\epsilon$  phase.

### 7.3. Nitrogen Diffusion Constant Analysis

After obtaining thicknesses of the nitrated layers (Table 6.1) from the cross-sectional spectroscopy measurements (SEM, AFM and optical microscopy), after polishing, electrochemical and Ar beam etching, and the GDOES concentration depth profiles, the thickness data are used in nitrogen diffusion constant analyses. The Equation 7.1 is used to estimate the nitrogen diffusion coefficients at 400 °C for different thickness data sets.

$$L \sim \sqrt{Dt} \quad (7.1)$$

In this equation, L is the thickness of the nitrated layer, D is the diffusion coefficient and t is the nitriding time. This equation is obtained by solving the Fick's second law in boundary conditions (Crank 1975).

Figure 7.5 shows the calculation of the nitrogen diffusion coefficients from experimental nitrated layer thickness of the cross-sectional Ar<sup>+</sup> beam and electrochemical etching as well as the GDOES data. The Equation 7.1 is used to calculate nitrogen diffusion constants. The nitrogen diffusion coefficients are obtained after least square curve-fitting of each data set. The results ( $D_N$ ) are listed in Table 7.5. As can be seen from Table 7.5, the diffusion coefficient values change between  $\sim 1 \times 10^{-11}$  and  $2 \times 10^{-11}$  cm<sup>2</sup>/s and the average nitrogen diffusion coefficient,  $D_{ave}$ , is  $1.5 \times 10^{-11}$  cm<sup>2</sup>/s. The reason for the slight difference of the diffusion coefficients is due to that the nitrated layer thicknesses are found to be slightly different for each measurement (cross-sectional spectroscopy and GDOES).

In the literature, there are few studies which intend to investigate the nitrogen diffusion coefficient of fcc CoCrMo for nitriding experiments. One recent study (Lutz 2008) has reported some nitrogen diffusion coefficients for stellite SY21 medical alloy (with elemental compositions similar to the CoCrMo alloy used in this study) nitrated (without hydrogen) between 300-700 °C for 2 h by using plasma immersion ion implantation (PIII) and plasma nitriding (PN). According to this study, the nitrogen diffusion coefficients are determined to be  $\sim 2 \times 10^{-12}$  cm<sup>2</sup>/s (PN) and  $\sim 3 \times 10^{-11}$  cm<sup>2</sup>/s (PIII) at 400 °C. It can be said that the nitrogen diffusion coefficient of the PIII one of the study correlates quite well with the results presented in Table 7.4, while the PN one

does not. It is clear that the diffusion coefficient of the PN one is lower compared to the PIII one and the data presented in Table 7.4. It is believed that the slower diffusion in PN experiment in this study is related to the hydrogen which was not used in the PN experiments. As explained before, hydrogen contributes the nitrogen diffusion by removing the native oxide layer ( $\text{Cr}_2\text{O}_3$ ) on the CoCrMo and FeCrNi alloys.

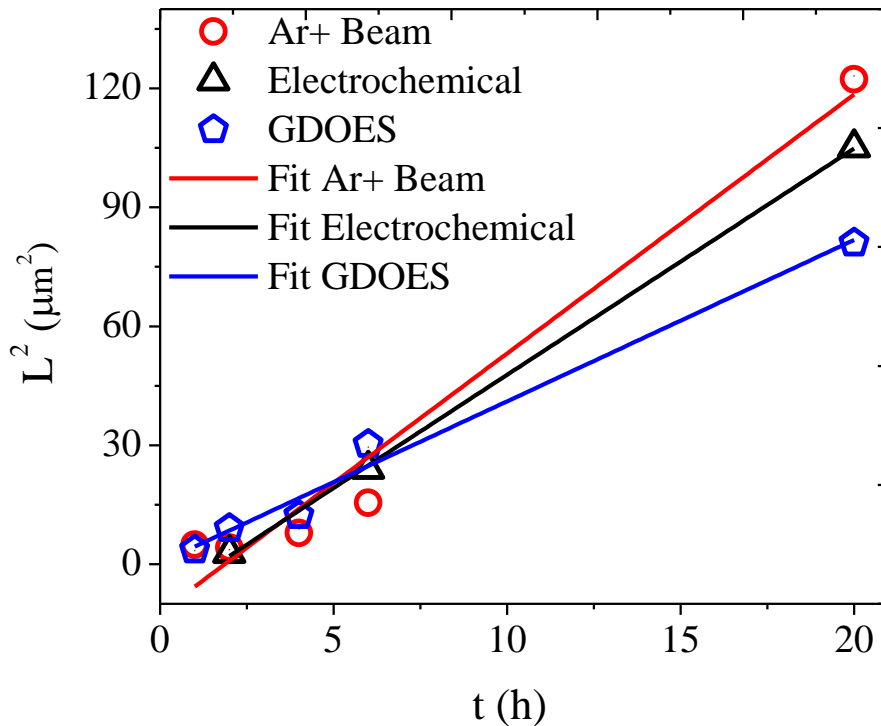


Figure 7. 5. Calculation of the nitrogen diffusion coefficients from the experimental nitrated layer thickness of the cross-sectional Ar+ beam and electrochemical etching as well as the GDOES data.

There are many nitrogen diffusion coefficient values for 300 series austenitic stainless steel presented in the literature (G. Abrasonic 2005). One study (S. Mandl 2002) reports that the nitrogen coefficient for fcc  $\gamma$ -(Fe,Cr,Ni) [304, 310, 316 SS] at 400 °C varies between  $10^{-10}$ - $10^{-12}$   $\text{cm}^2/\text{s}$ . Another study is the nitrogen ion implantation of 316L stainless steel at 400 °C (Williamson 2001). In this study, the nitrogen diffusion constant is found to be  $3.9 \times 10^{-11}$   $\text{cm}^2/\text{s}$ . As can be seen from the literature data for the nitrogen diffusion coefficients, there are not so many difference for diffusion coefficients between the literature data and the results listed in Table 7.5. It is believed that this good correlation comes from the structural (same crystal lattice) and

compositional (Cr alloying element which has an important role for the nitrogen diffusion) similarities.

Table 7. 4. Nitrogen diffusion coefficients obtained from Figure 7.5.

Thickness Measurements (by using)	Diffusion Coefficient (cm <sup>2</sup> /s)
Ar Beam etching	1.815 x 10 <sup>-11</sup>
Electrochemical etching	1.586 x 10 <sup>-11</sup>
GDOES	1.131 x 10 <sup>-11</sup>
D <sub>ave</sub>	1.510 x 10 <sup>-11</sup>

One reason for the similar diffusion coefficients for CoCrMo and FeCrNi alloys may arise from the structural similarities between two alloys (fcc crystal structures, similar lattice constants). However, the CoCrMo alloy has a two phase crystal structures, mainly fcc  $\gamma$ -(CoCrMo) and hcp  $\epsilon$ -(CoCrMo) (as thin plates in  $\gamma$ -(CoCrMo) grains). It is believed that the substrate  $\epsilon$ -(CoCrMo) converts to the substrate  $\gamma$ -(CoCrMo) and then into the  $\gamma_N$ -(CoCrMo) during the plasma nitriding. But the effects of  $\epsilon$ -(CoCrMo) on the nitrogen diffusion into CoCrMo is still unidentified and this needs further investigation. In the literature, there is no data presented to explain the  $\epsilon$ -(CoCrMo) effect on the nitrogen diffusion into CoCrMo.

Another reason for the similar diffusion coefficients for CoCrMo and FeCrNi alloys may arise from the compositional similarities between two alloys (Cr alloying element). The atomic concentration of Cr is  $\sim 30$  at.% for CoCrMo alloy, while the atomic concentration of Cr changes between 18 at.% and 20 at.% for 300 series austenitic stainless steels (304, 316L, etc.). As explained before, according to the TD model, Cr has a significant role in the nitrogen diffusion during the nitriding of the CoCrMo and FeCrNi alloys. It is believed that the slight difference in Cr elemental composition in these alloys may be the reason for the slightly different nitrogen diffusion constants. The Cr effect on the nitrogen diffusion in CoCrMo may be negative because Cr atoms act as trap sites for N, and so the incoming nitrogen atoms and molecules encounter an obstacle to diffuse deeper. From this, it is expected that nitrogen

can diffuse deeper in the FeCrNi alloys during the nitriding compared to the CoCrMo alloys due to lower Cr concentration.

Also, being different from the nitrogen diffusion of austenitic stainless steels at 400 °C, CrN formation are observed for longer plasma nitriding times (6 and 20 hours) in CoCrMo samples (XRD results). It can be assumed that this CrN formation may affect the nitrogen diffusion for longer nitriding times for the CoCrMo alloys. According to the TD model, the effect of CrN formation on the nitrogen diffusion may be positive because the incoming nitrogen atoms and molecules do not encounter any obstacle to diffuse into the CoCrMo. This is due to that the Cr, which bonds earlier N atoms and molecules and forms CrN, can not acts as trap site for the incoming nitrogen, so, the nitrogen can diffuse deeper.

## CHAPTER 8

# MECHANICAL CHARACTERIZATION OF PLASMA NITRIDED LAYERS

### 8.1. Microhardness Results

Vicker's microhardness measurements were done on all the plasma nitrided (for 1, 2, 4, 6 and 20 h) and CoCrMo substrate specimens. Several indentations were made with each of the following loads: 5, 10, 25, 50, 100, 200, 300, 500 and 1000 grams for each sample. The area of each indentation was measured by either an optical microscope (connected to the Vicker's microhardness system) or an SEM depending of the load (5 and 10 g). A Vicker's microhardness was calculated from the applied load and the average area of a particular indentation in units of  $\text{kg}/\text{mm}^2$ .

Table 8. 1. Average diagonal lengths ( $\mu\text{m}$ ) and probe depths ( $\mu\text{m}$ ) of the substrate according to the applied microindenter loads (grams). Average values were obtained from several indents for each load.

Applied Load (g)	5	10	25	50	100	200	300	500	1000
Average Diagonal Length ( $\mu\text{m}$ )	5.34	6.22	9.87	13.12	18.74	26.88	34.78	45.61	65.44
Average Probe Depth ( $\mu\text{m}$ )	0.76	0.89	1.41	1.87	2.68	3.84	4.97	6.52	9.35

Table 8.1 lists average diagonal lengths and probe depths of the indenter with respect to the applied loads for the substrate sample. One of the important points in Table 8.1 is the average indent depths of the indenter used in the hardness measurements. As can be seen in the table, the indent depths changes from  $\sim 1.0 \mu\text{m}$  (for 25 g load) to  $\sim 9.0 \mu\text{m}$  (for 1000 g load). As mentioned in the cross-sectional characterization section, the thickness of the nitrided layers varies from  $\sim 2 \mu\text{m}$  to  $\sim 10 \mu\text{m}$  which are very close to the average probe depths of applied loads. This means that, in some cases of microhardness measurements, the used indenter penetrates more than the plasma nitriding layer thicknesses resulting in increasing of the substrate

contribution to the hardness values of plasma nitrided layers. According to Table 8.1, it can be assumed that the more accurate results for the hardnesses of plasma nitrided phases are obtained from the 25 g loads microhardness measurements because less probe depth means less substrate addition to the microhardness of the plasma nitrided samples.

Table 8.2 lists the Vicker's microhardness (HV) data for the 1, 2, 4, 6 and 20 h plasma nitrided as well as CoCrMo substrate (0 h) samples. As can be seen from this, the plasma nitriding process applied to the CoCrMo alloy results in significant hardness improvement. In Table 8.2, there can clearly be seen two trends related to microhardness of the nitrided samples. For a given sample (nitrided sample), the microhardness decreases as the applied load increases. This is due to increased substrate contribution at higher loads. For example, at 1000 g load, the hardness of the 4 h nitrided specimen is 474 kg/mm<sup>2</sup> (close to the hardness of the substrate at that load; 433 kg/mm<sup>2</sup>), while, at 25 g load, the hardness of the 4 h nitrided specimen reaches 1327 kg/mm<sup>2</sup> (~ 3 times higher than the substrate hardness at that load and the hardness of the 4 h nitrided specimen at 1000 g load). The other trend is that the hardness of the nitrided samples increase as a function of plasma nitriding time at any load. For example, at 25 g load, the hardness of the 1 h nitrided sample increased to 956 kg/mm<sup>2</sup> (~ 2 times higher than the substrate hardness), while the hardness of the plasma nitrided layers reaches its peak point at 6 h plasma nitrided sample, 1709 kg/mm<sup>2</sup> (~ 3.6 times higher than the substrate hardness and ~ 2 times higher than the 1 h nitrided sample hardness).

As can be seen in Table 8.2, at 25 and 50 g loads, the hardness of the 20 h nitrided specimen lower than the 6 h nitrided specimen, even though the 20 h nitrided specimen has a thicker nitrided layer compared to the 6 h nitrided specimen. The reason may be due to excessive microstructural defect formation (cracks, observed in cross-sectional characterization of the 6 and 20 h nitrided layers) in the 20 h nitrided phase compared to the 6 h nitrided surface. The structural defects (cracks) in the 20 hours nitrided sample may render the hardness property of the 20 h nitrided sample. The microhardness results presented in Table 8.2 correlate reasonably well with the explanation that the thickness of the plasma nitrided layers increases with respect to the nitriding time and the substrate contribution to the hardness of the plasma nitrided samples decreases.

The decrease in hardness at high loads can be explained by the fact that, at high loads, the probe depth of the indenter exceeds the thickness of the plasma nitrided layer,



resulting in a large contribution of the rather softer substrate phase,  $\gamma$ -(CoCrMo). At smaller loads, the hardness measurement is affected more by the  $\gamma_N$ -(CoCrMo) layer and less by the  $\gamma$  phase. Note that nearly 10 times higher probe depth is observed at 1000 g load compared to the probe depth at 25 g load.

Table 8. 2. Vicker's microhardness (HV in kg/mm<sup>2</sup>) data for the nitrided specimens. The loads (first row) are in grams. The average Vicker's microhardness values in the table are estimated from the microhardness values of the 1, 2, 4, 6 and 20 h nitrided samples (without taking into account the substrate hardness).

Nitriding Time (h)	5	10	25	50	100	200	300	500	1000
0	325	478	476	539	528	513	460	446	433
1	1336	1256	956	866	596	571	524	487	461
2	-	-	989	780	617	477	530	491	450
4	-	-	1327	1020	747	602	561	536	474
6	-	-	1709	1641	983	712	625	576	518
20	-	-	1508	1499	1332	1020	903	707	588
H <sub>ave</sub>	1336	1256	1297	1161	855	676	629	559	498

Using the data in Table 8.2, the microhardness (kg/mm<sup>2</sup>) data of the plasma nitrided and substrate samples are plotted as a function of the applied load (N), presented in Figure 8.1. Also, in Figure 8.2, the substrate microhardness and the average microhardness of the plasma nitrided specimens ( for 1, 2, 4, 6 and 20 h) are presented as well as the least square fit of the substrate microhardness. The fit of the substrate hardness is a straight line. The microhardness result of the substrate was found after fit, to be 474 kg/mm<sup>2</sup>, and this value correlates well with the literature (450 kg/mm<sup>2</sup>) (O. Öztürk 2010).

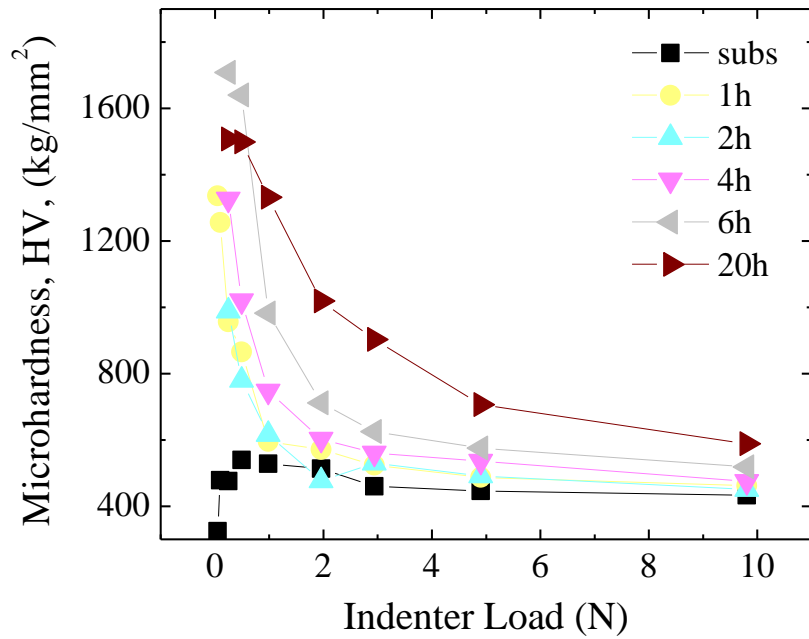


Figure 8. 1. Microhardness data for the plasma nitrided and CoCrMo substrate samples. The microhardness is in  $\text{kg/mm}^2$  ( $2000 \text{ kg/mm}^2 = 19.6 \text{ GPa} = \sim 20 \text{ GPa}$ ) and load in N ( $\text{kg.m/s}^2$ ).

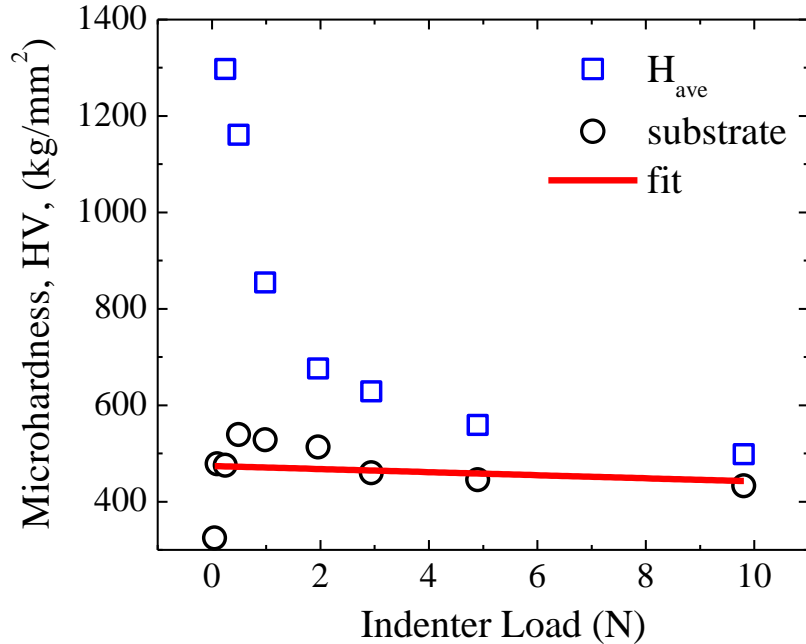


Figure 8. 2. Average microhardness of the plasma nitrided samples and the microhardness of substrate sample as well as the fit of the substrate. The microhardness is in  $\text{kg/mm}^2$  ( $2000 \text{ kg/mm}^2 = 19.6 \text{ GPa} = \sim 20 \text{ GPa}$ ) and load in N ( $\text{kg.m/s}^2$ ).

According to the hardness profiles in Figure 8.1 and Figure 8.2, in general, the untreated sample show low hardness, while the samples treated by plasma nitriding exhibit a high hardness even fairly high loads; note that the hardness values of the 20 h nitrided sample for 200 and 300 g loads are 1020 and 903, respectively. At applied loads ( $> 50$  g), the hardness value is the largest for the specimen nitrided for 20 h compared to the other specimens nitrided for 1, 2, 4 and 6 h. Although, the nitrided layer of the 20 h nitrided sample is rather thick, also, CrN precipitates distributed in the nitrided layer may contribute to higher hardness values for 20 h nitrided sample. So, enhanced hardness behaviour observed here can be due to the  $\gamma_N$  and CrN formations and thicker nitrided layers. Also, it is believed that the compressive stresses operating in the nitrided layers may add to the increased hardness.

## 8.2. Wear Results

The wear behaviour of the 2, 6 and 20 h plasma nitrided as well as the as-polished substrate (0h) samples (D30) were investigated by pin-on-disc wear measurements. In the experiments, a ruby ball of 6 mm in diameter was used at two different loads of 1 and 4 N with corresponding contact stresses of 0.216 GPa (22 kg/mm<sup>2</sup>) and 0.342 GPa (35 kg/mm<sup>2</sup>), respectively. Sliding wear distances were chosen to be 200 and 600 m. Wear tracks were investigated with the help of optical profilometry and optical microscope. The information about wear tracks obtained by the optical profilometry is presented in Table 8.3. As can be seen in Table 8.3, at any load (1 and 4 N) and sliding wear distance (200 and 600 m), the nitrided sample surfaces have better wear resistance compared to the substrate. For example, at 1 N load and 200 m sliding distance, the wear volume of the substrate is 44  $\mu\text{m}^3$ , while the wear volume of the samples nitrided for 2, 6 and 20 h are 27, 2 and 4  $\mu\text{m}^3$ , respectively. As can be seen in Table 8.3, the wear volume, wear width and wear depth values increase with increasing applied loads (1 and 4 N) and sliding wear distances (200 and 600 m).

According to the results in Table 8.3, at any experimental wear condition, the wear widths for the 20 h sample are larger than those for the 6 h nitrided sample suggesting better wear resistance for the latter sample. This difference may be attributed to the structural changes taking place in the nitrided layers. As stated before in the microhardness results, the structural defects (cracks) may deteriorate the mechanical

properties of the plasma nitrided samples (the hardness of the 20 h plasma nitrided sample is lower than the 6 h one for 25 and 50 g loads). The poorer wear behaviour for the 20 h nitrided sample in comparison to the 6 h one can also be seen from the wear volume analysis results as well.

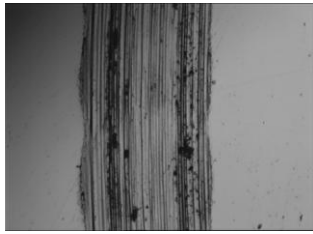
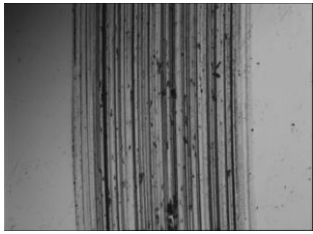
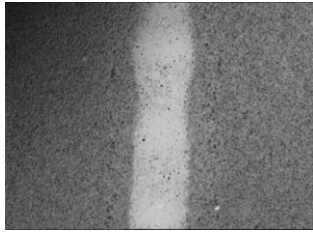
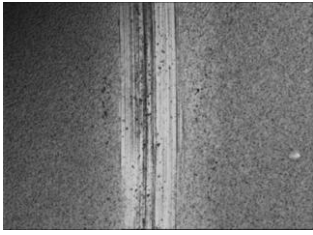
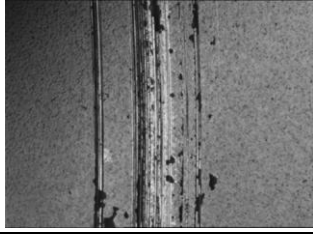
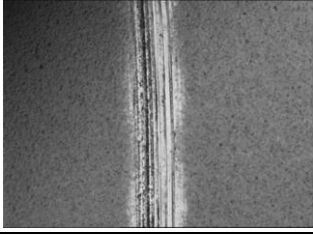
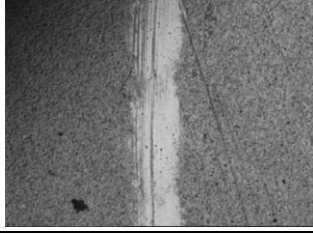
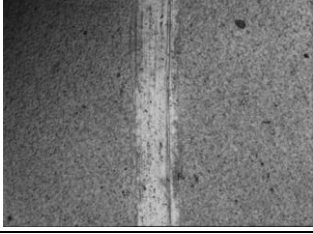
After wear experiments, the resultant wear tracks were investigated by optical microscopy. Some optical microscope images of the wear tracks of the 2, 6 and 20 h nitrided as well as substrate (0 h) surfaces are presented in Table 8.4; 1 N for 600 m (1 N-600 m) and 4 N for 200 m (4 N-200 m). In Table 8.3, there is clear evidence that the wear resistance increases with the plasma nitriding time. As seen in Table 8.3, the widths of the wear tracks decreases with respect to the plasma nitriding time (except 20 h), agreeing with the data, presented in Figure 8.4. This may be because of that longer plasma nitriding results in thicker nitrided layers causing stronger wear resistance. The wear width of the 6 hour nitrided sample for 1 N load and 600 m sliding distance is somehow anomalous in comparison to the other nitrided samples. The scratches, which are seen in the image, were possibly caused by wear debris that was picked up by the ball.

Table 8. 3. Wear volume, wear width and wear depth data of the wear tracks of 2, 6 and 20 h nitrided as well as substrate (0 h) samples for different wear conditions. The wear volume is estimated by multiplying cross-sectional wear areas and wear widths of the wear tracks.

Wear Conditions	Wear Volume ( $\mu\text{m}^3$ )				Wear Width ( $\mu\text{m}$ )				Wear Depth ( $\mu\text{m}$ )			
	0h	2h	6h	20h	0h	2h	6h	20h	0h	2h	6h	20h
1N 200m	440	27	2	4	255	130	88	158	-	0.37	0.06	0.08
1N 600m	450	51	74	72	333	148	166	170	2.70	0.59	0.96	0.84
4N 200m	1150	67	59	45	439	155	150	156	5.05	0.80	0.74	0.56
4N 600m	2460	185	144	187	503	204	193	307	-	1.42	1.24	1.94

Figure 8.3 exemplifies one of the optical profilometer wear track results (2 h nitrided specimen for 1 N load and 200 m sliding wear distance) used in wear volume, width and depth estimations. Figure 8.3 comprizes 2-dimensional and 3-dimensional as well as cross-sectional images of the track. There can be seen an abrupt cross-sectional wear image of 2 h plasma nitrided in Figure 8.3. This may be due to random wear debris accumulation during the sliding.

Table 8. 4. Optical images of wear tracks (1 N-600 m and 4 N-200 m) of 0, 2, 6 and 20 hours plasma nitrided samples.

	1 N-600 m	4 N-200 m
0h		
2h		
6h		
20h		

Based on the analyses of the wear tracks by optical profilometry track results (Table 8.3), the wear widths and volumes of the nitrided samples as a function of wear conditions (applied load and sliding wear distance), are plotted in Figure 8.4. The wear volumes were estimated by measuring the wear track cross-sectional area by the profilometer (bottom image of Figure 8.3). In Figure 8.4, the results suggest significant wear volume reductions for the nitrided specimens compared to the polished substrate alloy. As can be seen in Table 8.4 and Figure 8.4, the wear width results clearly show that the wear resistance is increased by the plasma nitriding treatment independent of the wear conditions.

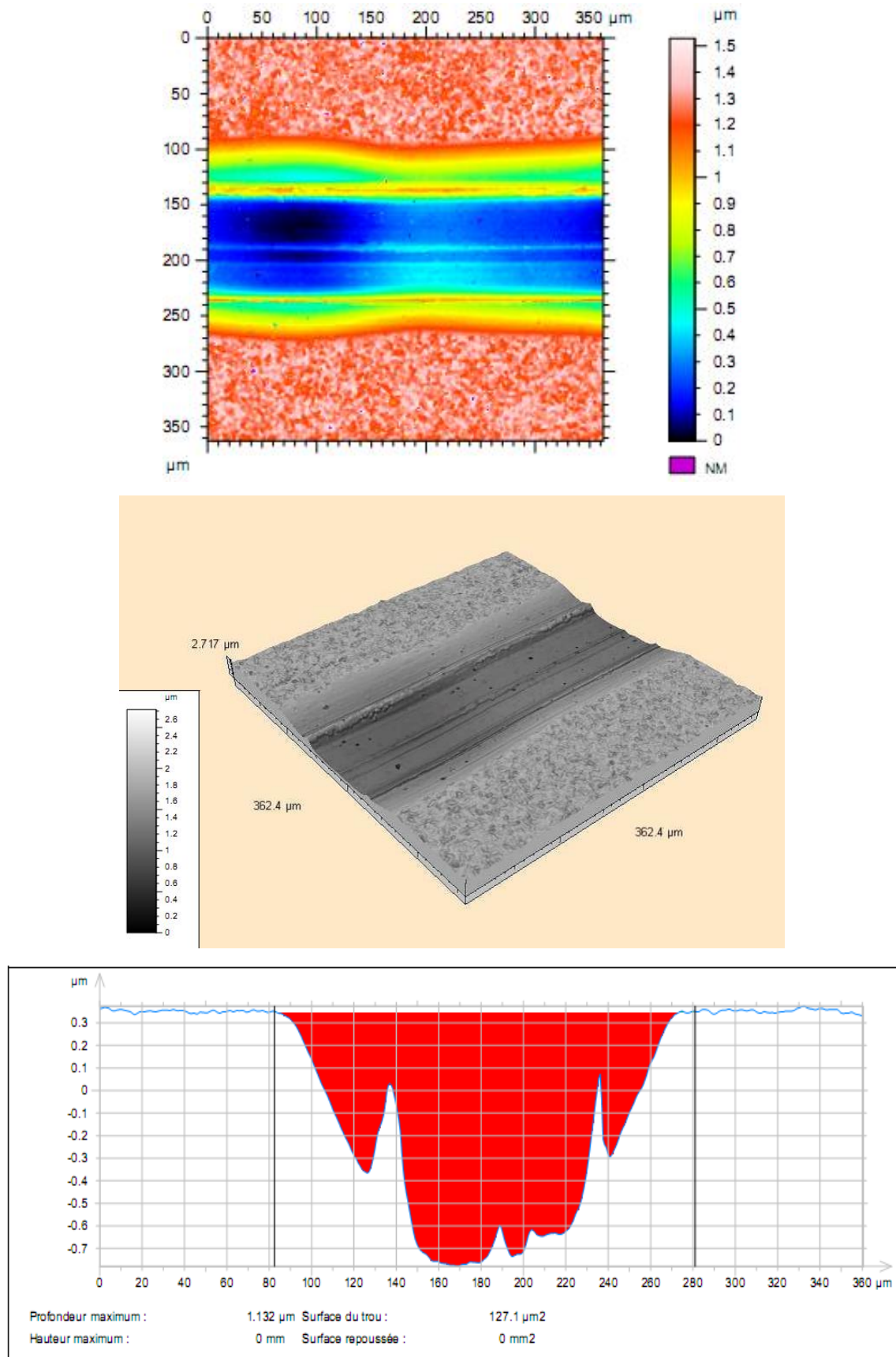


Figure 8. 3. Optical profilometer wear track results of the 2 h nitrided specimen for 1 N load and 200 m sliding wear distance used in wear results calculations.

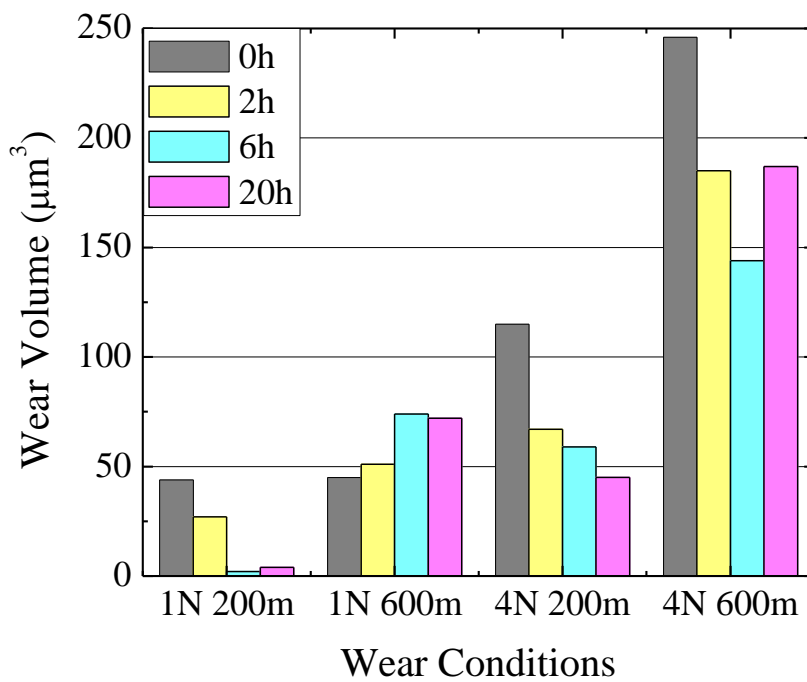
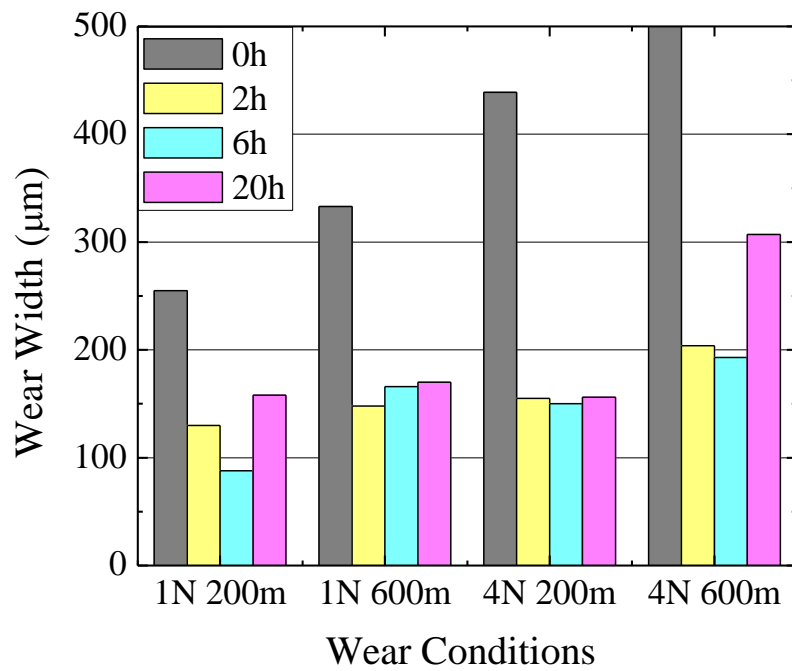


Figure 8. 4. Wear widths and volumes for the plasma nitrided specimens for all the wear conditions (loads = 1, 4 N; sliding wear distance = 200, 600 m). For the substrate sample (0 h), the estimated wear volume values (Table 8.3) are divided by 10 for comparison purposes.

In general, the wear resistance of the bulk material (CoCrMo) is enhanced by plasma nitriding. Furthermore, the longer plasma nitriding time is found to be more effective for the enhanced wear resistance due to the thicker nitrided layers. Reduction in wear obtained with plasma nitriding is generally thought to result from the strengthening of the wearing surface (Williamson 1990). The observed relative increase in the wear resistance of the nitrided samples are in good agreement with the observed hardness profiles in that the nitrided specimens have higher surface hardness.



## CHAPTER 9

### CONCLUSIONS

#### 9.1. Summary and Discussion

In this study, microstructural, compositional and mechanical characterization of CoCrMo alloy RF plasma nitrided under a gas mixture of 60% N<sub>2</sub> – 40% H<sub>2</sub> for a substrate temperature of 400 °C, and plasma nitriding times of 1, 2, 4, 6 and 20 h was investigated. The experimental results in the preceding chapters clearly show that the plasma nitriding leads to the development of new phase,  $\gamma_N$ -(Co,Cr,Mo), which is called expanded phase (solid solution phase or nitrogen in interstitial sites phase) and enhanced mechanical properties of the surface of the CoCrMo alloy.

The XRD results of the plasma nitrided samples (Chapter 4) indicate that the nitrogen diffusivity has a strong dependence on the crystalline orientation. According to the XRD results, the nitrogen diffuses deeper in the (200) oriented grains compared to the (111) oriented grains and more nitrogen concentration is found in the (200) planes compared to the (111) planes producing anisotropic lattice expansions and different nitrided layer thicknesses along the nitrided layers. The experimental XRD results indicate larger lattice expansions in the (200) planes compared to the (111) planes. The difference is attributed in part to the compressive residual stresses prevailing in the nitrided layers.

The XRD results suggest a preferential (200) orientation of  $\gamma_N$  grains parallel to the surface with increasing nitriding times. When the plasma nitriding time increases, [111] oriented plasma nitrided grains rotate in [200] direction due to nitrogen incorporation to the grains. The  $\gamma_N$ (200) planes (parallel to the surface) are almost dominant on the surface of 6 and 20 h plasma nitrided CoCrMo samples implying strong grain rotations (texturing).

The XRD and GIXRD data clearly show some structural changes taking place in the CoCrMo samples nitrided for 6 and 20 h, resulting in CrN phase ( $2\theta = \sim 37.5^\circ$ ). According to GIXRD results, CrN formed in 6 and 20 h plasma nitrided layers has a homogenous distribution in the  $\gamma_N$  layer.

According to AFM and optical interferometry results, the plasma nitrided surfaces became rougher with respect to the nitriding time. Comparing to as-polished CoCrMo surface, the average roughness of the plasma nitrided surfaces increased about 15 times with the increasing nitriding time. The main reason for the roughness development is due to the different expansion rates of differently oriented grains during the nitriding. Also, it is believed that the compressive stresses might contribute to the roughness increase of the nitrided surfaces.

According to the surface SEM results, structural defects (intergranular cracks) occur on the plasma nitrided CoCrMo surfaces. The main reason for the structural defects is due to high compressive stresses in the nitrided layers. Also, it is believed that the texture development contributes to the structural defects in the nitrided layers.

Cross-sectional SEM and optical microscopy results clearly reveal the nitrided layer,  $\gamma_N$ -(CoCrMo), after polishing, electrochemical and  $\text{Ar}^+$  beam etching with a reasonably well defined interface between the  $\gamma_N$  layer and the CoCrMo substrate suggesting uniform N contents with uniform layer thicknesses within a given grain. However, they also show significant variations in the  $\gamma_N$  layer thickness from one grain to the next along the plasma nitrided layer clearly supporting the XRD findings of the variations in N diffusivity with grain orientation.

The cross-sectional SEM photomicrographs of the plasma nitrided samples clearly reveal grain structure of the underlying CoCrMo substrate phase after electrochemical and  $\text{Ar}^+$  beam etching. According to the cross-sectional SEM images, the nitrided layers (2 h plasma nitrided) with the  $\gamma_N$ -(CoCrMo) phase has a much better corrosion resistance compared to the substrate  $\gamma$ -(CoCrMo) phase. In contrast, the 6 and 20 h plasma nitrided layers show worse corrosion resistance compared to the substrate phase,  $\gamma$ -(CoCrMo). This is due to the CrN precipitates that is formed in the  $\gamma_N$  matrix for the 6 and 20 h nitrided layers.

The GDOES results clearly indicate enhanced nitrogen diffusion in fcc CoCrMo alloy RF plasma nitrided at 400 °C. The GDOES nitrogen concentration depth profiles suggest that the nitrogen concentration values are quite high at the surfaces of plasma nitrided samples (ranging from ~ 28 to ~ 32 at.%) and then they decrease slowly to a level of ~ 20 to ~ 22 at.%. Within this range, the nitrogen depth profiles are of nearly rectangular shape for all the samples corresponding to a depth of ~ 70-80% of the nitrided layer. From the GDOES profiles, the average nitrogen concentration reached

nearly 25 at.% for all the nitrided samples independent of the plasma nitriding time correlating quite well with the EDX data.

The EDX data collected from the surfaces and the cross-sections of the plasma nitrided samples show that nitrogen concentrations correlate well with the GDOES nitrogen concentration depth profiles. According to the cross-sectional EDX measurements, the nitrogen concentration decreases with the depth (18 at.% on the cross-sectional area in Figure 7.3) compared to the surface EDX results (24.87 at.% on the surface area in Figure 7.3).

Based on the plasma nitrided layer thickness calculations from the cross-sectional microscopy measurements (SEM, AFM and optical microscopy) and the GDOES concentration depth profiles, the average nitrogen diffusion constant is found to be  $\sim 1,5 \times 10^{-11} \text{ cm}^2/\text{s}$ . The higher nitrogen diffusivity found here is attributed to the large N content of the  $\gamma_N$  phase in the nitrided state and is consistent with the Trapping/Detrapping model summarized in Chapter 7.

According to the literature review for the nitrogen diffusion coefficients of the nitrided CoCrMo and FeCrNi alloys, there are not so many difference for the diffusion coefficients between the literature and the results listed in Table 7.5. It is believed that this good correlation comes from the structural (same crystal lattice) and compositional (Cr alloying element which has an important role for the nitrogen diffusion) similarities.

Significant hardness improvement is observed for the plasma nitrided layers from the Vicker's microhardness tests. According to the microhardness results, the hardness of the nitrided layers showed an increase with respect to the increasing nitriding time (increasing nitrided layer thickness). In addition to the plasma nitriding process, it is also believed that the compressive stresses operating in the nitrided layers may add to the increased hardness.

The wear resistance of the bulk material (CoCrMo) is enhanced by plasma nitriding. Furthermore, the longer plasma nitriding time is found to be more effective for the enhanced wear resistance due to the thicker nitrided layers. Reduction in wear obtained with plasma nitriding is generally thought to result from the strengthening of the wearing surface. The observed relative increase in the wear resistance of the nitrided samples are in good agreement with the observed hardness profiles in that the nitrided specimens have higher surface hardness.

## 9.2. Conclusions

- a. A metastable, fcc, high nitrogen concentration phase ( $\gamma_N$ ) is found to be produced in fcc CoCrMo alloy for low-pressure R.F. plasma nitriding under a gas mixture of 60%  $N_2$  – 40%  $H_2$  for a substrate temperature of 400 °C.
- b.  $\gamma_N$  layers are produced in the range 2 to 10 micrometer for 1 to 20 h plasma nitriding times at 400 °C.
- c. The N is found to have a higher content and to diffuse deeper in the (200) grains oriented parallel to the surface compared to the (111) grains.
- d. The larger lattice expansions in the (200) planes are found compared to the (111) planes ( $\sim 10\%$ ).
- e. A preferential (200) orientation of  $\gamma_N$  grains parallel to the surface is observed with increasing nitriding times. When the plasma nitriding time increases, [111] oriented plasma nitrided grains rotate in [200] direction due to nitrogen incorporation to the grains.
- f. CrN phase is observed in the CoCrMo layers nitrided for 6 and 20 h. CrN formed in the 6 and 20 h plasma nitrided layers has a homogenous distribution in the  $\gamma_N$  layers.
- g. The plasma nitrided surfaces became rougher with respect to the nitriding time. Comparing to as-polished CoCrMo surface, the average roughness of the plasma nitrided surfaces increased about 15 times.
- h. Structural defects (intergranular cracks) occur on the plasma nitrided CoCrMo surfaces mainly due to the high compressive stresses in the nitrided layers.
- i. The  $\gamma_N$  (2 h) shows higher corrosion resistance compared to the CoCrMo substrate and the  $\gamma_N + CrN$  composition (6 and 20 h).
- j. The nitrogen diffusion constant is estimated to be  $\sim 1,5 \times 10^{-11} \text{ cm}^2/\text{s}$ . The higher nitrogen diffusivity found here is attributed to the large N content of the  $\gamma_N$  phase in the nitrided state and is consistent with the Trapping/Detrapping model.
- k. According to the GDOES profiles, the average nitrogen concentration reached nearly 25 at.% for all the nitrided samples independent of the plasma nitriding time correlating well with the EDX results.
- l. Significant hardness improvement is observed for the plasma nitrided layers from the Vicker's microhardness tests.

m. The wear resistance of the bulk material (CoCrMo) is enhanced by plasma nitriding. Furthermore, the longer plasma nitriding time is found to be more effective for the enhanced wear resistance due to the thicker nitrided layers.

### **9.3. Future Work**

In this study, it has been observed that the nitrogen diffusion is strongly related to the crystalline orientations. The CoCrMo samples used in this study were polycrystalline. It is thought that the studying with single crystal CoCrMo samples will give further information about the nitrogen diffusion in the nitrided CoCrMo alloy.

As well as the mechanical characterization techniques (hardness and wear test) presented in this study, fatigue tests of the plasma nitriding CoCrMo samples will contribute to the understandings of the mechanical properties of the CoCrMo samples.

In some study, metal ion release from the CoCrMo specimens nitrided by different nitriding techniques but not plasma nitriding one. It should be beneficial for the orthopedic application to investigate the metal ion release from the plasma nitrided CoCrMo samples.

## REFERENCES

- Abrasonis, G. *Phys. Rev. Lett.* 96 (2006): 065901.
- Abrasonis, G., J. P. Riviere, C. Templier, A. Declémy, L. Pranevicius, X. Milhet. *J. Appl. Phys.* 97 (2005): 083531.
- Alvarado, J., R. Maldonado, J. Marxuach and R. Otero. «Biomechanics of hip and knee protheses.» *Applications of Engineering Mechanics in Medicine*, GED, University of Puerto Rico Mayaguez, 2003.
- Banoczy, J., B. Roed-Petersen, J. J. Pindborg, and J. Inovay. "Clinical and histologic studies on electrogalvanically induced oral white lesions." *Oral Surg., Oral Med., Oral Pathol.* 48 (1979): 319-323.
- Bell, T., Y. Sun. *Heat Treat. Met.* 29 (2002): 57.
- Bianco, P. D., P. Ducheyne, and J. M. Cuckler. «Local accumulation of titanium released from a titanium implant in the absence of wear.» *J. Biomed. Mater. Res.* 31 (1996): 227-234.
- Binning, G., C.F. Quate, Ch. Gerber. "Atomic Force Microscope." *Phys. Rev. Lett.* 56, no. 9 (1986): 930-933.
- Chen, J., X.Y. Li, T. Bell, H. Dong. *Wear* 264 (2007): 157.
- Christiansen, T., M.A.J. Sommers. *Defects Diffus. Forum.* 2006. 258-260.
- Christiansen, T. L. *Mater. Sci. Tech.* 159 (2008): 24.
- Collins, G.A., R. Hutchings, K. T. Short, J. Tendys, M. Samandi. *Surf. Coat. Technol.* 417 (1995): 74-75.
- Crank, J. *The Mathematics of Diffusion* 2nd Edition. Oxford , 1975.
- Cullity, B. D. *Elements of X-Ray Diffraction*. Addison-Wesley Publishing Company, 1956.
- Dearnley, P.A., A. Namvar, G.G.A. Hibberd, T. Bell. *Proceedings of the International Conference PSE. Surface Engineering*, 1989. 219.
- Duisabeau, L., P. Combrade, B. Forest. «Environmental effect on fretting of metallic materials for orthopaedic implants.» *Wear* 256 (2004): 805-816.
- Eden, J. W. Boretos and M. Contemporary Biomaterials, Material and Host Responcei Clinical Applications, New Technology and Legal Aspects. Park Ridge: Noyes Publications, 1984.
- Ensinger, W. *Surf. Coat. Technol.* 341 (1998): 100-101.

- Grill, A. «Cold Plasma in Material Fabrication.» IEEE Press. New York: From Fundamental to Applications, 1994.
- Hannula, S. P. *Thin Solid Films* 343 (1989): 181.
- He, H., T. Czerwiec, C. Dong, and H. Michel. *Surf. Coat. Tech.* 331 (2003) 163-164.
- Hudis, M. J. *Appl. Phys.* 44 (1973): 1489.
- "IARC Monographs on the Evaluation of Carcinogenic Risks to Humans: Surgical Implants and other Foreign Bodies." 74 (1999): 65-84.
- Ichii, K., K. Fujimara, T. Takase. *Rep. Kansai Univ. Technol.* 27 (1986): 135.
- Karakan, M., A. Alsarar, A. Çelik. "Effects of Various Gas Mixtures on Plasma Nitriding of AISI 5140 Steel." *Materials Characterization* 49 (2003): 241-246.
- Katti, Kalpana S. «Biomaterials in total joint replacement.» *Colloids and Surfaces B: Biointerfaces*, 2004.
- Kumar, S., M.J. Bladwin, M.P. Fewell, S.C. Haydon, K.T. Short, G.A. Collins, J. Tendys. *Surf. Coat. Technol.* 123 (2000): 29.
- Lakes, S., J. B. Park and R. Biomaterials - an introduction, 2nd Edition. New York: Plenum Press, 1992.
- Leigh, S., M. Samandi, G. A. Collins, K. T. Short, P. Martin and M. Samandi. *Surf. Coat. Tech.* 417 (1995): 74-75.
- Li, X. Y., N. Habibi, T. Bell and H. Dong. "Microstructural characterization of a plasma carburised low carbon Co-Cr alloy." *Surface Engineering* 23, no. 1 (2007): 45-51.
- Lutz, J., A. Lehmann, S. Mandl. "Nitrogen diffusion in medical CoCrNiW alloys after plasma immersion ion implantation." *Surface and Coatings Technology* 202 (2008): 3747-3753.
- Lutz, J., J.W. Gerlach, S. Mändl. *Phys. Stat. Sol. A* 205 (2008): 980.
- Lutz, J., S. Mandl. "Effect of ion energy and chemistry on layer growth processes during nitriding of CoCr alloys." *Nuclear Instruments and Methods in Physics Research B*, 2009: in press.
- Lutz, Johanna, Jürgen w. Gerlach and Stephan Mandl. "PIII nitriding of fcc-alloys containing Ni and Cr." *Physica Status Solidi A* 205, no. 4 (2008): 980-984.
- Mandl, S. *J. Appl. Phys.* 88 (2000): 3323.
- Mandl, S., B. Rauschenbach. *J. Appl. Phys.* 91 (2002): 9737.
- Mändl, S. *Plasma Proc. Polym.* 4 (2007): 239.

- Manova, D. *Surface & Coatings Technology* 201 (2007): 6686–6689.
- Matsumo, O. *Proceedings of the International Ion Engineering Congress*. Kyoto, 1983. 1379.
- Mu, Y., T. Kobayashi, K. Tsuji, M. Sumita, and T. Hanawa. «Causes of titanium release from plate and screws implanted in rabbits.» *J. Materials Science: Materials in Medicine*, 2000: 13583-588.
- Negm, N.Z. «A study of rf plasma nitriding at a constant power in different h<sub>2</sub>-n<sub>2</sub> mixtures at different temperatures.» *Mat. Sci. Eng.*, 2006.
- Öztürk, O., S. Okur, J.P. Riviere. "Structural and magnetic characterization of plasma ion nitrided layer on 316L stainless steel alloy." *Nucl. Ins.& Met. in Phy. Res. B* 267 (2009): 1540–1545.
- Öztürk, O., U. Türkan, A. E. Eroğlu. *Surface and Coatings Technology* 200 (2006): 5687.
- Öztürk, O., U. Türkan, A.E. Eroglu. *Surf. Coat. Technol.* 200 (2006): 5687.
- Parascandola, S., W. Möller, D. L. Williamson. *Appl. Phys. Lett.* 76 (2000): 2194.
- Perdaza F., C. Savall, G. Abrasonis, J. P. Riviere, J. F. Dinhut, and J. L. Grosseau-Poussard. *Thin Films* 515 (2007): 3661
- Philibert, J. *Atom Movements, Diffusion and Mass Transport in Solids*. Les Ulis: Les Editions des Physique, 1991.
- Pourbaix, M. *Atlas of electrochemical equilibria in aqueous solutions*, 2<sup>nd</sup> Edition. Houston: National Association of Corrosion Engineers, 1974.
- Pranevicius, L. *Surface and Coatings Technology* 135 (2001): 250-257.
- Priest, J.M., M.J. Baldwin, M.P. Fewell. «The action of hydrogen in low-pressure rf plasma nitring.» *Surf. Coat. Tech.* 145 (2001): 152-153.
- Ratner, B. D., A. S. Hoffman, F. J. Schoen, and J. E. Lemons. *Biomaterials science: an introduction to materials in medicine*. New York: Elsevier, 1996.
- Renevier, N., T. Czerwiec, P. Collington, H. Michel. *Surf. Coat. Tech.* 98 (1998): 1400.
- Ricard, A. *Surf. Coat. Tech.* 59 (1993): 67.
- Rivière, J.P., C. Templier, A. Declémy, O. Redjda, Y. Chumlyakov, G. Abrasonis. *Surface & Coatings Technology* 201 (2007): 8210–8214.
- Riviere, J. P. *Surf. Coat. Tech.* 99 (2002): 158-159.
- Rosnagel, S. M., J. J. Cuomo and W. D. Westwood. *Handbook of Plasma Processing Technology*. Park Ridge: Noyes, 1990.



- Rutscher, A., H. Deutsch. Wissensspeicher Plasmatechnik. Leipzig: Fachbuchverlag, 1983.
- Samandi, M., B.A. Shedden, D.I. Smith, G.A. Collins, R. Hutchings, J. Tendys. Surf. Coat. Technol. 59 (1993): 261.
- Simith, D. C., R. M. Pilliar, J. B. Metson, and N. S. Melntrye. "Preparative procedures and surface spectroscopic studies." J. Biomed. Mat. Res. 25 (1991): 1069-1084.
- Singer, L. L. Vacuum 34 (1984): 853.
- Stinville, J. C. «PhD Thesis.» Poitiers: University of Poitiers, 2009.
- Sumita, M., Y. Ikada and T. Tateishi. Corrosion fatigue and fretting corrosion fatigue, in Metallic Biomaterials - Fundamentals and Applications. Tokyo: ICP, 2000.
- Szasz, A., D.J. Fabian, A. Hendery, Z. Szasz-Csih. J. Appl. Phys. 66, no. 11 (1989): 5598.
- Teoh, S. H. "Fatigue of biomaterials: a review." Int. J. Fatigue 22 (2000): 825-837.
- Tong, W.P., N.R. Tao, Z.B. Wang, J. Lu, K. Lu. Science 299 (2003): 686.
- Total Hip Replacement: Implant Choices. 2009.  
<http://www.kneereplacement.com/binary/org/DEPUY/doc/pt.com/altbearing s2.ppt>.
- Turkan, U. "Biocompatibility and microstructural characterization of PVD TiN coated and nitrogen implanted Co-Cr alloy." MSc Thesis. İzmir Institute of Technology, 2004.
- Wei, R., T. Booker, C. Rincon. J. Arps, Surf. Coat. Technol. 186 (2004): 305.
- Williamson, D. L., J. A. Davis, and P. J. Wilbur. Surf. Coat. Tech. 178 (1998): 103-104.
- Williamson, D. L., O. Ozturk, R. Wei, P. J. Wilbur. Surf. Coat. Technol. 65 (1994): 15.
- Williamson, D. L., P. J. Wilbur, F. R. Fickett, S. Parascandola,. "Role of ion-beam processing time in the formation and growth of the high-nitrogen phase in austenitic stainless steel." Osaka, 2001. International Current Status Seminar on Thermomechanical Surface Engineering of Stainless Steel.
- Williamson, D.L., Li Wang, R. Wei, P.J. Wilbur. "Solid Solution Strengthening of Stainless Steel Surface Layers by Rapid, High Dose, Elevated Temperature Nitrogen Ion Implantation." Materials Letters 9, no. 9 (1990): 302-308.
- Williamson, D.L., O. Ozturk, R. Wei, P.J. Wilbur. Surf. Coat. Technol. 65 (1994): 15.

Williamson, D. L. *Mat. Res. Soc. Symp/ Proc.* 1992. 473.

Waterhouse, R. B. *Fretting fatigue in aqueous electrolytes*, in *Fretting Fatigue*. London: Applied Science Publishers, 1981.

Yan, Y., A. Neville, D. Dawson. *J. Phys. D: Appl. Phys.* 39 (2006): 3206.

Zairyo-Kagaku, A. Sato. «Biological safety of metallic materials.» 19 (1982): 193-199.

Zhang, Z.L., T. Bell. *Surf. Eng.* 12 (1985): 131.